DISSERTATION

MIXING AND TRANSPORT OF PASSIVE SCALARS AROUND OBSTACLES IN ENVIRONMENTAL FLOWS

Submitted by

Hyeyun Ku

Department of Civil and Environmental Engineering

In partial fulfillment of the requirements

For the Degree of Doctor of Philosiphy

Colorado State University

Fort Collins, Colorado

Fall 2011

Doctoral Committee:

Advisor: Subhas K. Venayagamoorthy

Brian P. Bledsoe
Pierre Y. Julien
Takamitsu Ito

ABSTRACT

MIXING AND TRANSPORT OF PASSIVE SCALARS
AROUND OBSTACLES IN ENVIRONMENTAL FLOWS

Turbulent mixing and transport in environmental flows such as rivers, lakes, estuaries, oceans and the atmosphere has been the subject of numerous studies for many decades. The characteristic chaotic and enhanced mixing properties of turbulence in conjunction with other environmental conditions such as the presence of solid and/or porous obstacles and density stratification raise a number of interesting scientific but yet practical problems pertaining to both flow dynamics and mixing of passive scalars (such as pollutants and nutrients). Understanding these processes is of fundamental importance in applications such as prediction of nutrient and contaminant transport in water bodies (e.g. rivers, estuaries and the ocean), air quality modeling and in many sustainable environmental (e.g. river restoration) and renewable energy related applications (e.g. wind energy technology).

The main aim/objective of this dissertation is to use high-resolution two-dimensional numerical simulations to study the mixing and transport of passive scalars in environmental flows in the presence of varying flow conditions and different arrangement of porous obstacle(s) in the flow domain. The objectives are multi-fold:

- To obtain an understanding of the dynamics of environmental flows around a porous obstacle (idealized as a cylinder in this dissertation) for three different flow scenarios consisting of uni-directional, oscillatory, and a combination of uni-directional and oscillatory velocity fields. In particular, the mixing and

transport of passive scalars in the turbulent flow regime are investigated. It results in quantitative parameterization for the turbulent scalar diffusivity as a function of key non-dimensional parameters, namely: drag coefficient C_D, a ratio of tidal to mean flow (shape parameter) η, and a ratio of tidal excursion length to the obstacle diameter (tidal excursion parameter) K.

- To gain insights of the flow dynamics under multiple flow reversals, for instance purely tidally-driven flow and strong tide with mean current. The effect of the presence of cylindrical obstacle in the flow domain may enhance the horizontal mixing of the passive scalars.

- To investigate the influence of the drag exerted by multiple cylindrical obstacles on the flow and scalar field. In flow field past multiple obstacles, wakes and vortices may interact depending on the distance between the obstacles.

- To highlight the importance of correct description of hydrodynamic conditions (e.g. strength of tides, wind stress and freshwater inflow) and location of obstacles/point sources in engineering application. A series of field-scale, numerical simulations were performed to show the importance using high-resolution, depth-averaged simulations of open netpen aquaculture farms in an idealized coastal embayment.

As a first step toward addressing these objectives and questions, high-resolution two-dimensional numerical simulations have been performed. A simulation of classical dispersion in a uni-directional steady flow field is used as a base case to provide basic understanding of turbulent mixing and for validation. This is followed by slightly more complicated simulations involving obstacles (which are represented by cylinders) placed in the flow domain. The lateral mixing of passive scalars in uni-directional, oscillatory, and a combination of uni-directional and oscillatory flow conditions interacting with single as well as multiple obstacles are presented to highlight issues

related to flow separation at the rear of the obstacles and the associated vortex-wake structures.

An obstacle blocks the flow (partially or fully depending on the porosity) causing deceleration of the flow, shedding of vortices and the formation of a downstream wake. For the first part of this dissertation, an in-depth investigation was carried out to study the effects of the drag exerted by a single obstacle under different flow conditions. In particular, the lateral dispersion coefficient was quantified as a function of the drag coefficient C_D, at two other given parameters. The simulation results show that the lateral mixing (spread) is substantially enhanced due to the drag exerted by the obstacle compared to the classical dispersion in a uni-directional flow without drag. This effect is even further amplified under oscillatory flow conditions (i.e. the lateral mixing is considerably larger and found to be about 40 times the typical classical dispersion coefficient in some cases). The effect of flow reversals on scalar mixing around obstacle has also been examined for pure oscillatory flows. Strong departure from the Gaussian distribution is evident. The results also highlight the complex dispersion patterns around submerged obstacles in oscillatory flow conditions.

The second part of this dissertation focuses on mixing around multiple obstacles using both a single column of three cylinders and a staggered array consisting of eight cylinders, to investigate the lateral mixing of passive scalars. Vortex patterns and sizes depend on the clustering (spacing) of the cylinders. These vortices range from cylinder-scale vortices to mid-scale vortices to array-scale vortices. Finally, to put the current work in the context of a field-scale application, a numerical study on the transport of aquaculture dissolved waste in a coastal embayment is presented to provide an understanding of the impact of aquaculture fish-pens on coastal water quality.

Overall, this dissertation aims to contribute to better fundamental understanding of turbulent mixing around obstacles in environmental flows. The results from this

study have lead to some quantitative and intuitive tips regarding lateral mixing that will translate into simple effective parameterizations of such processes for application in large-scale numerical simulation models for environmental flows.

ACKNOWLEDGEMENTS

I would like to express my sincerest gratitude to my advisor, Professor Subhas Karan Venayagamoorthy, for his encouragement, academic guidance, imparted knowledge, suggestions, and continuous support throughout my PhD studies. I would have never done my dissertation without the able guidance from Karan. I also wish to extend my deepest appreciation to my PhD committee, Dr. Pierre Y. Julien, Dr. Brian P. Bledsoe, and Dr. Takamitsu Ito. I thank all of them for serving on my committee, for their mentorship and encouragement throughout my research.

I also wish to deliver my sincerest gratitude to Professor Sungsu Lee at ChungBuk National University in South Korea. I studied computational and environmental fluid dynamics during my BS and MS in Dept. of Civil System Engineering at CBNU. My professor has been an exceptional mentor for my academic career and in my life as a engineering researcher.

Thanks are also due to Jordan Wilson, Zach Elliot and Amy Xu who were my first co-workers at the Engineering Research Center (ERC) for their friendship. Acknowledgements are also given to Farid Karimpour, Ben Mater, Cole Davis, Simon Schaad, and Zachary Taylor for many enthusiastic discussions on research and for their friendship. I also thank many other friends I have come to know during my years at Colorado State University.

I am very grateful to my parents, Mr Eulseo Ku and Mrs Soonduk Seo, for their trust and love for me which kept me focused on my study. I thank my lovely younger sister, Seulip (who has the other part of my parents' hearts), for her love and support from South Korea. This dissertation is dedicated to my family for their unwavering faith in me.

TABLE OF CONTENTS

LIST OF FIGURES

LIST OF TABLES

Chapter 1

Introduction

1.1 Motivation and background

Turbulence is ubiquitous in environmental flows such as in rivers, lakes, estuaries, oceans and the atmosphere, and it is characterized by chaotic and (supposedly) random motions, with the basic notion that it enhances mixing and transport of both momentum and mass (Tennekes and Lumley 1972). Turbulence is also a common phenomenon in many practical engineering problems such as wall-bounded shear flows and multiphase flows (Balachandar and Eaton 2010). Turbulence is triggered through instabilities in the flow field related to the interaction between the nonlinear inertia term and the viscous term in the governing equations of fluid motion. Naturally, turbulence plays a critical role in the mixing and transport of scalars in environmental flows. In this context a scalar can be regarded as 'passive' such as a contaminant plume that is advected and diffused by the flow field without any dynamic interactions with the flow (i.e. it only depends on the fluid motion (Warhaft, 2000), or 'active' where buoyancy effects will influence the flow dynamics in a coupled manner (e.g. in stably stratified flows)). A great deal of effort has gone into investigating turbulent mixing and transport processes in environmental flows with a broad and

Figure 1.1: Some examples of natural and man-made obstacles encountered in estuarine, oceanic and atmospheric flows.

vast amount of publications. Some well known concepts about turbulent mixing and transport phenomenon in the water environment are nicely summarized in the classic text by Fischer *et al.* (1979).

While, a large body of work exists on understanding turbulent mixing and transport processes in natural flows dating back to the classical dispersion studies by G. I Taylor (see Taylor (1922) and Taylor (1953) for a summary) and Richardson and Stommel (1948), there remains much to be understood in terms of turbulent mixing around obstacles (such as submerged oceanic vegetation or man-made obstacles) as shown in Figure 1.1 in complex flows (e.g. tidally-driven flows superimposed on mean currents). For instance, we do not yet have a clear understanding on how the lateral (turbulent) mixing coefficient should be quantified for flow past a single obstacle due to the added complexity of the drag effect induced by the obstacle(s) and the oscillations in the flow field. Even in the case of steady flows in a neutrally stratified water column, the factors controlling lateral mixing are poorly understood with wide variations in observed values for the lateral mixing coefficient (Fischer *et al.* 1979). Furthermore, evidence from previous field and laboratory studies (Stacey *et al.* 2000; Crimaldi *et al.* 2002; Kay 1997) suggests that contaminants may be transported in plumes that retain their coherence and hence can maintain high concentrations over large distances from the source.

Therefore, much remains to be understood especially in regard to turbulent mixing and transport processes in complex environmental flows (e.g. oscillatory flows such as tidally-driven flows) encountering obstacles (be it porous or solid, streamlined or bluff) such as natural vegetation in water bodies, aquaculture pens, bridge piers, wind turbines and buildings. Full or partial blockage of the flow is induced by such obstacles resulting in a reduction of the velocity of the approaching flow and the formation of wakes behind the body. The drag force exerted by an obstacle depends on the shape and size of the obstacle as well as on the intensity and nature of the flow. For flow passing an obstacle with a no-slip boundary condition, wakes are observed behind the obstacle. The vorticity field behind the obstacle, the so called von Karman vortex street, appears with well-defined frequency, which can be measured by the Strouhal number. Figure 1.2 shows structures of a von Karman vortex at various Reynolds numbers. The two rows of opposite-signed vortices which are unstable are considered an inherent phenomenon (Williamson 1996). At sufficiently high Reynolds numbers, the flow is turbulent, and it includes vortex structure that does not behave like equilibrium turbulence (Zhang and Perot 2000). This wake generation also links with energy transfer from mean kinetic energy into turbulent kinetic energy which affects the drag force on the body and the turbulent intensity (Nepf 1999).

The dynamics of the vortex-wake interactions in itself is a subject of ongoing research. The transport of pollutants under such conditions is even more critical given that many relevant problems related to water and air quality issues occur in these types of flow and environmental conditions. Also, nutrient fluxes in water bodies are directly influenced by the flow dynamics. Changes in magnitude and direction of the velocity field as well as the location of obstacles result in a complex scalar distribution. The need for improved understanding is essential for the development of accurate and reliable models to both reliably predict and mitigate the impacts of pollution in the environment. In the modeling context, the mixing of the scalar

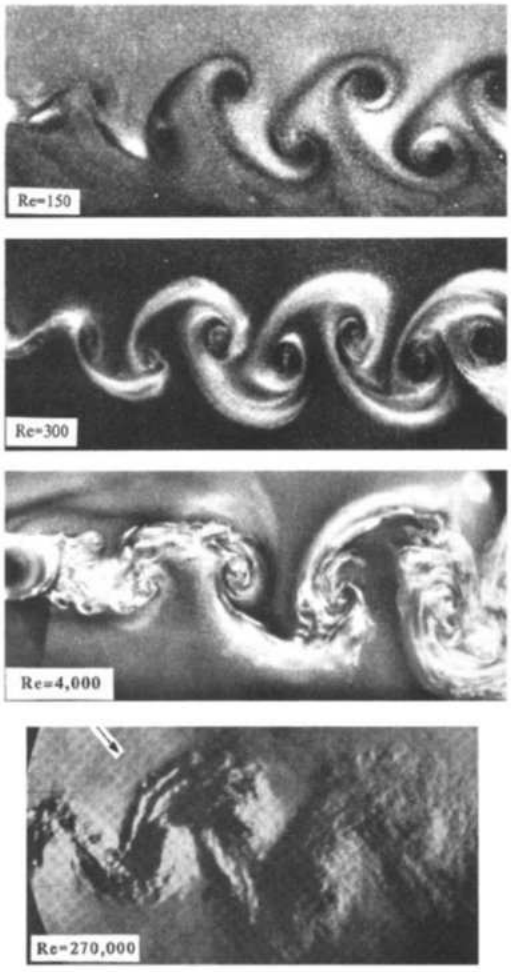

Figure 1.2: Visualization of laminar and turbulent vortex streets over a wide range of Reynolds number, Re. Streamwise vorticity, in the braid between Karman vortices, is indicated by the white regions and is visible for $Re = 300$ up to the highest $Re = 270,000$ (Williamson 1996).

field is parameterized through a turbulent scalar diffusivity (analogous to molecular diffusivity) (Fischer *et al.* 1979; Rummel *et al.* 2005; Rossi and Iaccarino 2008). Many parameterizations exist for the scalar diffusivity under different flow conditions but most do not account for the presence of obstacles as well as varying flow conditions such as a combination of unidirectional and oscillatory flows. It is therefore the subject of this dissertation to investigate fundamental aspects of turbulent mixing and transport processes in environmental flows and develop parameterizations for scalar diffusivities for flow around obstacles under different flow conditions.

The main research tool used in this study is computational fluid dynamics (CFD). CFD is a useful research tool to understand and explicate the physics of fluid flow and it is now widely regarded as one of three key dimensions in fluid dynamics, the other two dimensions are experiments and theory, respectively (Anderson 1995). CFD is essentially the numerical solutions of the Navier-Stokes (momentum) and scalar transport equations. It provides more detailed information on a flow field than is typically afforded by laboratory and field-scale experiments. Furthermore, CFD may be used to generate results to facilitate and compare with experimental results.

1.2 Objectives

In this research, high-resolution two-dimensional numerical simulations will be used to study fundamental aspects of turbulent mixing and transport of passive scalars around submerged porous obstacle(s) in environmental flows. The main objectives of this research are as follows:

1. To understand the dynamics of environmental flows, with particular emphasis on the mixing and transport of passive scalar in the turbulent flow regime, and to parameterize the scalar diffusivity for different flow scenarios consisting of uni-directional flow and a combination of uni-directional and oscillatory flows. We introduce three key non-dimensional parameters, namely: drag coefficient (a surrogate of porosity), a ratio of tidal to mean flow (shape parameter), and a ratio of tidal excursion length to the obstacle diameter. Detailed parametric studies will be performed to investigate the dependence of the scalar diffusivity on the above parameters for a single cylindrical obstacle.

2. To gain insights of flow dynamics under flow reversals (e.g. purely tidally-driven flow and strong oscillatory flow superimposed on the mean current). In particular, scalars transport processes will be investigated with and without drag exerted by a single cylinder.

3. To investigate the influence of the drag exerted by multiple obstacles (an idealized cylinder mostly for the purposes of this investigation) on scalar fields. In flow fields past multiple obstacles, wakes and vortices may interact depending on the distance between the obstacles.

4. To highlight impacts of different hydrodynamic conditions and locations of obstacles in engineering application. The depth-averaged simulations of open net-pen aquaculture farms in an idealized coastal embayment will be performed to show the importance of correct description of such conditions at any given study site.

1.3 Dissertation layout

The remainder of this dissertation is composed of six further chapters: Chapters 3, 4, 5, and 6 have been written in a format suitable for journal manuscripts, hence they are relatively self-contained and as such some redundancy will exist, particularly with regard to governing equations and numerical methodology.

Chapter 2 consists of a literature review on the flow physics and scalar transport. It expands on some of the issues mentioned in Section 1.1. Numerical methodology is also presented with equations that govern flow dynamics and scalar transport. Chapter 3 focuses on the lateral mixing of passive scalars around a single obstacle in steady uni-directional flows as well as a combination of uni-directional and oscillatory flows. The main highlight of this chapter is the quantification of the lateral mixing coefficient as a function of the three key non-dimensional parameters discussed

in Section 1.2. Flow reversals under pure oscillatory flow conditions and associated mixing are presented in Chapter 4. In Chapter 5, the concentration fields of a passive scalar dispersed by the flow encountering a group of cylindrical obstacles are presented. Complex vortex patterns occur around the cylinders which are arranged in either a single column or a staggered array. The effect of spacing between adjacent cylinders on lateral mixing is investigated. To put the current work in the context of a field-scale application, a numerical study on the transport of aquaculture dissolved waste in a coastal embayment is presented in Chapter 6. The importance of accurate description of hydrodynamic conditions as well as the location of obstacles for predicting concentration distribution is highlighted. Finally, Chapter 7 concludes with a summary of what has been done with some suggestions for the further work.

1.4 Summary

This dissertation presents a study on the fundamental aspects of mixing and transport of passive scalars in turbulent environmental flows. High-resolution, two-dimensional simulations are used to study scalar transport around porous obstacles in steady, oscillatory flows and combined flows. The research is carried out primarily by means of high-resolution two-dimensional simulations. Overall, this dissertation aims to contribute to better fundamental understanding of turbulent mixing around obstacles in environmental flows.

Chapter 2

Literature review

Turbulent flow arises from the instability of the flow layers at high Reynolds numbers. The nonlinear nature of turbulence has made it too difficult (but interesting) to fully comprehend it and hence turbulence has and is being continuously investigated by scientists and engineers through field- and laboratory-scale experiments as well as numerical simulations. Under an unsteady flow field caused by the presence of an obstacle, the concept of turbulent vortex shedding is apparent by drag, and this governs the further dynamics of the flow. Most environmental flows fall in the regime of turbulent flows, and are perturbed by obstacles existing in the flow domain such as buildings, bridges, aquaculture pens, trees and vegetation canopies. Passive scalar transport past idealized obstacles such as a cylinder, has been widely used to examine mixing and transport processes in many flow fields (Yasuda 2004; Warhaft 2000). In the case of a disturbance induced by an obstacle, the scalar transport depends on the density and configuration of the obstacles, and the longitudinal dispersion is influenced by different mechanisms, near and far, from the bodies (White and Nepf 2003; Tanino and Nepf 2008).

Changes in flow direction (e.g. in oscillatory flows) will affect the mixing and transport of a scalar. Such flow conditions in the presence of obstacles are even more

complicated and its effects are reflected in the magnitudes of the fluid-induced forces, the fundamental frequency of the lift force, and the reduced momentum and scalar diffusivities compared to uni-directional flows (Smith 1982; Williamson 1985).

This chapter provides an overview of the significant properties of the turbulence and reviews relevant literature corresponding to the objectives of this research. In particular, work by Fischer *et al.* (1979), White and Nepf (2003), Smith (1982), Williamson (1985, 1996), Rummel *et al.* (2005) and Crimaldi and Koseff (2006) are probably the most relevant.

2.1 Basics of flow and scalar transport

The Navier-Stokes equations with Boussinesq approximation for unsteady, three-dimensional incompressible fluid flow with constant kinematic viscosity are given by:

$$\frac{\partial u_i}{\partial t} + \frac{\partial}{\partial x_j}(u_i u_j) = -\frac{1}{\rho_0}\frac{\partial p}{\partial x_i} + \nu\frac{\partial^2 u_i}{\partial x_j \partial x_j} - (\rho - \rho_0)\, g\delta_{i3}, \tag{2.1}$$

with the continuity equation

$$\frac{\partial u_i}{\partial x_i} = 0, \tag{2.2}$$

and the density transport equation

$$\frac{\partial \rho}{\partial t} + \frac{\partial}{\partial x_j}(\rho u_j) = \Gamma\frac{\partial^2 \rho}{\partial x_j \partial x_j}, \tag{2.3}$$

where the Einstein notation is assumed with $i, j = 1, 2, 3$ and x_3 is the vertical coordinate. ρ_0 is the reference density of the fluid, and ρ is the fluid density. Note that the Navier-Stokes equation given in Equation (2.1) includes the effects of the buoyancy resulting from density difference in the vertical such as in stably stratified flows (e.g. in estuaries, oceans and the nocturnal atmospheric boundary layer). The density transport equation given by Equation (2.3) is fully coupled with the Navier-

Stokes equations through the buoyancy term. Here, Γ is eddy diffusivity, which is equivalent to the scalar diffusivity for the scalar transport equation. A separate transport that is similar in form to the density transport equation can be used to solve for the transport of a passive scalar.

In general, the concentration of matter is stretched out by a molecular diffusion process. Fickian law represents the scalar diffusion restated from Fourier's law for heat transfer. Fick's law states that the flux of solute mass is proportional to the gradient of solute concentration in a given direction (Fischer *et al.* 1979). This results in the diffusion equation (using the conservation law of the mass):

$$\frac{\partial \phi}{\partial t} = D \frac{\partial^2 \phi}{\partial x_j \partial x_j}, \tag{2.4}$$

where ϕ is arbitrary scalar, and D is the molecular diffusion coefficient with dimensions of L^2T^{-1}. Considering the two-dimensional transport process of a scalar ϕ in $x - y$ plane, under the assumption that it is well-mixed in vertical direction, the analytical solution for concentration from an initial slug of mass M released at time zero at the x origin is given by:

$$\phi\,(x,t) = \left(\frac{M}{\sqrt{4\pi D t}}\right) \exp\left(-\frac{x^2}{4Dt}\right). \tag{2.5}$$

The factors of 4π and $4Dt$ are added arbitrarily for mathematical convenience. Here, Equation (2.5), which follows Gaussian distribution, represents the longitudinal plume structure. Lateral concentration distribution can be derived by using y component instead of x component.

However, Equation (2.5) only provides the pure diffusive solution (e.g. dye poured in a cup of water and allowed to mix through molecular diffusion without any external stirring). In most environmental flows, the scalar is transported by the mean motion of flow, i.e. the flow is not stationary. The equation, including the advection term by

flow mean motion, is called advection-diffusion equation:

$$\frac{\partial \phi}{\partial t} + \frac{\partial}{\partial x_j}\left(\phi u_j\right) = D\frac{\partial^2 \phi}{\partial x_j \partial x_j}, \tag{2.6}$$

where the second term in the left-hand side is the advection term describing the transport of ϕ by a velocity field u_j and the right-hand side is the diffusion term. While Equations (2.4) and (2.5) emphasize the molecular process, Equation (2.6) accounts for fluid motion and hence the appropriate transport equation that captures the longitudinal structure of the scalar plume that results from the combination of advection and diffusion effects. For example, a solution describing the plume structure in a fluid moving with a constant velocity u in the longitudinal direction (x) with negligible gradients (well mixed) in the lateral (y) direction is as follows Fischer *et al.* (1979):

$$\phi\left(x,t\right) = \frac{\phi_0}{2}\left[1 - erf\left(\frac{x-ut}{\sqrt{4Dt}}\right)\right], \tag{2.7}$$

where ϕ_0 is the initial concentration. The error function describing the plume structure is formed by integral of the Gaussian distribution and it always converges.

However, the diffusion coefficient in the above equations is based on molecular diffusion applicable to laminar flows. In turbulent flows (common in the environment), mixing is greatly enhanced mainly due the shear. The accepted norm is to define an analogous turbulent mixing coefficient (commonly known as a turbulent scalar diffusivity) in order to solve for the average concentration.

2.2 Analytical work

Laminar, transition, and turbulence represent the characteristics of the flow. These are classified by the Reynolds number which is the ratio of inertial forces to viscous forces. Osborne Reynolds showed how the flow physically transitions using his now

famous dye injection pipe flow experiments (Munson *et al.* 2009). In a laminar flow, the dye streak remains along a well-defined line, while the streakline in a turbulent flow is immediately blurred and spreads across the cross-section. The dye streak fluctuates in time and space at transition. This transition stage may be considered as a universal phenomenon that leads to an enhanced turbulent flow state (Dimotakis 2000). As mentioned, the dye streak moves with the flow, the turbulent motion enables heat and other scalar quantities to diffuse in a fluid by molecular agitation, thereby greatly enhancing molecular diffusion (Taylor 1922). Taylor (1953) derived an analytical solution for the soluble matter through a tube. The scalar disperses by the combined action of molecular diffusion and velocity shear over the cross-section. Taylor's analysis provides a methodology for the estimation of the diffusion coefficient.

In a similar manner, the dispersion in turbulent flow was studied by Taylor (1954). Aris (1956) compared diffusion occurring in circular and elliptical cross-sections to obtain Taylor's results. He fixed his attention on the movement of the mean of the concentration distribution and the growth of its higher moment. Fischer (1978) applied a one-dimensional dispersion equation and extended it to a shear flow at horizontally homogeneous depth. The magnitude of a coefficient describing the effect of the shear flow was derived.

When fluid flows around an obstacle (a bluff body in this context), the flow creates alternating low-pressure vortices at the point of boundary layer separation (Munson *et al.* 2009). The location of the separation point and configuration of wakes depend on drag forces induced by the shear stress at the boundary layer of the cylinder. Gerrard (1978) investigated the wakes of bluff bodies by using dye washed from the rear of the cylinders at low Reynolds number. He derived relationship between the Reynolds number and the Stokes number, which is equal to the Reynolds number multiplied by Strouhal number, to highlight the physical significance of the oscillations. It turns out that relationship depends more on the range of Reynolds number

than on the cylinder configuration. Vortex shedding is a typical characteristic of fluid flowing around obstacles. From laminar through turbulent flow, various regimes are classified as having different types of wakes, and they are divided based on Reynolds number and pressure coefficient (Williamson 1996). White and Nepf (2003) classified the wake behind an obstacle into two zones: vortex-trapping zone and secondary-wake dispersion zone. They described the dispersion of a scalar from a random array of circular cylinders and went on to suggest two mechanisms for each zone leading the longitudinal dispersion of a passive scalar due to the solid fraction and distance between cylinders.

The wakes occur at the rear of obstacles. When the flow switches direction, for example a shift in wind direction or a tidal current, the flow movements will affect all the properties associated with the mixing and transport of the scalar. Holley *et al.* (1970) investigated the longitudinal dispersion to predict the magnitude of dispersion coefficients in tidal waterways. In their study of the effect of oscillatory flow on dispersion, they found that either transverse or vertical variations of velocity will be more important in the dispersion process. Chatwin (1975) studied passive contaminant dispersion in a flow varying harmonically in time from an imposed longitudinal pressure gradient. They concluded that the effective longitudinal diffusion coefficient depends on both frequency and the Schmidt number of the scalar contaminant. Analytically, the negative diffusivities, which arise due to flow reversals, imply the spontaneous development of infinite concentrations. This means that a diffusion equation can not be used to obtain analytic solutions (Smith 1981, 1982). Smith proposed the delay-diffusion equation where the dispersion term is replaced by an advected memory term for steady flow. The negative diffusivity involved in an advected memory term is verified using 2-dimensional contaminant equation (Liu and Tsai 1993). The centroid and variances are exactly derived as functions across the flow, and the concentration is enhanced where the shear is large (Smith 1983, 1985). For the first few tidal cycles,

the rates of dilution of tracers rapidly increased (Smith and Scott 1997). The plume concentration distribution also deviates from the Gaussian profile in the flow direction since peaks in concentration occur due to flow deceleration (Kay 1990, 1997).

2.3 Laboratory-scale work

In efforts to investigate the plume structure in environmental flows, numerous experimental studies have been performed. Emphasis has been on quantifying the turbulent diffusion coefficient from plume experiments in order to obtain insights as well as parameterizations that may be widely applicable for dispersion modeling. The analytical solutions presented in Section 2.1 have often been used to compare and validate experimental results. Rummel *et al.* (2005), and Crimaldi and Koseff (2006) used a model having a smooth boundary. The flow was shallow which implies that the horizontal scales (length and width) are very large compared to the depth. The smooth bottom boundary permits for the development of the classical turbulent velocity profile from the bottom to the free surface with velocity profile given by the well known logarithmic law. These flows are prone to instabilities induced by large-scale, two-dimensional coherent structures which lead to enhanced eddy diffusivities. Both of these studies show that the plume structure transported by the mean flow follow the analytical solution. Crimaldi *et al.* (2002) and Crimaldi and Koseff (2006) show that lateral structures behave in a self-similar form while the longitudinal structures do not take on self-similar form at different heights. The diffusion coefficient obtained from using statistical analysis of plume width show reasonable agreement with typical values estimated by Fischer *et al.* (1979).

Rummel *et al.* (2005) and Chen and Jirka (1995) studied contaminant distribution past solid obstacles. While Rummel *et al.* (2005) focused on estimating scalar diffusion coefficient as a function of turbulence intensity, Chen and Jirka (1995) were

more concerned with dynamics of the turbulent wake downstream of the obstacles especially since different behaviors have been observed between the near- and far-wakes fields. Rummel *et al.* (2005) found that the scalar diffusivities are larger for a plume discharged in a flow field that encounters a row of cylinders than the diffusivity obtained for a plume dispersing in uniform mean flow. Figure 2.1 shows the time-averaged scalar concentration from their experimental study. Chen and Jirka (1995) verified that vortex streets formed at high Reynolds numbers, as well as von Karman vortices formed at even smaller Reynolds number, are a result of the small-scale turbulent mixing induced by the shear at the bottom. It appears that the vortex street in essence increases the effective mixing thus making the plume width to grow (i.e. disperse wider).

The flow disturbance also depends on the density and configuration of obstacles (White and Nepf 2003). The longitudinal dispersion of a passive scalar in a random array of circular cylinders is depicted by two mechanisms: vortex-trapping dispersion close to each cylinder and secondary-wake dispersion. In the vortex-trapping field, the dispersion depends on the density (used in this context to reflect how closely the cylinders are packed together) since this is one of main parameters that determines the turbulent intensity, and is expected to be the dominant parameter for the total dispersion (White and Nepf 2003; Tanino and Nepf 2008). Zhang and Zhou (2001) studied the turbulent near-wake of three side-by-side cylinders with different spacing. When the ratio of lateral spacing between two cylinders to the cylinder diameter is in the range $1.2-5$, two distinct wakes were observed with strong interaction.

It is apparent that the turbulent field past obstacles will be dominated by the density and configuration of the obstacles. However, characteristics of the flow are described by boundary conditions such as properties of the fluid, shape/roughness of obstacle, the magnitude and direction of the velocity field. For the case of an oscillatory flow with periodic back-and-forth oscillations, the reversed flow causes the

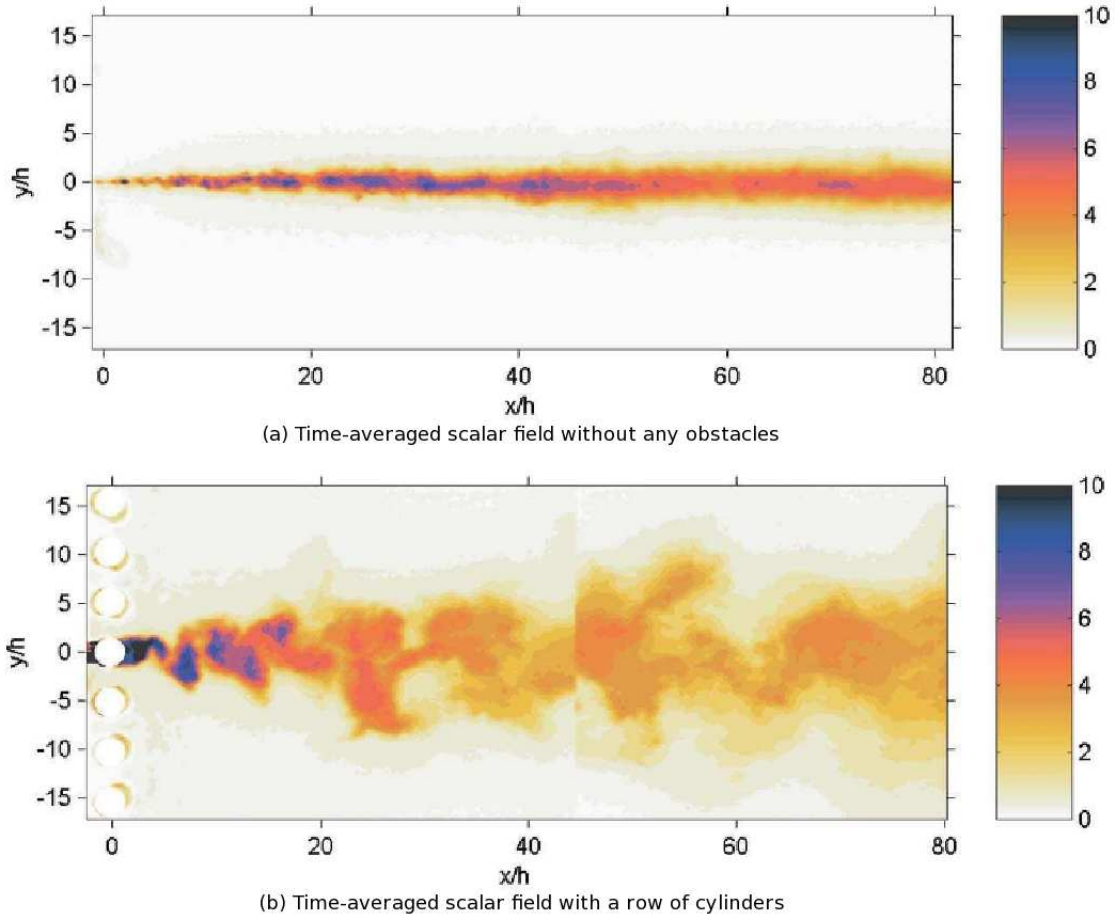

Figure 2.1: Time-averaged concentration distributions from laboratory experiments (Rummel *et al.* 2005).

vortex wake of one half cycle to sweep past the cylinder during the next half cycle (Williamson 1985). Williamson studied the vortex motion using a single cylinder with various Keulegan-Carpenter numbers, which is a ratio of the magnitude of oscillatory velocity to the frequency of the velocity and cylinder diameter, $K = 2U_{osc}/\omega D$. He also investigated a pair of cylinders in line. The change in direction of flow affects the fluid-induced lift and in-line forces. In the case of a pair of cylinders, both vortex shedding and induced forces are simultaneously in-phase or anti-phase between the obstacles.

Despite the numerous studies on scalar mixing and dispersion, there has been a dearth of studies as far as scalar dispersion around obstacles especially under oscillatory flow conditions as well as combined oscillatory and uni-directional flow conditions, even at the laboratory scale. Mixing and transport of passive scalars under such conditions are expected to be very different from the classical uni-directional flow case where a Gaussian plume spread occurs. Some fundamental research questions that need to be addressed and that have shaped the theme of this dissertation are:

- How is the distribution of the scalar field altered in the presence of obstacles (be it single or multiple)? How different are the distributions compared to the classical uniform flow field?

- How do the most relevant non-dimensional parameters affect passive scalar mixing for flow around obstacles in both uni-directional and oscillatory flow conditions? (i.e. How does the lateral mixing coefficient (i.e. turbulent scalar diffusivity) depend (or vary) as function of the most relevant non-dimensional parameters?)

- How do the multiple flow reversals govern the plume concentration of passive scalars in the absence and the presence of the obstacle?

- How does the spacing between neighboring obstacles influence both the flow and scalar fields?

2.4 Numerical work

Numerical simulations are increasingly being used to study turbulent flows. They are used to obtain better understanding of the flow physics since they not only provide more detailed information than laboratory- and field-scaled experiments, but also results to compare with experimental results (Venayagamoorthy 2006). They are also

cost effective and provide considerable time savings. Recently, Stevens *et al.* (2008), Delaux *et al.* (2010), and Venayagamoorthy *et al.* (2011 - part of this dissertation study) identify the environmental impacts of aquaculture pens through field and numerical studies. As mentioned in Section 2.3, fluid-structure induced disturbance is complex and depends on the configurations of obstacles. Bosch and Rodi (1998) studied the flow dynamics past a square cylinder, and Fernando *et al.* (2010) simulated flow around buildings using rectangular boxes to understand the fluid dynamics of urban boundary layers. Zhang and Perot (2000) used a triangular cylinder, and Catalano *et al.* (2003) obtained numerical results using a circular obstacle.

The numerical solution of the Navier-Stokes equations for turbulent flow is extremely difficult, and due to the significantly different mixing-length scales that are involved in turbulent flow, the stable solution of this set of equations requires a very fine mesh resolution resulting in computational times that are prohibitively expensive. There are three main numerical modeling approaches for simulating turbulent flows namely: direct numerical simulation (DNS), large eddy simulation (LES), and Reynolds averaged Navier-Stokes simulation (RANS). DNS can capture all the scales of turbulent motion, however, it requires a lot of computing effort and is not feasible for most practical flow problems of interest where the Reynolds numbers are high. LES is a fairly recent approach that bridge the extremes between DNS and RANS (Ting and Prakash 2005; Pope 2000). LES is increasingly becoming popular with the rapid development of high performance computing hardware and software. As a result, a number of numerical methods using LES have been developed with simulation results showing better predictions of turbulent motions than RANS simulations. RANS equations classify the motion into mean and fluctuation components using the what is called the Reynolds decomposition. All turbulence scales are modeled in RANS because of the averaging process, which effectively removes all turbulent fluctuations. Figure 2.2 shows turbulent motions captured by these three different

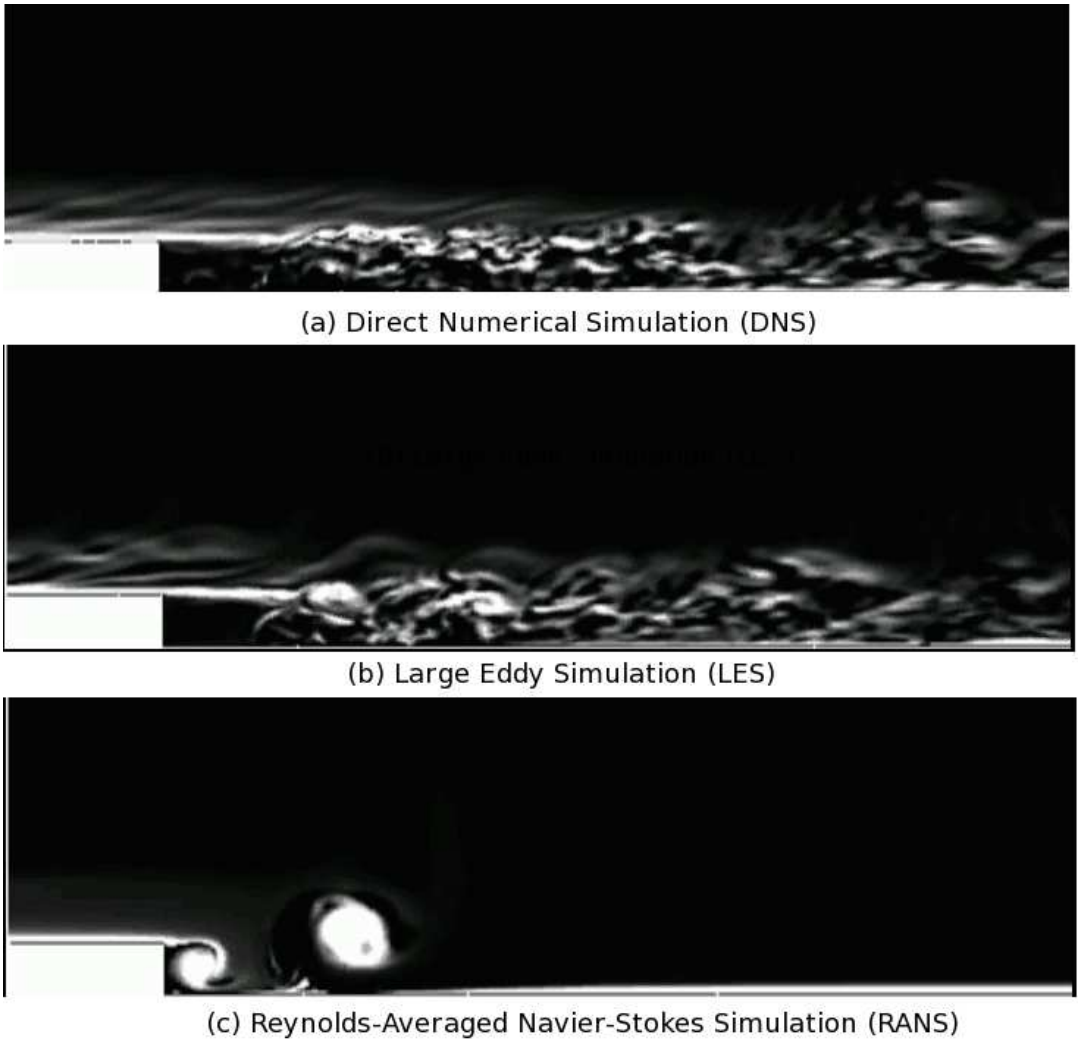

Figure 2.2: Spanwise vorticity for flow over a back-ward facing step from; (a) Direct Numerical Simulation (DNS), (b) Large Eddy Simulation (LES), and (c) Reynolds Averaged Navier-Stokes Simulation (RANS) (Wu *et al.* (Center for Turbulent Research)).

simulations. Catalano *et al.* (2003) concluded that the results from the LES simulation are considerably more accurate than RANS. Nevertheless, RANS simulations are widely used mainly due to their feasibility for practical engineering problems.

Rossi and Iaccarino (2008) compared mean scalar concentration fields using various models to describe turbulence in the RANS approach. The turbulence models depend on a number of extra equations employed such as two-equation models (e.g. κ-ϵ and κ-ω), and Reynolds Stress Transport (RST) models which make use of six extra

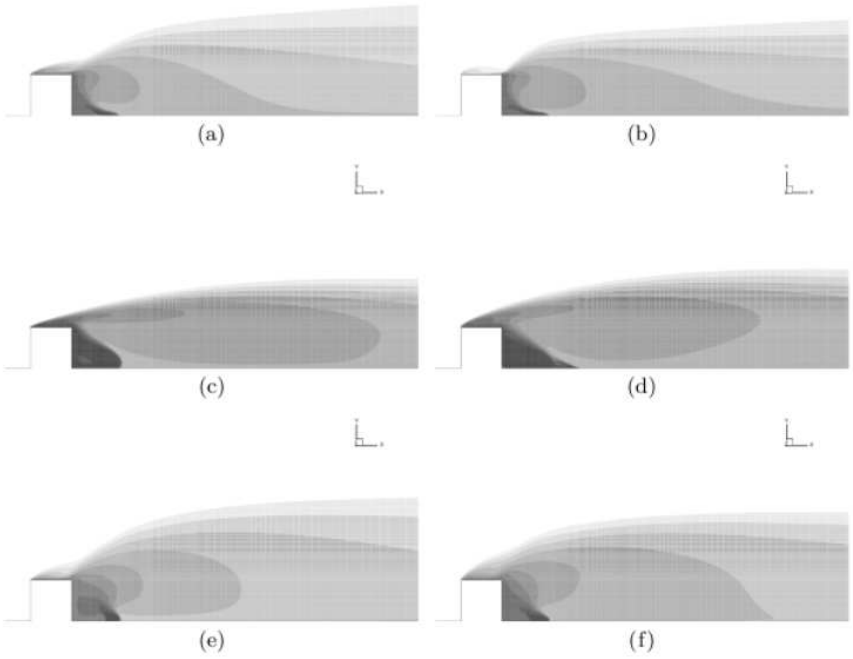

Figure 2.3: Mean scalar concentration downstream of the obstacle, (left column) water setup, (right column) air setup; (a,b) $\kappa - \epsilon$, (c,d) $\kappa - \omega$, (e,f) RST (Rossi and Iaccarino 2008).

equations. Figure 2.3 shows the mean scalar concentration downstream of a rectangular obstacle. The κ-ϵ and RST models suggest a stronger diffusive flux across the wake boundary. Rossi *et al.* (2009) adopted the algebraic flux models for turbulent heat and mass transport for evaluating the scalar flux for complex flows in an attempt to predict the scalar dispersion over a wavy wall.

RANS models are found to be deficient in flows with a wide range of scales encountering obstacles. DNS is mainly restricted to low Reynolds numbers and very simple geometries due to computational constraints required to fully resolve the whole spectrum of spatial and temporal scales. LES is now widely considered in the research community as the acceptable approach and as the compromise between the DNS and RANS approaches. LES can be expected to be more accurate and reliable than RANS for flows in demanding complex geometries which involves unsteady separation and vortex sheddings (Reynolds 1990; Pope 2004).

The theory behind LES is that the large scales of a flow which are explicitly resolved contain the bulk of the energy and the characteristics of the turbulent structures of the flow. A key assumption used in LES is that of universal (isotropic) behavior of turbulence at sub-grid scales which are essentially captured by sub-grid scale (SGS) models. In this manner, LES is able to resolve a wider range of energetic scales compared to DNS thus allowing for the modeling of higher Reynolds number flows at comparable computational costs. The spatial filtering operation results in sub-grid scale stresses/fluxes that must be modeled to achieve closure of the filtered system of equations. Discussions on intricacies pertaining to filtering approaches (implicit versus explicit) can be found in Carati *et al.* (2001) and Gullbrand and Chow (2003). The key to success of LES largely depends on how accurately the SGS motions (or more precisely stresses/fluxes) are modeled based on the resolved-scale quantities such as the velocity gradients and scalar gradients. Several SGS closure models have been proposed, of which the most widely used is the traditional Smagorinsky eddy viscosity model (Smagorinsky 1963), which is based on a gradient-diffusion hypothesis. Germano *et al.* (1991) developed the dynamic Smagorinsky model (DSM) which calculates the eddy viscosity dynamically in time and space. Similar SGS models are also required to quantify scalar fluxes for turbulent flows. An excellent discussion on existing turbulence models and their relative merits is given by Meneveau and Katz (2000).

2.5 Research code

In this research, an LES research code named SUNTANS (Stanford Unstructured Nonhydrostatic Terrain-following Adaptive Navier-Stokes Simulator) is used to perform highly resolved numerical simulations to investigate passive scalar mixing around obstacles. This research code is briefly reviewed next.

2.5.1 Research code description

SUNTANS is a research code developed at Stanford University by Professor Fringer (Fringer *et al.* 2006) with the goal of simulating nonlinear, nonhydrostatic coastal processes. It is finite-volume code based on the nonhydrostatic formulation of Casulli (1999) where the pressure term is split into hydrostatic and non-hydrostatic components. SUNTANS solves the non-hydrostatic Navier-Stokes equations with the Boussinesq approximation on unstructured, staggered, z-level grid. It solves the filtered equations of motions (as described in LES). This numerical model also solves the scalar transport equation with a formulation that ensures both local and global conservation. To increase the computational efficiency, parallel implementation using MPI is adopted. The grid partitioning is done in the horizontal to ensure that water columns remain continuous on each processor due to the use of unstructured grids in plan form and a staggered z-grid in vertical. Time stepping in SUNTANS is limited by accuracy considerations to capture short timescale processes associated with short lengthscales resolved on high-resolution unstructured grids (see Fringer *et al.* 2006 for details).

SUNTANS has proved to be a highly suitable research code for studying multiscale coastal processes. Jachec *et al.* (2006) employed SUNTANS to simulate internal tides in Monterey Bay. Wang *et al.* (2008) applied SUNTANS in the macrotidal Snohomish River estuary to study the interaction of tides with complex bathymetry and associated hydrodynamics.

2.5.2 Numerical limitations

In the SUNTANS, a number of numerical methods are applied to each term in the governing equations. For example, the theta-method is used for the time discretization of the vertical diffusion term and the fast free-surface gravity wave term. Scalar transport equations can be discretized from simple first-order schemes to more accu-

rate higher-order schemes known as total variation diminishing (TVD) schemes.

Convergence of numerical results is limited by time step size. The stability requirement is however not limited by the vertical diffusion term and the fast free-surface gravity waves term, since these are discretized using the semi-implicit theta method. The stability is limited by the terms discretized explicitly using explicit schemes such as the Adams-Bashforth method. The time step is also determined by the accuracy required in the simulations. For coastal applications, the internal wave gravity is the most limiting for stability, while the most limiting is the vertical advection of momentum for the estuarine applications (Fringer *et al.* 2006).

2.6 Summary

This chapter has introduced some of the fundamental aspects and complexities of mixing in environmental flows. A brief review of analytical and laboratory scale work, and numerical simulations focusing on passive scalar field in different flow fields with and without obstacles was provided. The numerical research code named SUNTANS employed in this dissertation has been also described. The next chapter discusses mixing and transport of a passive scalar around a single obstacle.

Chapter 3

Lateral mixing of passive scalars around a porous obstacle[1]

3.1 Introduction

There has been numerous studies over the last few decades focusing on understanding the vortex-wake dynamics around obstacles under different flow conditions (e.g. tides and currents) driven by both a need to gain fundamental insight on the dynamics and the relevance of this problem in engineering, atmospheric science and oceanography. Some examples include mixing and transport through vegetation (White and Nepf 2003; Tanino and Nepf 2008) and flow over and around topographic features. Despite the large body of existing work on this subject, there remains much to be understood in terms of turbulent mixing around obstacles (be it submerged oceanic vegetation, underwater topographic features such as seamounts, ridges, islands or manmade obstacles such as marine aquaculture pens, offshore wind turbines) in complex flows (e.g. tidally-driven oscillatory flows superimposed on unidirectional currents). For

[1]This chapter will be submitted in substantial part as a manuscript entitled "Lateral mixing of passive scalars around porous obstacles in uniform and oscillatory flows", by H. Ku and S. K. Venayagamoorthy, to *Physics of Fluids* Journal.

instance, we do not yet have a clear understanding on how the lateral (turbulent) mixing coefficient should be quantified for flow past a single obstacle due to the added complexity of the drag effect induced by the obstacle(s) and the oscillations in the flow field. Full or partial blockage of the flow induced by obstacles result in a reduction of the velocity of the approaching flow, flow separation and the formation of eddies and wakes behind the obstacles. It is therefore critical to understand and describe the turbulence resulting from such complex interactions in order to make practical progress towards obtaining quantitative estimates of mixing and transport under such conditions.

In what follows in this chapter, we use highly-resolved two-dimensional, depth-averaged numerical simulations to study passive scalar transport around obstacles in an idealized open channel domain. Specifically, we seek to parameterize the horizontal dispersion of the scalar plume using a lateral mixing coefficient which is a function of three dimensionless parameters namely; the non-dimensional drag coefficient C_D, the ratio of mean to tidal amplitudes of the velocity components η, and the tidal excursion length scale K. In Section 3.2, we provide a brief description of the numerical methodology employed for this study and the statistical measures that will be used to quantify scalar concentrations. The key non-dimensional parameters and the simulations cases are presented in Section 3.3. Results and discussion are presented in Section 3.4 and we conclude with a brief summary in Section 3.5.

3.2 Numerical methodology

A research code named SUNTANS (Stanford Unstructured Nonhydrostatic Terrain-following Adaptive Navier-Stokes Simulator), developed at Stanford University by Fringer *et al.* (2006), is employed to perform highly resolved numerical simulations in an idealized rectangular open channel domain. SUNTANS was developed for the

purpose of simulating multi-scale physics in environmental flows. It is an unstructured (in the horizontal) finite-volume code that solves three-dimensional nonhydrostatic Navier-Stokes equations with the Boussinesq approximation on z-level grids in the vertical. It also solves for the free surface as well as the transport of salinity and temperature. Parallel implementation using the message processing interface (MPI) is used in SUNTANS making it a highly scalable and computationally efficient code.

3.2.1 Governing equations

In this research, the depth-averaged formulation of SUNTANS using a single vertical layer is employed for all simulations. These equations together with depth-averaged continuity equations are given by

$$\frac{\partial u}{\partial t} + u\frac{\partial u}{\partial x} + v\frac{\partial u}{\partial y} = -g\frac{\partial h}{\partial x} + \nu_H\left(\frac{\partial^2 u}{\partial x^2} + \frac{\partial^2 u}{\partial y^2}\right) - C_{DB}\frac{\sqrt{u^2+v^2}}{H}u + F_{D,x}, \quad (3.1)$$

$$\frac{\partial v}{\partial t} + u\frac{\partial v}{\partial x} + v\frac{\partial v}{\partial y} = -g\frac{\partial h}{\partial y} + \nu_H\left(\frac{\partial^2 v}{\partial x^2} + \frac{\partial^2 v}{\partial y^2}\right) - C_{DB}\frac{\sqrt{u^2+v^2}}{H}v + F_{D,y}, \quad (3.2)$$

$$\frac{\partial h}{\partial t} + \frac{\partial}{\partial x}(Hu) + \frac{\partial}{\partial y}(Hv) = 0, \quad (3.3)$$

where u and v are the horizontal cartesian components of the depth-averaged velocity vector in m s^{-1}; t is time in s; g is the constant of gravitational acceleration in m s^{-2}; $H = h + d$ is the total water depth in m; h is the free-surface height relative to some vertical datum in m; d is the depth of the bottom relative to some vertical datum in m; ν_H is the horizontal diffusivity of momentum in $m^2 s^{-1}$; C_{DB} is a non-dimensional bottom drag coefficient; $F_{D,x}$ and $F_{D,y}$ are the drag forces exerted by obstacles in x and y directions respectively. They are given by a quadratic drag law formulation as

shown in Equation (3.12). Note, we have neglected the rotation of the earth in all the simulations discussed in this chapter.

3.2.2 Transport equation and statistical parameters

A separate transport equation that is similar in form to the density transport equation (see Equation (2.3)) is used to solve for the transport of an arbitrary passive scalar C in this study. In this section, an analytical solution for the passive scalar concentration and some basic statistical measures that will be used to provide quantitative description of scalar concentrations are briefly reviewed. This study focuses on the passive scalar transport in a depth-averaged flow domain, i.e. x-y plane, under the assumption that the scalar is well mixed in the vertical direction. In general, this assumption is valid when the transverse mixing time-scale is much larger than the vertical mixing time-scale by at least an order of magnitude (Fischer *et al.* 1979). In this case, the steady state turbulent mean scalar transport equation in a flow field with mean velocity $\bar{u}$ is given by

$$\bar{u}\frac{\partial \bar{C}}{\partial x} = \frac{\partial}{\partial y}\left(\varepsilon_y \frac{\partial \bar{C}}{\partial y}\right), \tag{3.4}$$

where ε_y is the turbulent (lateral) scalar diffusivity. In Equation (3.4), the molecular diffusion in flow direction is neglected relative to the advective scalar flux. The analytical solution for a Gaussian distribution with a source of mass of constant strength $\dot{M}$ is given as

$$\bar{C}\left(x, y\right) = \frac{\dot{M}}{\sqrt{4\pi\varepsilon_y x/\bar{u}}} \exp\left(-\frac{y^2}{2\sigma_y^2}\right), \tag{3.5}$$

where the standard deviation σ_y is given by

$$\sigma_y = \sqrt{\frac{2\varepsilon_y}{\bar{u}}x}. \tag{3.6}$$

It can be seen from Equation (3.6) that the plume grows with $x^{1/2}$ with its magnitude decaying like $x^{-1/2}$ in the flow direction. The standard deviation σ_y therefore provides a measure of the plume width at any given cross-section. It can be calculated from the second moment of the concentration distribution. In general, the n-th moment of a distribution is (Fischer *et al.* 1979; Papoulis and Pillai 2002):

$$m_n = E\left\{\mathbf{x}^n\right\} = \int_{-\infty}^{\infty} x^n f\left(x\right) dx. \tag{3.7}$$

The mean, μ, and the standard deviation, σ, of a random distribution are given by

$$\mu = \frac{m_1}{m_0}, \tag{3.8}$$

$$\sigma = \sqrt{\left(\frac{m_2}{m_0}\right) - \mu^2}. \tag{3.9}$$

The standard deviation can be expected to increase downstream of the source due to lateral mixing. For a Gaussian distribution, the plume width at any given cross-section is approximately equal to four times the standard deviation at that particular cross-section. This analytical solution in conjunction with empirical relationships for the lateral mixing coefficient will be used to validate the numerical simulation results for classical dispersion in Section 3.4.1.

3.3 Problem configurations

Here, a description of the open channel flow domain that is used for all the numerical simulations in this chapter is presented first. We then discuss the key non-dimensional parameters that are relevant to the problem at hand. These parameters will be used to quantify the lateral mixing coefficient. We will then present an outline of all the simulations cases that were performed for this parametric study.

3.3.1 Problem setup

An idealized rectangular open channel domain of 3 km long and 1 km wide (as shown in Figure 3.1) is used for all simulations. The flow depth d=50 m is represented by a single vertical layer in SUNTANS. A passive scalar is released from within the perimeter of a porous circular cylinder. We parameterize the porosity of the cylinder through a non-dimensional drag coefficient (see Section 3.3.2).

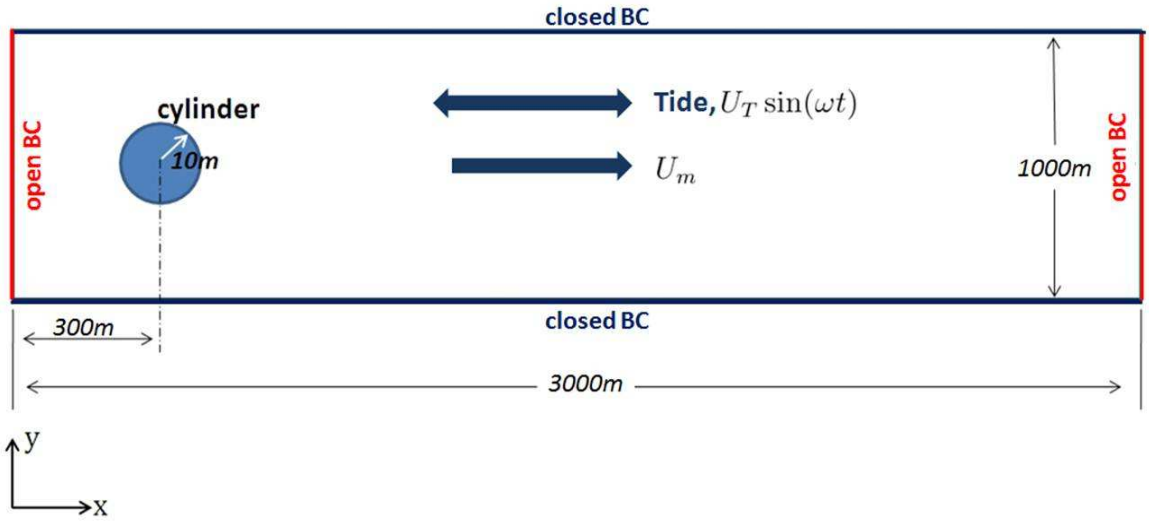

Figure 3.1: Schematic showing the open channel domain and setup used in the numerical simulations for this study. A velocity field described by Equation (3.10) with different forcing periods is imposed at the left-boundary of the domain. The center of the cylindrical porous obstacle is located at $x = 300$ m and $y = 500$ m.

For all simulations, we impose a velocity field at the left-boundary of the open channel domain given by

$$u = U_m + U_T \sin(\omega t), \tag{3.10}$$

where U_m and U_T are amplitudes of mean and tidal velocity components in m s^{-1}, respectively; and ω is the forcing frequency. Boundary conditions for the horizontal velocity u are free-slip at the lateral walls. The horizontal component in the y-direction of the velocity field v has no-flux boundary conditions on the lateral walls, and the scalar field has gradient-free boundary condition on all walls. The unstruc-

tured mesh has a total of approximately 193000 cells, with grid refinement of up to 1 m near the cylindrical obstacle depicted in Figure 3.1. The grid is horizontally stretched to about 10 m at the right-end boundary. The minimum voronoi distance obtained from the two-dimensional Delaunay triangulation is approximately 0.08 m. For stability, the minimum voronoi distance and the magnitude of maximum velocity are used to restrict the time step size which is given by

$$\triangle t \leq C_m \frac{D_{j,min}}{|u|_{max}}, \tag{3.11}$$

where C_m is the maximum Courant number, $D_{j,min}$ is the minimum voronoi distance, and $|u|_{max}$ is maximum amplitude of velocity field (Fringer 2007). We find that a maximum Courant number of 0.5 is required to ensure stability.

3.3.2 Three key non-dimensional parameters

For the flow conditions prescribed by Equation (3.10) in the presence of a porous obstacle, there are three key non-dimensional parameters that can be used to provide a general way to describe both the flow conditions as well as the porosity of the obstacles. These parameters are: the drag coefficient C_D, the ratio of mean to tidal amplitudes of the flow η, and the ratio of the tidal excursion lengthscale to the obstacle length scale K. We quantify the lateral mixing coefficient as a function of these three parameters. We discuss these parameters in slightly more detail next.

The drag coefficient C_D is used in this study as a surrogate for the porosity of the obstacle. The drag force exerted by the cylinder is represented on the right-hand side of the Navier-Stokes equations (as shown in Equation (3.1) and Equation (3.2)) using a quadratic drag law formulation as follows

$$F_{D,x} = -\frac{\alpha C_D (u^2 + v^2)^{1/2}}{D} u,$$
$$F_{D,y} = -\frac{\alpha C_D (u^2 + v^2)^{1/2}}{D} v, \tag{3.12}$$

where C_D is the non-dimensional drag coefficient, and $\alpha = 1$ inside the cylinder, while $\alpha = 0$ outside the cylinder. These drag laws describe the flow reduction inside the obstacle and resulting decrease in momentum downstream of the cylinder. The continuous passive scalar point source is placed inside the perimeter of the cylinder.

The second important non-dimensional parameter for our simple model flow problem is the ratio of the tidal to mean amplitudes of the velocity field given by

$$\eta = \frac{U_T}{U_m}. \tag{3.13}$$

This parameter compares the amplitudes of the tidal flow U_T to the mean current U_m. It is an important factor that determines the shape of scalar plume (Purnama and Kay 1999). The third important non-dimensional parameter is the ratio of the tidal excursion lengthscale to the obstacle length scale given by

$$K = \frac{2U_T}{\omega D}, \tag{3.14}$$

where D is the cylinder diameter. This accounts for the ratio of the tidal excursion to the cylinder diameter which is analogous to the Keulegan-Carpenter number encountered in wave-structure interaction studies (Keulegan and Carpenter 1958).

3.3.3 Simulation cases

A total of 49 simulations were performed as part of this parametric study to quantify the lateral mixing of passive scalars around a porous obstacle. These simulations

Table 3.1: Summary of simulations presented in this chapter. Note the actual drag coefficients values in the range (0 - 2) are: 0, 0.25, 0.5, 0.75, 1.0, 1.5 and 2.0, respectively.

Case #	Case Name	C_D	η	K	Remarks
1-7	Mean flow	0 - 2.0	0	0	C1 - classical dispersion
8-14	Oscillatory flow	0 - 2.0	1	23	T=4 h
15-21	Oscillatory flow	0 - 2.0	1	46	T=8 h
22-28	Oscillatory flow	0 - 2.0	1	71	M2 tide
29-35	Oscillatory flow	0 - 2.0	0.5	23	T=4 h
36-42	Oscillatory flow	0 - 2.0	0.5	46	T=8 h
43-49	Oscillatory flow	0 - 2.0	0.5	71	M2 tide

span different flow conditions and porosities of obstacles ranging from uni-directional mean flow in the absence of an obstacle to combined uni-directional and oscillatory flows with high drag in the open channel flow domain shown in Figure 3.1. Table 3.1 provides more details on all simulation cases for this study.

Case 1 is referred to as a classical dispersion case and is used to highlight the classical Gaussian behavior of the plume in a uni-directional mean flow in the absence of obstacle-induced drag (C_D=0). In this case, the concentration should decrease monotonically from the source in both lateral and longitudinal directions (Stacey *et al.* 2000). This classical dispersion case is also used to validate the numerical model results with analytical and empirical results of plume dynamics and for relative comparison to other cases with varying flow fields encountering obstacles. Cases 2-7 are also uni-directional mean flows but account for drag forces exerted by porous obstacles. These cases will be used to demonstrate the drag effect of porous obstacles on the lateral mixing of the scalar plume as well as provide a measure of the model sensitivity on C_D.

The remaining cases (cases 8-49) do have an oscillatory flow component in addition to the uni-directional mean flow. These simulations are performed to both qualitatively and quantitatively investigate the effect of all the three non-dimensional

parameters (i.e. η, K and C_D) on the lateral mixing of the plume. For cases 8-28, we explore three different forcing periods (with K values of 23, 46 and 71) and η=1 (i.e. U_m=U_T=0.1 m s^{-1}). For cases 29-49, η=0.5 (i.e. U_m = 0.1 m s^{-1} and U_T = 0.05 m s^{-1}). Note we have restricted η to be no more than 1 intentionally in order to prevent forced flow reversals. We will differ the discussion for cases when $\eta > 1$ (i.e. with flow reversals) to Chapter 4. The drag coefficient C_D is varied from 0 to 2 to simulate different porosities of the obstacle.

For all the simulations, we use vertical and horizontal momentum diffusivities of $\nu = 10^{-5}\ m^2 s^{-1}$ and $\nu_H = 10^{-3}\ m^2 s^{-1}$, respectively to ensure numerical stability. Based on the cylinder diameter of D=20 m, ν and U_m, the Reynolds number $Re_D = 2.0 \times 10^5$, which can be considered to be turbulent.

3.4 Concentration distribution

In this section, the results from all the simulations cases are presented. We first present results of all the steady channel flow cases (cases 1 through 7) to show the lateral mixing of a plume under these conditions. The goal is to highlight the classical behavior of the plume and the enhanced mixing that occurs due to vortices and wakes introduced by flow separation around the obstacle. The results of the combined flow cases (cases 8-49) are then presented and discussed. Parameterizations for the lateral mixing based on all the simulations are also presented in parallel.

The lateral mixing can be characterized by an eddy mixing coefficient usually called the transverse eddy diffusivity (Kay 1990 and Elder 1959). This mixing coefficient can be calculated using the rate of change of the plume width variance σ_y^2 given by

$$\varepsilon_t^* = \frac{1}{2}\frac{\partial \sigma_y^2}{\partial t} = \frac{1}{2}\frac{\Delta \sigma_y^2}{\Delta x}\bar{u}, \tag{3.15}$$

where the time dependence can be recast in terms of the mean velocity $\bar{u}$ and the

distance from the source to a given location Δx. The standard deviation σ_y at any given cross-section can be computed from the time-averaged concentration fields for each of the cases listed in Table 3.1.

3.4.1 Uni-directional mean flow cases

The results from the uni-directional mean flow cases involving only the mean current velocity component with and without drag force are presented in this section. Time-averaged, non-dimensional passive scalar field without cylinder-induced drag force in a uni-directional flow (case 1) is shown in Figure 3.2. The spanwise concentration distributions at sections (a-a), (b-b) and (c-c) are shown in Figure 3.3, respectively. The dashed red line in Figure 3.2 shows the classical spread of the plume width using an empirical lateral mixing coefficient for a uni-directional turbulent flow given by

$$\varepsilon_t / du^* \cong 0.15, \tag{3.16}$$

where d is the channel depth and u^* is the shear velocity (Fischer *et al.* 1979; Bowden 1967; Lau and Krishnappan 1977). It should be noted that the non-dimensional lateral mixing coefficient was in the range of 0.1-0.2 in the experiments and hence 0.15 is considered as an average value. Lateral mixing coefficients obtained from recent laboratory scale experiments on lateral plume mixing by Rummel *et al.* (2005) and Crimaldi and Koseff (2006) are between 0.11 through 0.17, falling within the error bound specified above.

It is well known from experiments (Lau and Krishnappan 1977; Fischer *et al.* 1979; Bowden 1967) and direct numerical simulations of channel flows (see for example Hoyas and Jimenez 2006) that the mean velocity U is approximately $25u^*$. Using this relationship, gives a value for $\epsilon_t = 0.03$ m^{2}s^{-1}. This is in good agreement with the lateral diffusivity of 0.026 m^{2}s^{-1} computed from the variances of the concentration

distributions shown in Figure 3.3.

It can be seen from Figure 3.2 that the plume linearly grows with $x^{1/2}$ in the flow direction as described in Equation (3.6) for a Gaussian plume. Also, all the concentration profiles at the cross sections shown in Figure 3.3 show close agreement with the Gaussian plume (see also Equation (3.5)). However, there is some divergence from the purely Gaussian case. This is probably a consequence of the averaging from the numerical simulations. It takes a lot of ensembles to get pure Gaussian plots in experiments and numerical simulations. Regardless, these results serve to validate the numerical model and hence provide us with the confidence to use the SUNTANS model for further numerical studies on mixing and transport of passive scalars under different flow conditions.

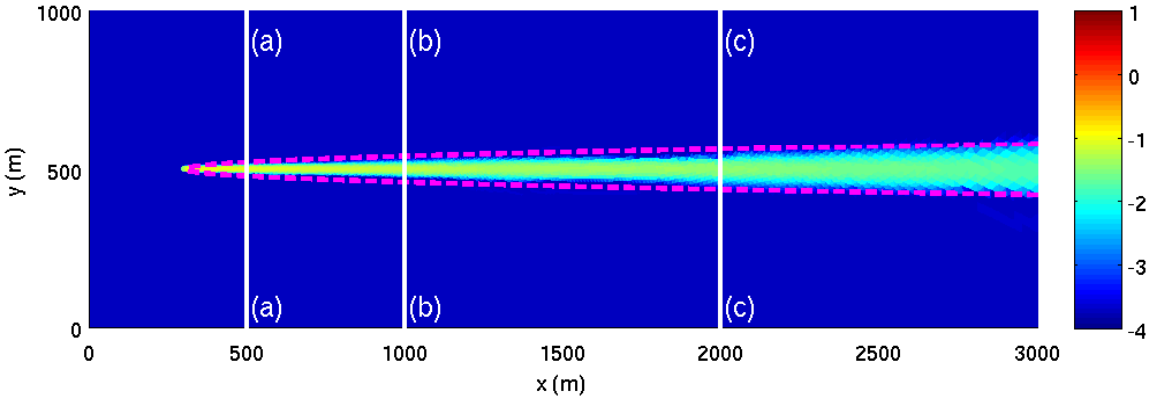

Figure 3.2: Time-averaged normalized concentration field (shown in color) for a steady uni-directional test flow case (case 1 in Table 3.1). The dashed red line shows the classical spread of a Gaussian plume using a lateral diffusivity of 0.03 m^2s^{-1}.

Figure 3.4 shows the time-averaged non-dimensional concentration fields for cases 2-7. The fields show a view closer to the cylinder ($200 \leq x \leq 1300$ m and $200 \leq y \leq 800$ m) in order to highlight the plume characteristics in the vicinity of the porous obstacle. It can be clearly seen that the presence of the porous obstacles has enhanced the lateral spread of the plume. An example snapshot of the instantaneous concentration fields at $t = 10$ hours is shown in Figure 3.5. The enhanced mixing

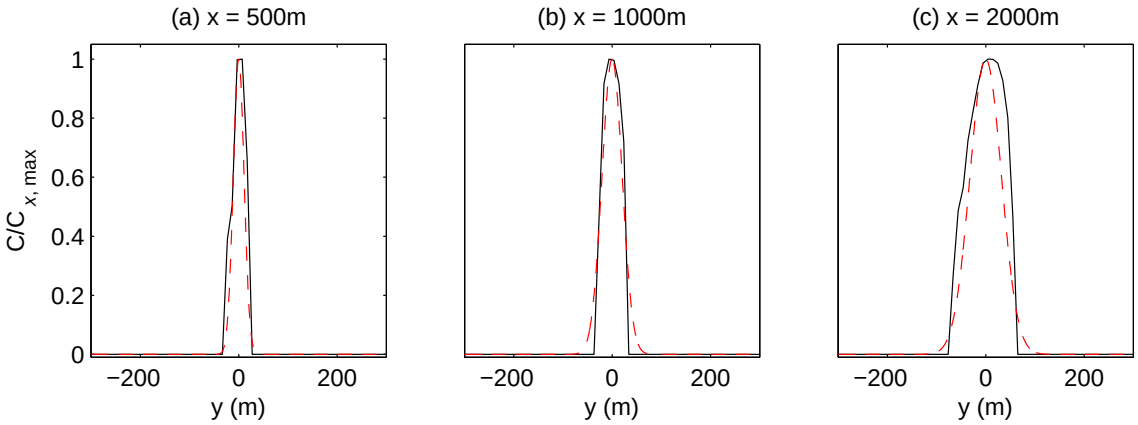

Figure 3.3: Time-averaged concentration distributions for case 1 in Table 3.1 at (a) $x = 500$ m, (b) $x = 1000$ m, and (c) $x = 2000$ m. The dashed red lines shows are the Gaussian profiles calculated using the empirical transverse mixing coefficient $\varepsilon_t = 0.15du^*$.

evident here has also been observed in laboratory experiments on dye dispersion by Rummel *et al.* (2005). Nepf (1999) obtained high turbulent diffusivities for flow through emergent vegetation and attributes this to the blocking effect caused by the stems.

Essentially, the presence of the obstacle blocks the flow thereby causing a deceleration of the approaching flow and the formation of downstream vortices and wakes. These downstream vortices and wakes lead to the complex patterns of the contaminant distribution as shown in Figures 3.4 and 3.5, respectively. More porous obstacles (i.e. with $C_D < 1$) exhibit lesser blocking effect since substantial amount of flow can pass through the obstacle. This clearly delays flow separation and the vortex shedding as can be seen in Figure 3.5(a)-(c). On the other hand, when the porosity is reduced (i.e. for higher C_D), the blocking effect is now stronger which promotes flow separation and development of the vortex-wake field much quicker and closer to the cylinder (see Figure 3.5(d)-(f)). Hence, different vortex patterns emerge in the vicinity of the obstacles depending on porosity of the obstacles, an observation that was also made in a recent numerical study of flow through a circular array of cylinders (Nicolle and Eames 2011). Lateral mixing is clearly enhanced as the drag

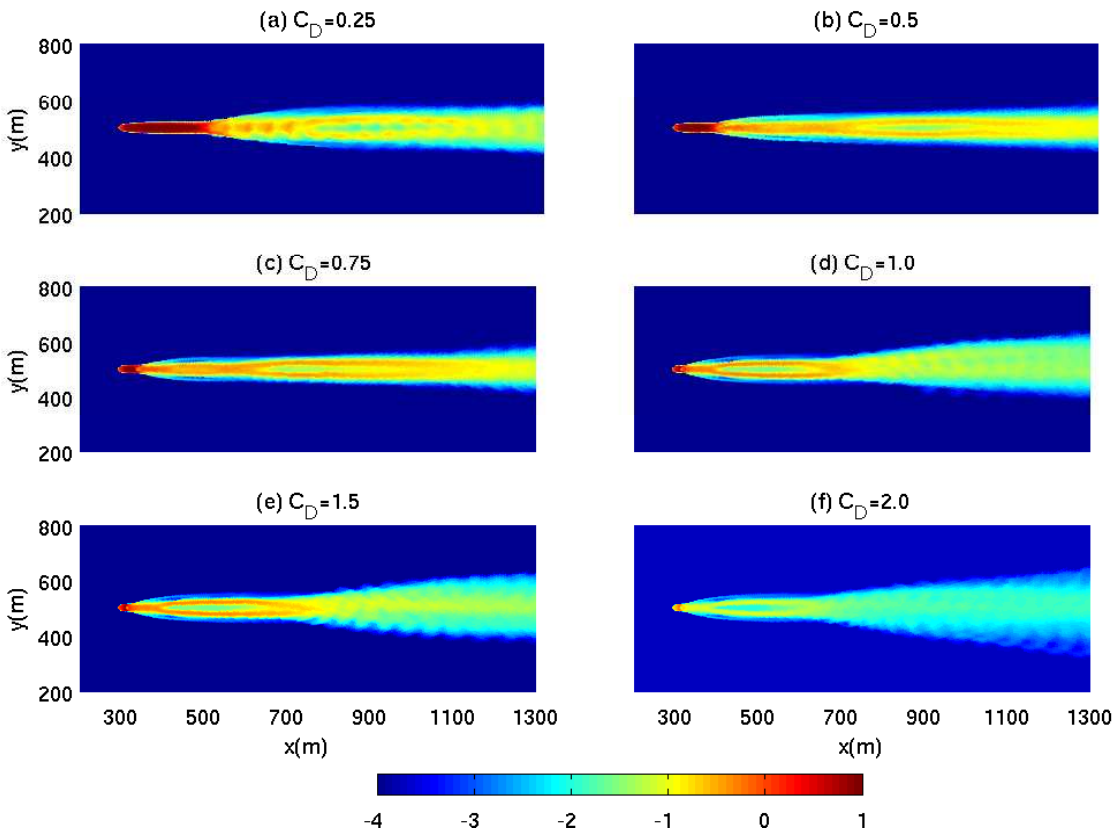

Figure 3.4: Time-averaged non-dimensional concentration field for the mean flow cases (cases 2-7) with non-dimensional drag coefficients of (a) $C_D = 0.25$, (b) $C_D = 0.5$, (c) $C_D = 0.75$, (d) $C_D = 1.0$, (e) $C_D = 1.5$ and (f) $C_D = 2.0$.

from the obstacle increases as seen in both the time-averaged and instantaneous fields in Figures 3.4 and 3.5, respectively.

Figure 3.5 also shows how the wake field gradually begins to transition from a rather disordered (unstable) state of a staggered row of vortices to more stable in-phase vortex state that eventually merge further downstream due to far-field turbulent mixing. Based on these observations and the ideas presented in Williamson (1985), it is plausible to classify the characteristic of the vortex-wake field into three distinct regions, namely: a separation region of length l_s; an in-phase vortex region of length l_t; and a binary vortex street region. Figure 3.6 shows a schematic sketch of these three regions. Note the separation region is identified by a length l_s which is the distance from the obstacle to flow separation, the in-phase vortex region is defined

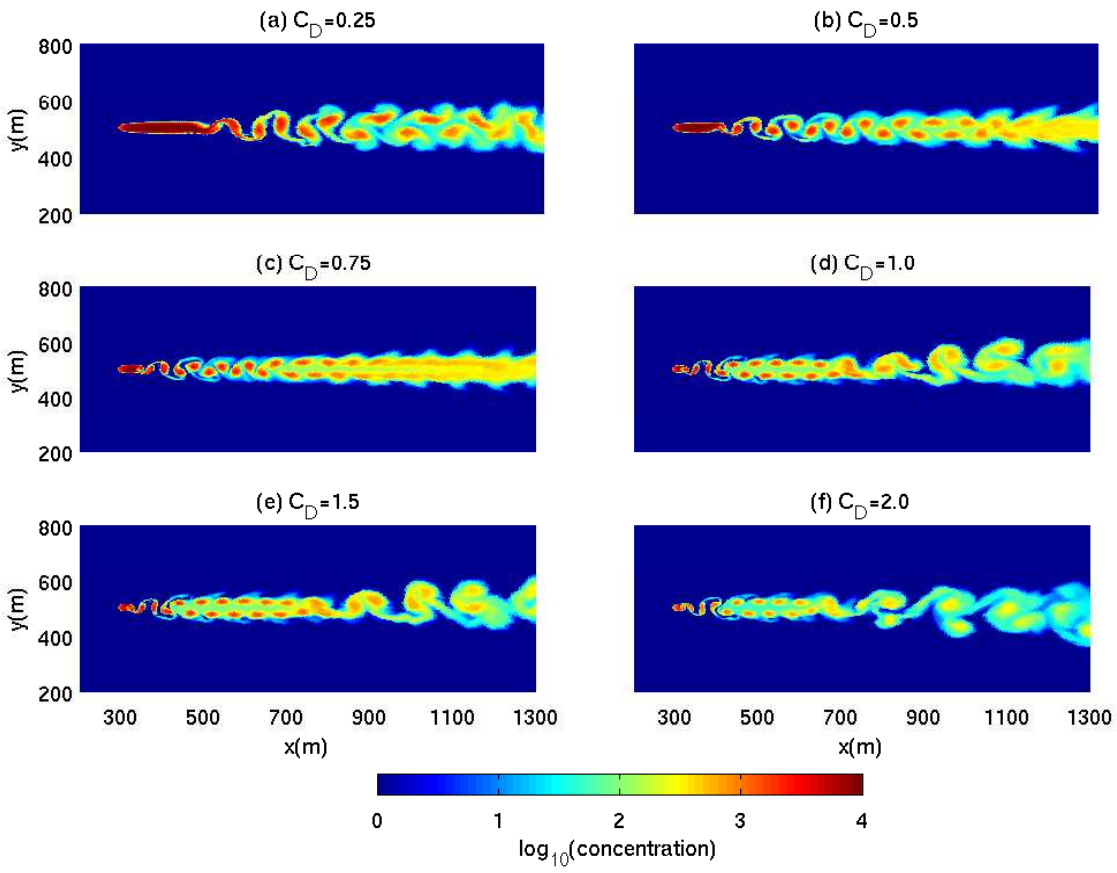

Figure 3.5: Instantaneous non-dimensional concentration field for the mean flow cases (cases 2-7) at time $t = 10$ h with non-dimensional drag coefficients of (a) $C_D = 0.25$, (b) $C_D = 0.5$, (c) $C_D = 0.75$, (d) $C_D = 1.0$, (e) $C_D = 1.5$ and (f) $C_D = 2.0$.

by a length l_t which is the distance covered by the non-staggered row of vortices, and finally the binary vortex region is region where a consistent staggered row of vortices are observed, respectively.

As discussed above, more porous obstacle cases ($C_D < 1$) permit greater through flow and hence delay the onset of separation and recirculation due to the inertia of the flow field. Eventually, the flow separation occurs and a recirculation region appears as shown in Figure 3.5(a)-(c). Note how the length of the separation region (l_s) decreases as C_D increases and asymptotes to a constant value of the order of the obstacle diameter. The flow separation triggers the shedding of alternating (i.e. non-staggered) vortices which are found to be quite unstable. Again, the length of

this in-phase vortex region l_t is found to decrease dramatically as C_D increases and approaching an asymptotic value of about $l_t \simeq 5D$ for $C_D > 1$, where D is the diameter of the obstacle. The in-phase vortex region transitions into a binary vortex region that comprises of a staggered row of vortices. It has been found from earlier work by Von Karman that these vortices are stable only when the ratio of the lateral to longitudinal scales of the vortices are greater than 0.28 (Kundu and Cohen 2008). We use these characteristic vortex patterns to quantitatively define the lengths of the first two regions shown in the schematic in Figure 3.6.

Figure 3.7 shows the non-dimensional lengths l_s/D and l_t/D for the separation region and the in-phase vortex regions, respectively, as a function of the drag coefficient C_D. Note the lengths of these regions are infinite for the classical dispersion case ($C_D = 0$). The lengths quickly decrease and converge to $l_s/D = 1$ and l_t/D=5 for $C_D > 1$. These results are in agreement with the longitudinal dispersion in a random array of cylinders where the recirculation region was found to be of the order of diameter of the solid cylinder (White and Nepf 2003). Clearly, the development of these regions are a strong function of C_D and are found to decrease exponentially

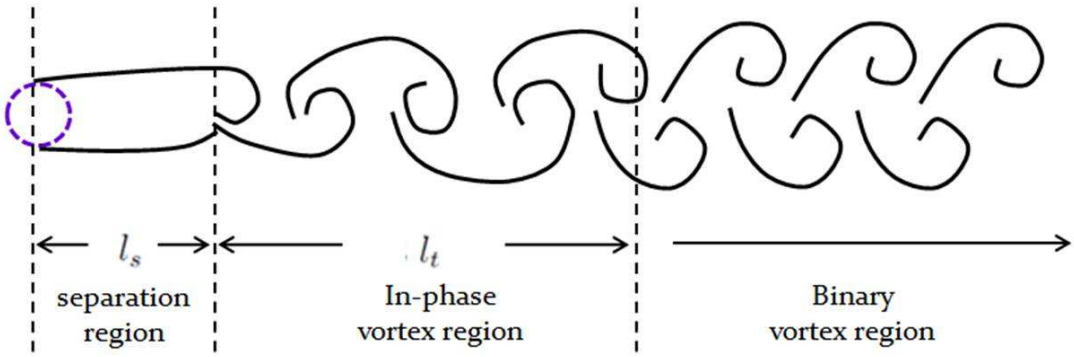

Figure 3.6: Schematic sketch of vortex patterns around a cylindrical obstacle depicting the separation region, the in-phase vortex region, and binary-vortex region, respectively.

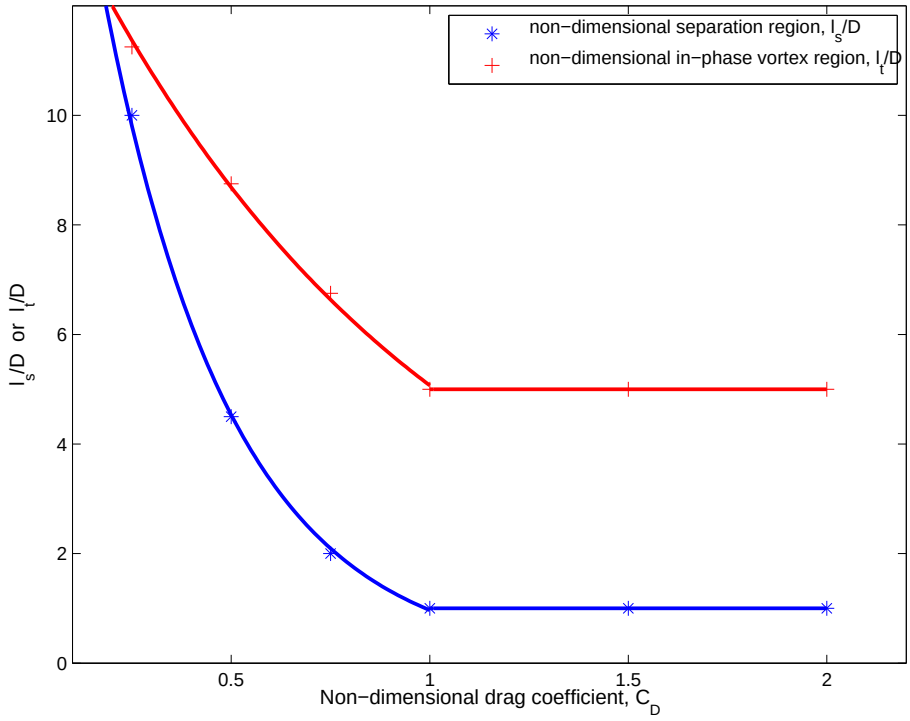

Figure 3.7: Lengths of separation and in-phase vortex regions. Blue asterisks and red crosses show the normalized separation region length l_s/D and in-phase vortex region l_t/D for the uni-directional mean flow cases ($\eta = 0$, cases 1 through 7 in Table 3.1).

with C_D as follows

$$l/D \cong \gamma \exp\left(\beta C_D\right), \tag{3.17}$$

where γ is a scale factor and β is an exponential constant. For ease of interpretation, we will use γ_s, β_s to denote the values for the separation region and γ_t, β_t for the in-phase vortex region. $\beta_s = -3.1$ and $\beta_t = -1.1$ with $\gamma_s = 21$ and $\gamma_t = 15$. The separation region decays 3 times faster than the in-phase vortex region.

The spanwise concentration distribution at $x = 500,\ 700,\ 1000$, and 1250 m for cases 2-7 are shown in Figure 3.8. The concentrations are normalized by the maximum value of concentration among all of the cases 1-7, in order to show the effect of the obstacles on pollutant dispersion. These profiles highlight how the plumes for all the cases (under the influence of obstacle-induced drag) begin to depart quite early (at x=500 m) from the classical Gaussian plume (case 1,dotted-dashed red in Figure 3.8).

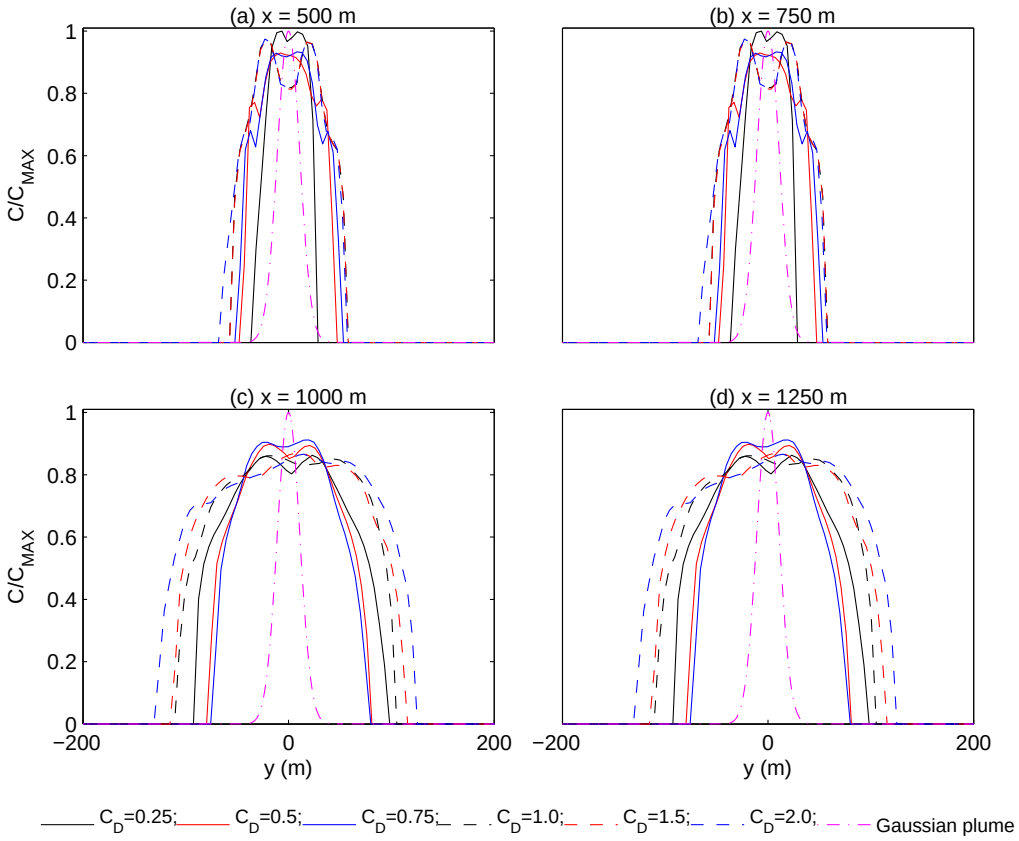

Figure 3.8: Time-averaged non-dimensional spanwise concentration for the mean flow cases ($\eta = 0$, cases 2 - 7 in Table 3.1) at (a) $x = 500$ m, (b) $x = 750$ m, (c) $x = 1000$ m, (d) $x = 1250$ m. The dotted-dashed red line shows the Gaussian plume.

For the more porous obstacles with $C_D < 1$, the separation region is extended over at least a diameter length of the obstacle and hence the plume exhibits a similar behavior to the classical dispersion case. The averaged lateral diffusivities computed using concentration variances in the separation region are approximately $0.034 - 0.036$ $\mathrm{m^2 s^{-1}}$, which are in good agreement with the empirical diffusivity for classical dispersion. For the purposes of quantifying an overall lateral mixing coefficient, the separation region is ignored. The lateral mixing coefficients are therefore obtained using the time-averaged spanwise concentration profiles between the in-phase and the binary vortex regions. The coefficients computed from the numerical simulations are shown in Table 3.2. The last column shows the normalized values using the empirical value of $\varepsilon_t/du^* \cong 0.15$ (Equation (3.16)) for the classical dispersion case. These values are about 3 to 5 times larger than the lateral mixing coefficient computed for the classical dispersion.

Figure 3.9 depicts these results graphically as a function of C_D and shows the enhanced effect of the drag forces imparted by the porous obstacles on the scalar plume dynamics. A least squares regression fit to the data provides a relationship of the form

$$\varepsilon_t^*/\varepsilon_t = \lambda \exp\left(-\frac{1}{5C_D}\right) + 1, \tag{3.18}$$

where λ is a constant scaling factor. For ease of presentation as far tying these results to the oscillatory flow cases (cases 8-49), we shall denote the scaling factor for the mean flow cases as λ_0 since $\eta = 0$. The best fit value was found to be $\lambda_0 = 5$. Equation (3.18) captures the pattern of the lateral mixing coefficients which for all intents and purposes asymptote a constant when $C_D \geq 1$. However, the coefficients grow in an exponential manner for $0 < C_D \leq 0.25$. Overall, the results for these mean flow cases highlight how the lateral mixing is enhanced in the presence of obstacles and show the importance for studying the influence of obstacles on the plume dispersion.

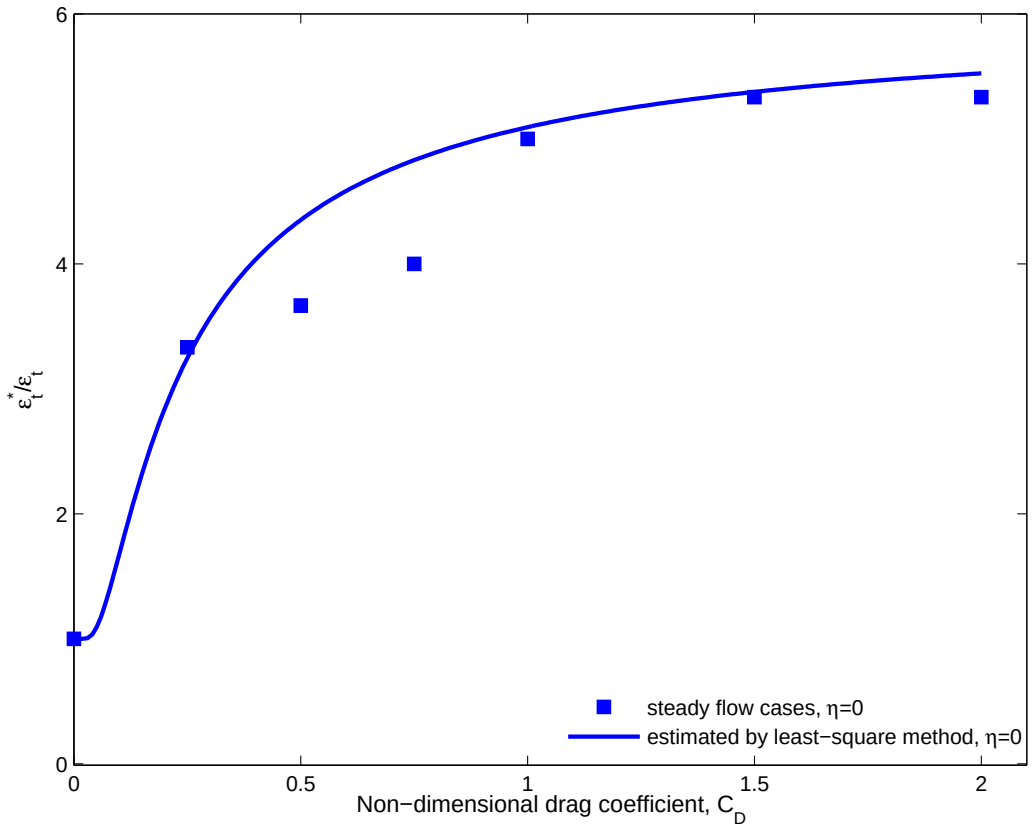

Figure 3.9: Time-averaged non-dimensional lateral mixing coefficients for mean flow cases ($\eta = 0$, cases 1 through 7 in Table 3.1). They are normalized by the empirical transverse mixing $\varepsilon_t \cong 0.15du^*$. Blue squares are computed from the simulation and blue line shows the exponential relation given by Equation (3.18) for $\lambda_0 = 5$ (as listed in Table 3.5).

Table 3.2: Time-averaged lateral mixing coefficients for the mean flow cases shown in Table 3.1, $\eta = 0$.

Case No.	C_D	ε_t^* $(m^2 s^{-1})$	$\varepsilon_t^*/\varepsilon_t$
1	0	0.03	1.00
2	0.25	0.10	3.33
3	0.5	0.11	3.67
4	0.75	0.12	4.00
5	1.0	0.15	5.00
6	1.5	0.16	5.33
7	2.0	0.16	5.33

3.4.2 Combined mean and oscillatory flow cases

Results of simulation cases 8-49 are presented here. The ratio of the tidal to mean velocity amplitudes are $\eta = 1$ for cases 8-28 and $\eta = 0.5$ for cases 29-49. As pointed out earlier, the value of the shape parameter has been chosen such that no forced flow reversals occur in these simulations, thus allowing for a direct comparison with the mean flow cases presented in Section 3.4.1. Three different values of the tidal excursion parameter K: 23, 46 and 71, are used and correspond to forcing periods of 4 hours, 8 hours and 12.42 hours ($M2$ tide), respectively. Cases 8-28 ($\eta = 1$) are discussed first to show the influence of a stronger tidal signal, followed by a somewhat similar discussion of cases 29-49, which corresponds to a weaker tidal forcing amplitude ($\eta = 0.5$).

Cases 8-28: $\eta = 1$

Figures 3.10 and 3.11 show the time sequence using the non-dimensional concentration fields of the passive scalars for case 12 and case 19, respectively. In both figures, the mixing and transport of a continuous scalar point source collocated within the obstacle (with $C_D = 1$) are shown using a time sequence of the concentration field over a duration of nearly two tidal periods. The tidal excursion parameters are $K = 23$ ($T = 4$ hours) for case 12 and $K = 46$ ($T = 8$ hours) for case 19. When the tidal component is in phase with the mean current, the flow evolves in a similar manner to the uni-directional mean flow cases (e.g. case 5) with the usual formation of an unstable downstream wake resulting in vortex shedding (Figures 3.10(a),(b) and 3.11(a),(b)). Soon after the initial vortex shedding begins, the flow starts to retard as the tidal velocity reverses direction and increases in amplitude. This causes the plume to contract in the longitudinal direction with a simultaneous dispersion in the lateral direction as shown in Figures 3.10(c),(d) and 3.11(c),(d), and during the subsequent tidal cycle as shown in Figures 3.10(g),(h) and 3.11(g),(h), respectively.

Note how the vortex shedding is also attenuated during this period. This behavior was first described by Chatwin (1975), where he points out that the contaminant cloud appears to be periodically expanding and contracting. The plume is stretched during the period of high flow during the first half of the tidal cycle and contracts during the second half-cycle. The longer tidal period (case 19 with K=46) results in a slightly more dispersed plume compared to the case with the shorter tidal period (case 12).

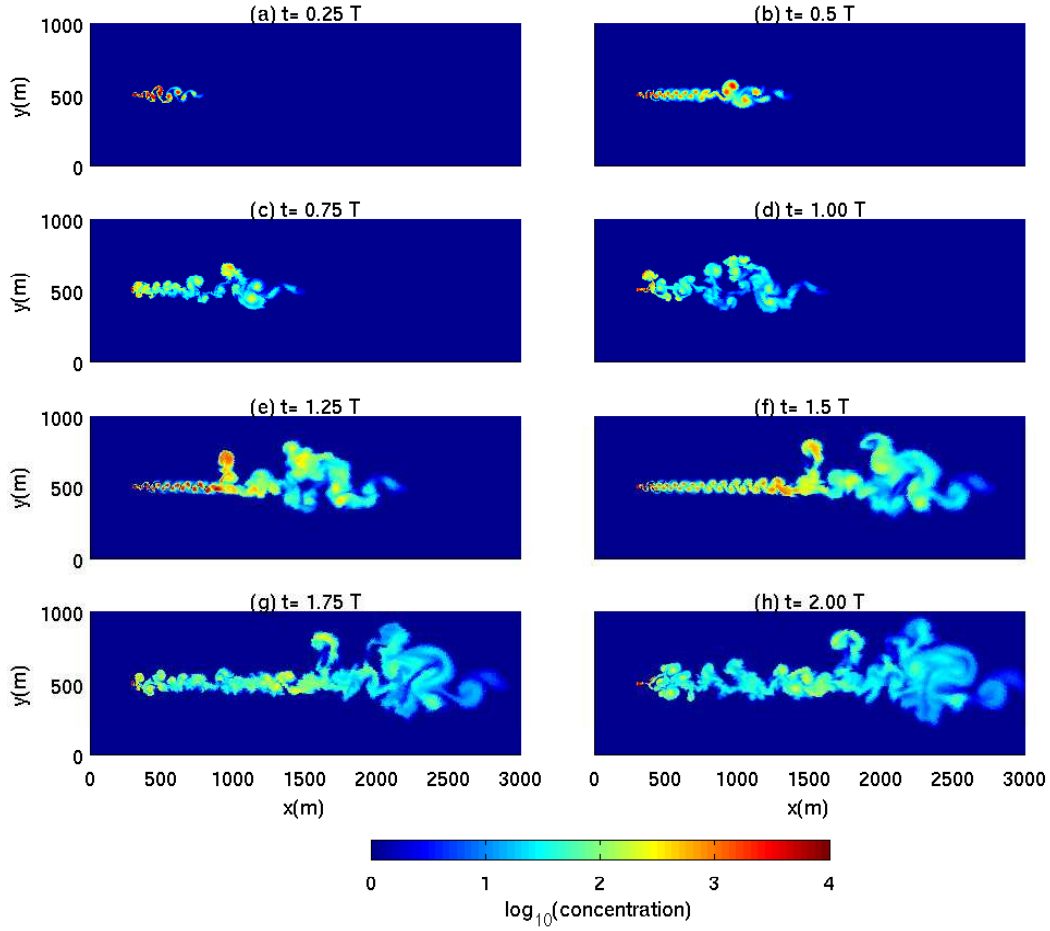

Figure 3.10: Instantaneous scalar concentration field (shown in color) for a porous obstacle with a drag coefficient of $C_D = 1.0$ under the combined action of the mean and tidal velocity components for two tidal periods ($\eta = 1$, $K = 23$ case 12 in Table 3.1). The continuous point source is located within the perimeter of the cylindrical obstacle. Time is normalized by the tidal period $T = 4$ h.

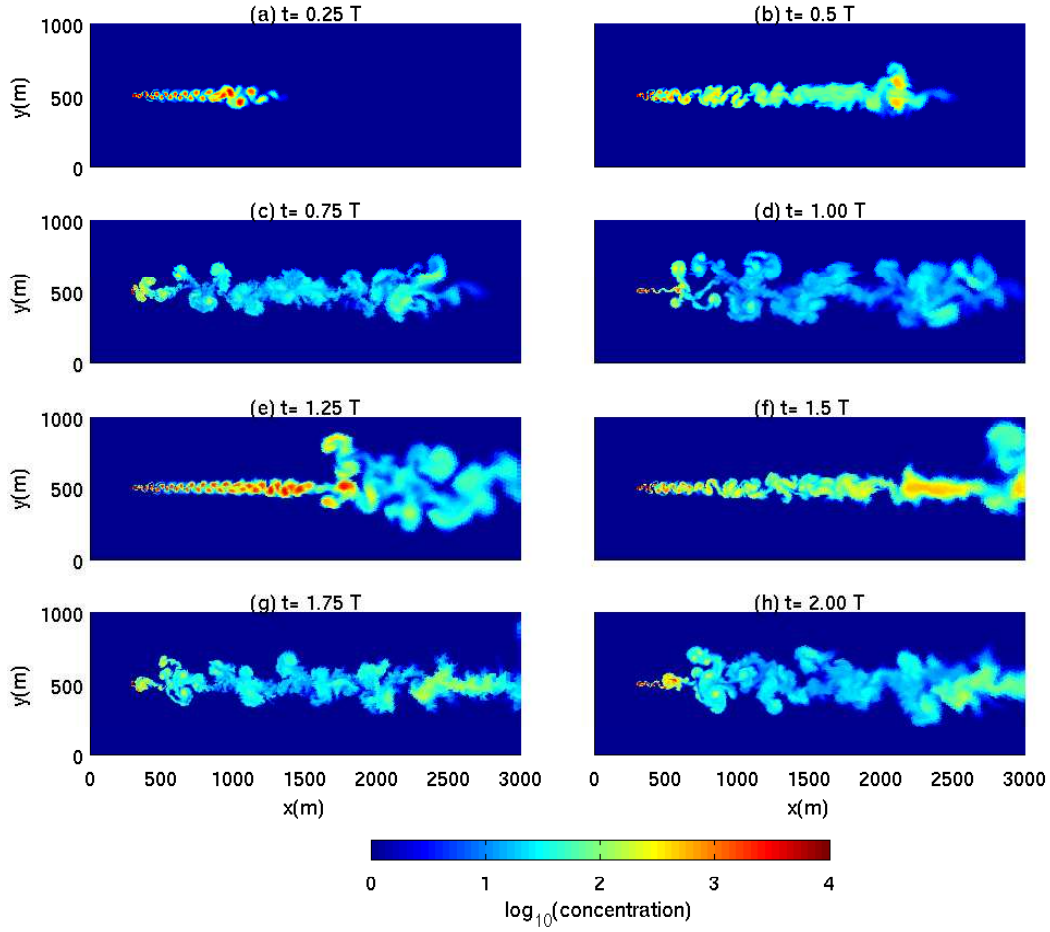

Figure 3.11: Instantaneous scalar concentration field (shown in color) for a porous obstacle with a drag coefficient of $C_D = 1.0$ under the combined action of the mean and tidal velocity components for two tidal periods ($\eta = 1$, $K = 46$ case 19 in Table 3.1). The continuous point source is located within the perimeter of the cylindrical obstacle. Time is normalized by the tidal period $T = 8$ h.

The time-averaged concentration fields for cases 8, 15, and 22 (with $C_D = 0$) are shown in Figure 3.12 (a)-(c). Since there is no flow reversal for $\eta = 1$, the passive scalar fields are very similar to the classical dispersion plume (case 1) except for noticeable contractions during the second half cycle of tides. It can be easily seen that distances between the contractions depend on the different tidal frequencies while the overall transport patterns are independent of the forcing period (i.e. the lateral mixing coefficients are more or less the same for cases 1, 8, 15, and 22 (see Tables 3.2 and 3.3 for details).

As expected, the concentration fields quickly become very different once the porous obstacle is introduced into the flow field. The lateral mixing is substantially enhanced as shown in Figures 3.13 and 3.14. The slight asymmetry in the time-averaged concentration fields in these figures is due to the finite number of tidal cycles over which the averaging is performed. This results in a distribution that is skewed in the direction of a set of counter-rotating vortices that emerge in the positive y-direction upon the first tidal reversal, as depicted in Figures 3.10(c),(d) and 3.11(c),(d). As shown in Figures 3.10(e),(f) and 3.11(e),(f), these counter-rotating vortices move in the positive y-direction, thereby causing a skew in the averaged concentration field. Subsequent ejections of counter-rotating vortices are not as strong and therefore, opposite-signed vortices do not counteract the effect of the first pair unless many more tidal cycles are computed. We should also note that the asymmetry is accentuated by the logarithmic concentration contours. Regardless, these results indicate that the mixing and dispersion of the passive field under oscillatory flow conditions with obstacle-induced drag is very different (and enhanced) from a classical uni-directional flow case as well oscillatory flow cases without obstacle-induced drag (cases 1, 8, 15 and 22). It is also worth noting that the plume growth for these cases is further enhanced compared to the uni-directional mean flow cases (cases 2-7), indicating that the combined action of obstacle-induced drag and oscillations in the flow field is very effective in mixing

the plume laterally. This observation can easily be verified by comparing the lateral mixing coefficients for the oscillatory flow cases with those for cases 2-7.

Furthermore, the time-averaged scalar fields show the effect of the different tidal excursion length scales on plume dispersion. The tidal forcing period affects both the magnitude and extent of a plume from a point source. The scalar field is concentrated in near-field and close to the center line for the cases with shorter tidal excursion scales in conjunction with a lower drag coefficient.

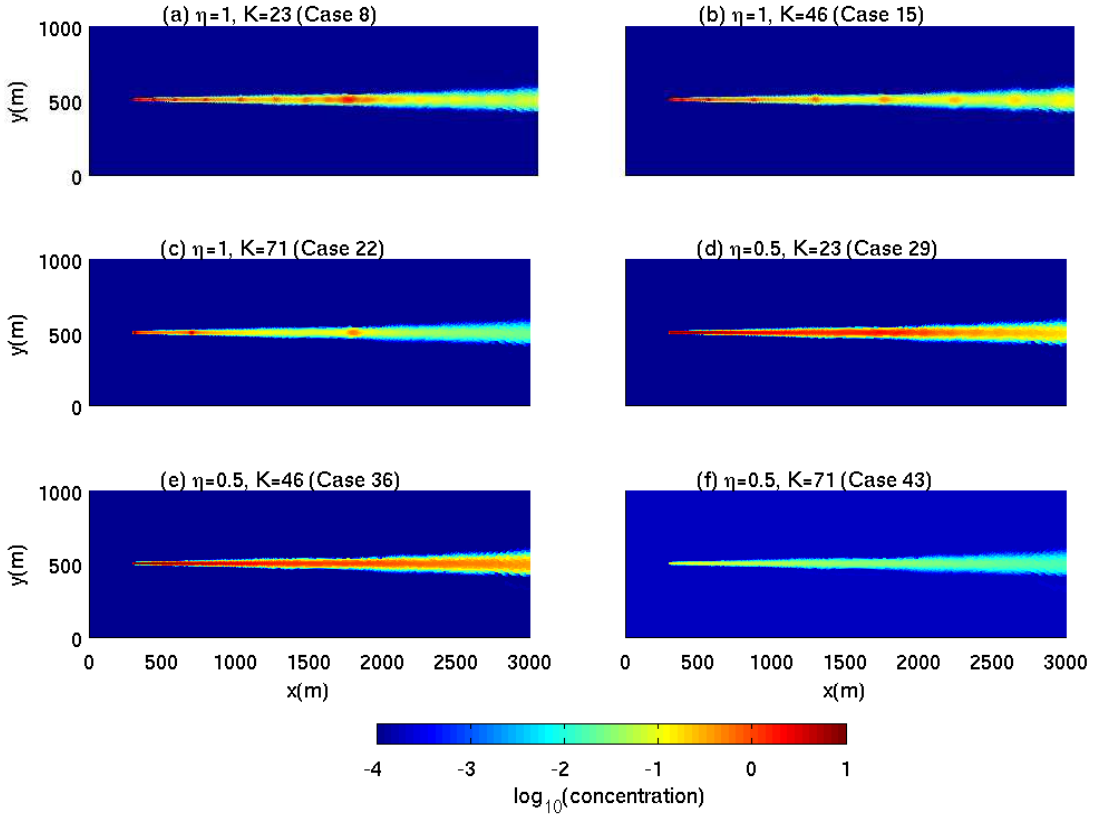

Figure 3.12: Time-averaged non-dimensional concentration fields without drag for (a) case 8, (b) case 15, (c) case 22, (d) case 29, (e) case 36 and (f) case 43, respectively.

The lateral scalar diffusivities obtained from the simulations results using Equation (3.15) are listed in Table 3.3 and shown plotted versus the drag coefficient in Figure 3.15. Note separate fitted curves are used for each K value. The mixing coefficient increases dramatically with increasing C_D until about $C_D = 1$. Beyond this,

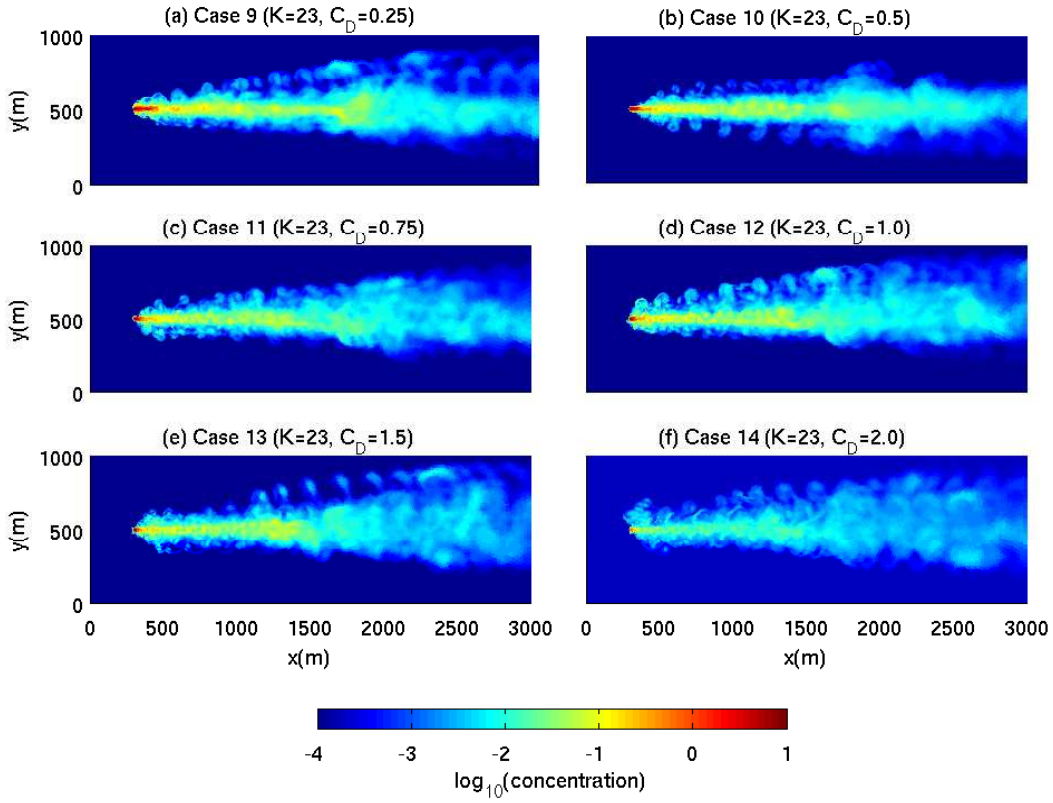

Figure 3.13: Time-averaged non-dimensional concentration field under the combined action of mean and oscillatory velocity components for a forcing period of $T = 4$ h ($K = 23$) with drag coefficients of (a) $C_D = 0.25$, (b) $C_D = 0.5$, (c) $C_D = 0.75$, (d) $C_D = 1.0$, (e) $C_D = 1.5$ and (f) $C_D = 2.0$.

the mixing coefficients begin to level out asymptotically and approach a constant λ (see Table 3.5 for relevant values). These curves are also given by Equation (3.18) but with different λ values from the mean flow cases. These results clearly show how the lateral mixing is greatly enhanced in the presence of the obstacles under the combined effect of the mean and the oscillatory flows. They also show the effect of the different forcing periods on the mixing.

Cases 29-49: $\eta = 0.5$

The results for simulation cases (29-49) with $\eta = 0.5$ are presented here to show the effect of a smaller shape factor on the plume dynamics. The mean amplitude U_m of

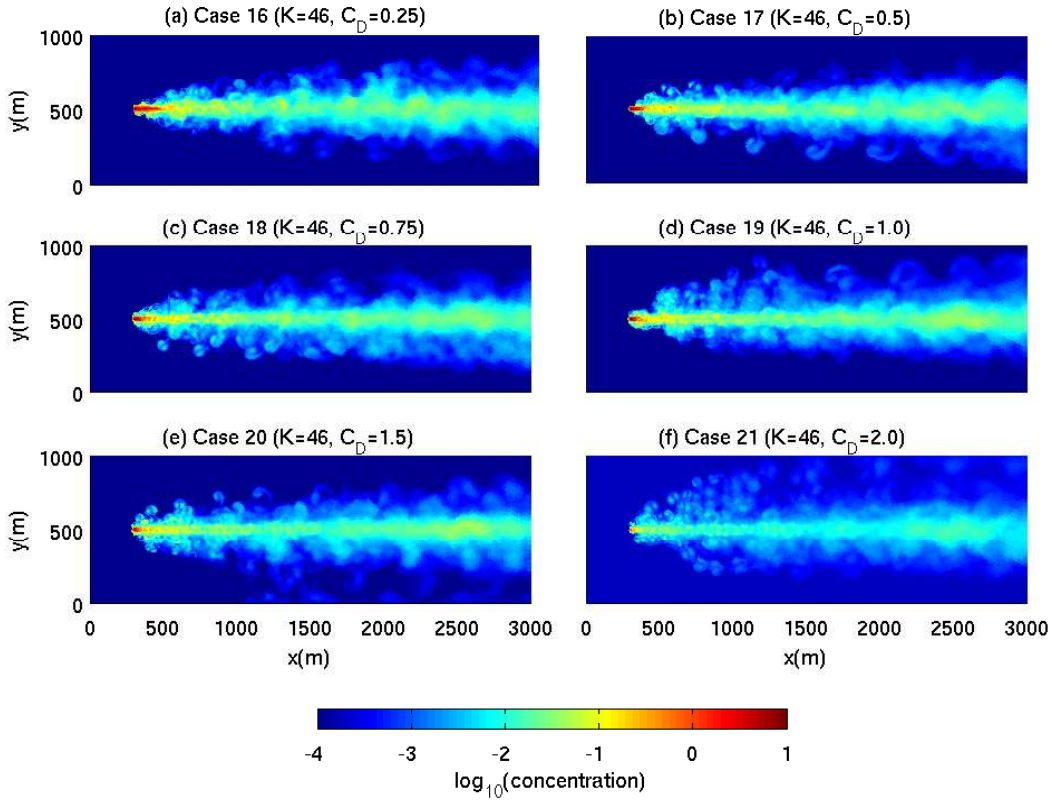

Figure 3.14: Time-averaged non-dimensional concentration field under the combined action of mean and oscillatory velocity components for a forcing period of $T = 8$ h ($K = 46$) with drag coefficients of (a) $C_D = 0.25$, (b) $C_D = 0.5$, (c) $C_D = 0.75$, (d) $C_D = 1.0$, (e) $C_D = 1.5$ and (f) $C_D = 2.0$.

the flow is twice as fast as the tidal amplitude U_T and hence, the effect of the tidal component in our model problem as prescribed by Equation (3.10) should be less stronger than for the $\eta = 1$ cases discussed in the previous section.

In Figure 3.12(d)-(f), the time-averaged scalar fields are shown for the cases without obstacle-induced drag (cases 29, 36 and 43). The distributions are again very similar to the classical dispersion plume (case 1) as well to those for cases 8, 15 and 22, respectively. However, the contractions during the second half cycle of tides are less noticeable as can be seen by comparing Figure 3.12(d)-(f) with Figure 3.12(a)-(c)). However, there is no noticeable difference in the overall time-averaged lateral mixing coefficients (see Table 3.4 for details).

Table 3.3: Time-averaged lateral mixing coefficients for oscillatory flow cases 8-28 with $\eta = 1$ shown in Table 3.1.

Case No.	K	C_D	ε_t^* $(m^2 s^{-1})$	$\varepsilon_t^*/\varepsilon_t$
8	23	0	0.03	1.00
9	23	0.25	0.59	19.67
10	23	0.5	0.69	23.00
11	23	0.75	0.76	25.33
12	23	1.0	0.79	26.33
13	23	1.5	0.82	27.33
14	23	2.0	0.84	28.00
15	46	0	0.03	1.00
16	46	0.25	0.64	21.30
17	46	0.5	0.72	24.00
18	46	0.75	0.87	29.00
19	46	1.0	0.97	32.3
20	46	1.5	1.11	37.00
21	46	2.0	1.15	38.30
22	71	0	0.03	1.00
23	71	0.25	0.65	21.67
24	71	0.5	0.99	33.00
25	71	0.75	1.10	36.67
26	71	1.0	1.12	37.33
27	71	1.5	1.22	40.67
28	71	2.0	1.31	43.67

A time sequence of the instantaneous scalar field for case 40 is shown in Figure 3.16 over two tidal periods. All simulation parameters are identical to the sequence shown in Figure 3.11 except for the shape factor. The effect of the stronger tidal forcing in Figure 3.11 is no longer evident at different times in the flow. Quantitative evidence of the effect of the shape factor comes from the lateral mixing coefficients that were computed from the time-averaged scalar fields in an analogous manner to the previous cases.

The time-averaged fields for $\eta = 0.5$ and $K = 46$ ($T = 8$h) for different C_D values are shown in Figure 3.17 to highlight the effect of the porosity of an obstacle on plume dispersion. Figure 3.18 shows the time-averaged fields for three different forcing periods. Both of these figures confirm the earlier findings that the mixing and

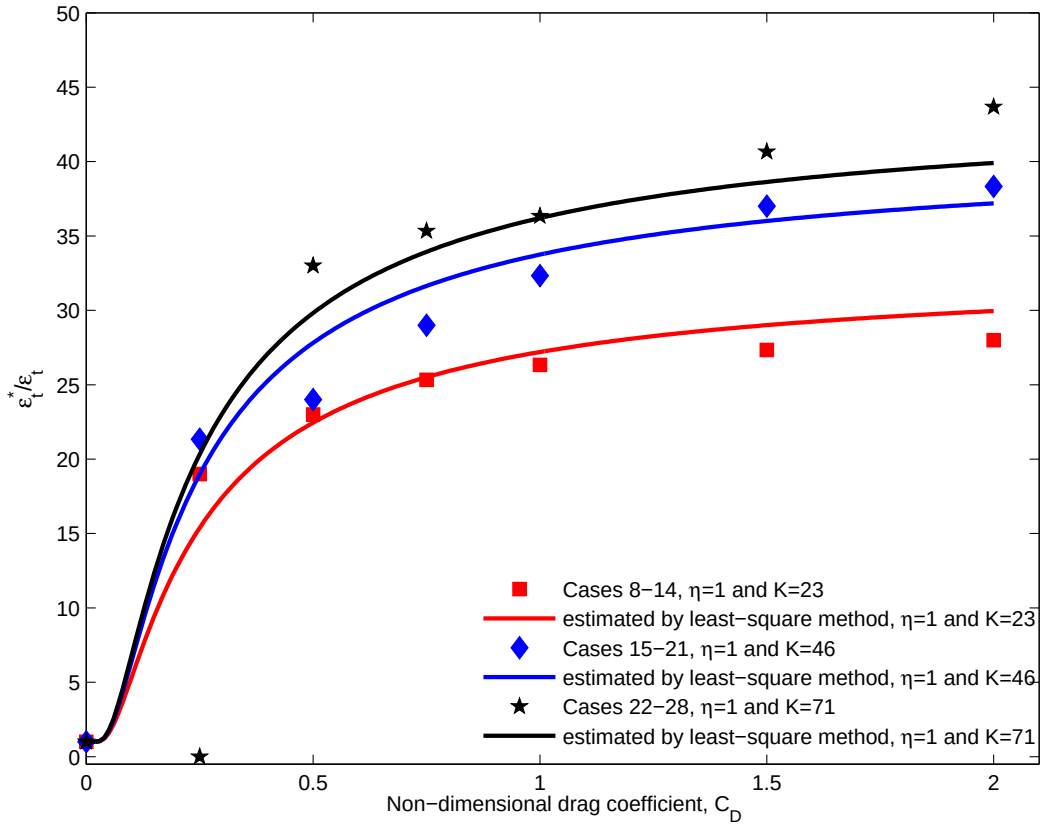

Figure 3.15: Time-averaged lateral mixing coefficients for the combined flow cases ($\eta = 1$, cases 8 through 28 in Table 3.1). They are normalized by the empirical transverse mixing $\varepsilon_t \cong 0.15du^*$. The red squares, blue diamonds, and black stars are computed from the numerical simulations and the associated colored lines show the exponential relation given by Equation (3.18) for the relevant values of λ listed in Table 3.5.

dispersion of a passive field under oscillatory flow conditions with obstacle-induced drag is greatly enhanced from the classical uni-directional flow case as well oscillatory flow cases without obstacle-induced drag (see Figure 3.12).

The lateral scalar diffusivities obtained from the simulations results using Equation (3.15) are listed in Table 3.4 and shown plotted versus the drag coefficient in Figure 3.19. Note separate fitted curves are used for each K value. The mixing coefficient increases dramatically (but not as fast as for the cases shown in Figure 3.15 with increasing C_D until about $C_D = 1$). As observed previously, the mixing coefficient begins to level out asymptotically and approach a constant λ (see Table

3.5 for relevant values). Again, these curves are also given by Equation (3.18) but with different λ values from the mean flow cases. There is at least a 25% reduction in the largest λ values for the $\eta = 0.5$ cases compared to $\eta = 1$ cases (as shown in Table 3.5). Furthermore, the decrease in the shape factor has also clearly reduced the effect of the different tidal forcing frequencies as can be seen by comparing Figure 3.19 with Figure 3.15.

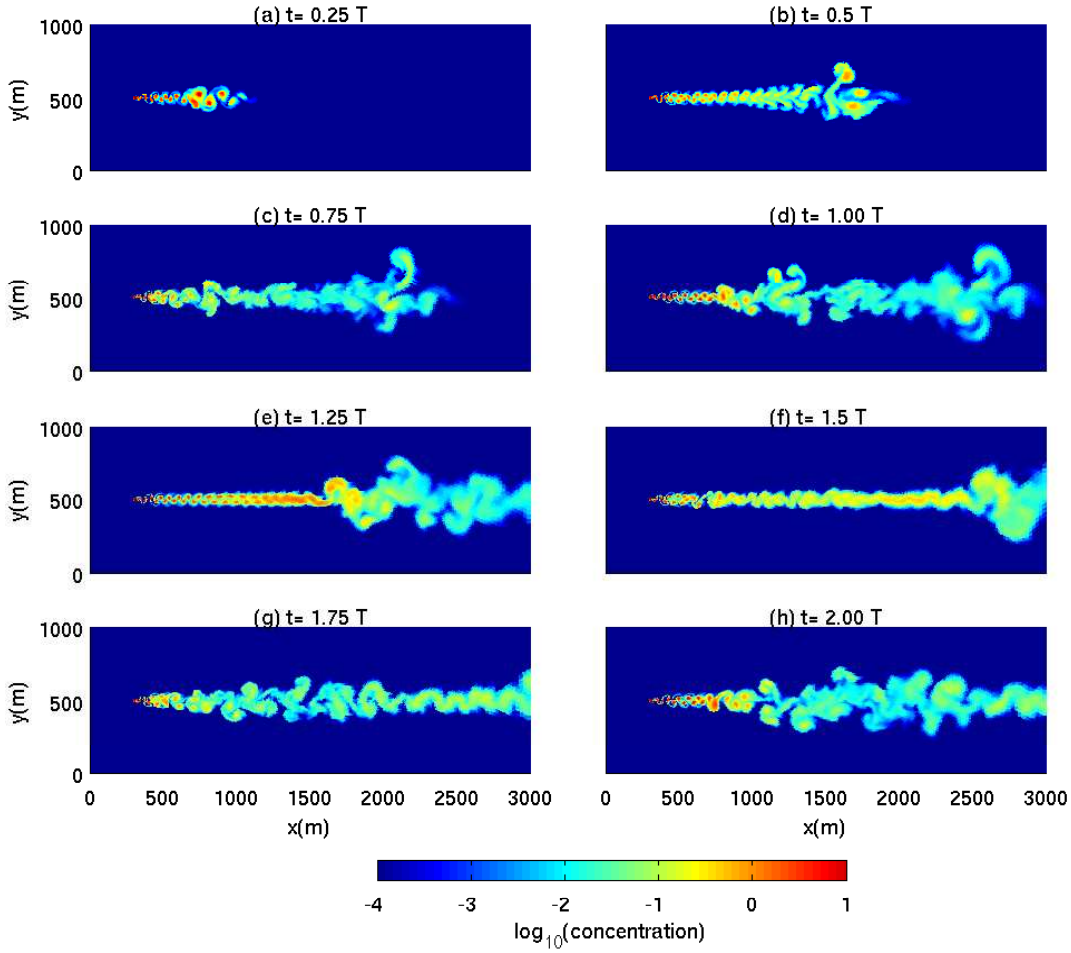

Figure 3.16: Non-dimensional concentration field with the drag on the non-dimensional drag coefficient of $C_D = 1.0$ under the combination of the steady and the oscillatory flows ($\eta = 0.5$, $K = 46$, case 40 in Table 6.1). The continuous point source is located within the perimeter of the cylindrical obstacle. Time is normalized by the tidal period $T = 8$ h.

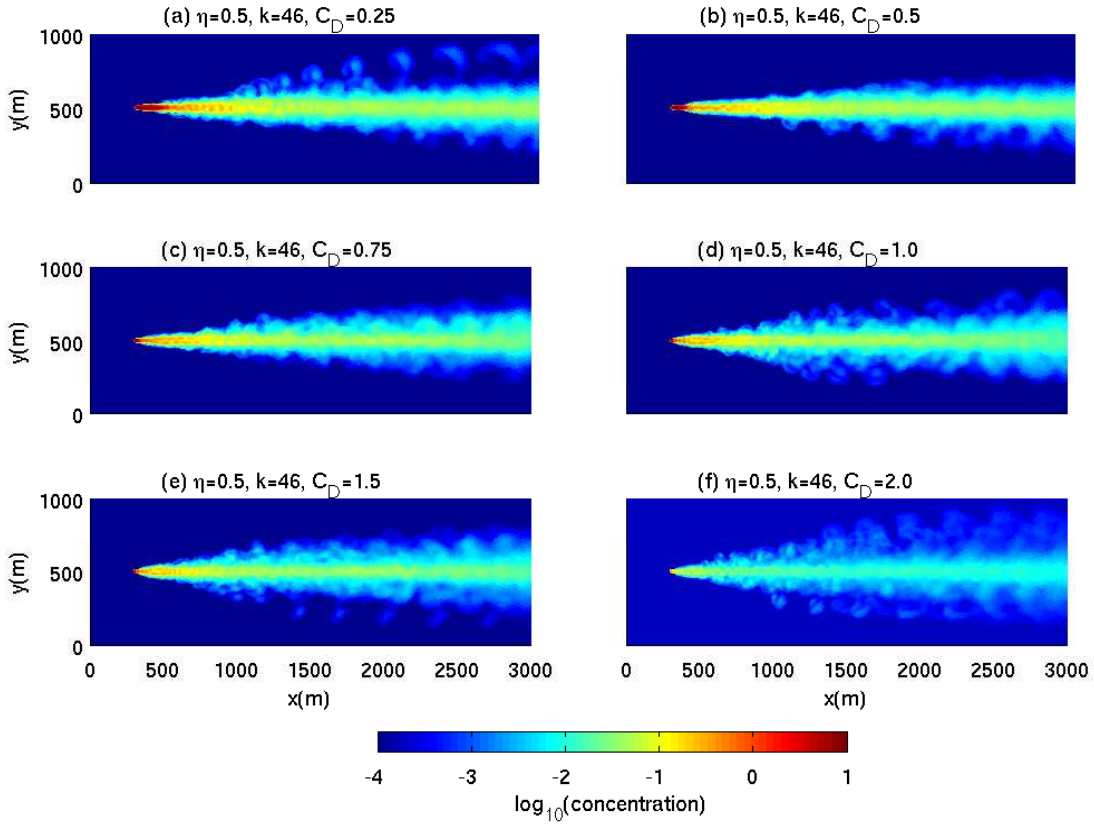

Figure 3.17: Time-averaged non-dimensional concentration field under the combined action of the steady and oscillatory flows ($\eta = 1$, $K = 46$, case 37-43 in Table 6.1) with the drag due to the non-dimensional drag coefficients of (a) $C_D = 0.25$, (b) $C_D = 0.5$, (c) $C_D = 0.75$, (d) $C_D = 1.0$, (e) $C_D = 1.5$ and (f) $C_D = 2.0$.

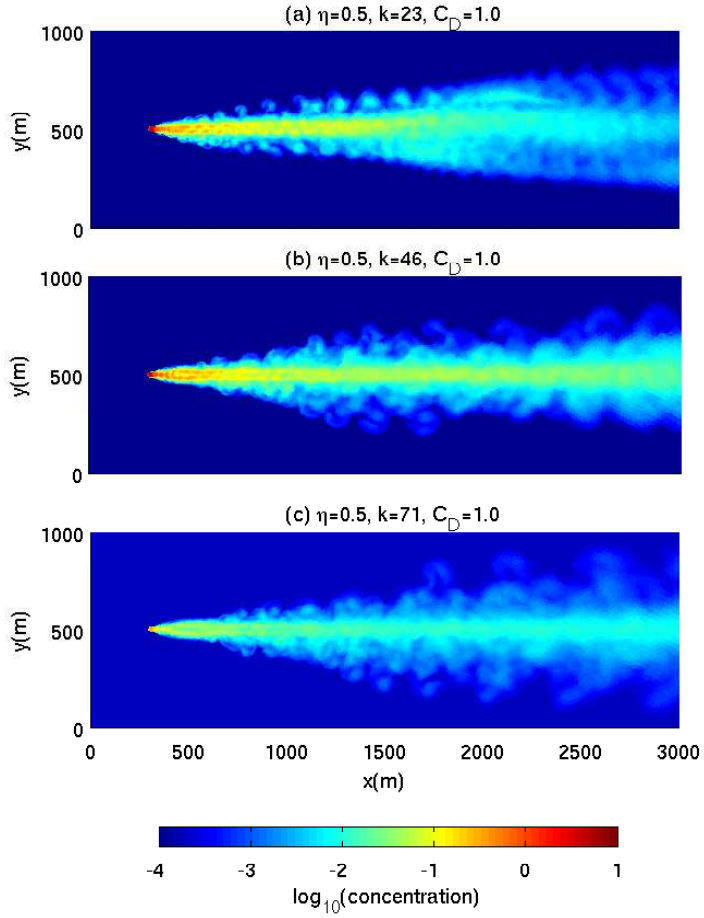

Figure 3.18: Time-averaged non-dimensional concentration field under the combined action of the steady and oscillatory flows with the drag due to the non-dimensional drag coefficients of $C_D = 1.0$ at (a) case 33 ($\eta = 0.5$, $K = 23$), (b) case 40 ($\eta = 0.5$, $K = 46$), and (c) case 47 ($\eta = 0.5$, $K = 71$).

Table 3.4: Time-averaged lateral mixing coefficients for oscillatory flow cases 8-28 with $\eta = 1$ shown in Table 3.1.

Case No.	K	C_D	ε_t^* $(m^2 s^{-1})$	$\varepsilon_t^*/\varepsilon_t$
29	23	0	0.03	1.00
30	23	0.25	0.40	13.33
31	23	0.5	0.52	17.33
32	23	0.75	0.65	21.67
33	23	1.0	0.68	22.67
34	23	1.5	0.68	22.67
35	23	2.0	0.70	23.33
36	46	0	0.03	1.00
37	46	0.25	0.49	16.33
38	46	0.5	0.57	19.00
39	46	0.75	0.66	22.00
40	46	1.0	0.75	25.00
41	46	1.5	0.74	24.67
42	46	2.0	0.82	27.33
43	71	0	0.03	1.00
44	71	0.25	0.36	12.00
45	71	0.5	0.57	19.00
46	71	0.75	0.74	24.67
47	71	1.0	0.76	25.33
48	71	1.5	0.76	25.33
49	71	2.0	0.80	26.67

Table 3.5: Relevant λ values in Equation (3.18) for the lateral mixing coefficients.

Case Name	η	K	λ	remarks
mean flow	0	0	5	λ_0, mean flow
mean + Oscillating	1	23	31	$\lambda_{\eta=1,k=23}$ for $T = 4$ h
Unidirectional + Oscillating	1	46	40	$\lambda_{\eta=1,k=46}$ for $T = 8$ h
Unidirectional + Oscillating	1	71	46	$\lambda_{\eta=1,k=71}$ for M2 tide
Unidirectional + Oscillating	0.5	23	26	$\lambda_{\eta=1/2,k=23}$ for $T = 4$ h
Unidirectional + Oscillating	0.5	46	28	$\lambda_{\eta=1/2,k=23}$ for $T = 8$ h
Unidirectional + Oscillating	0.5	71	29	$\lambda_{\eta=1/2,k=23}$ for M2 tide

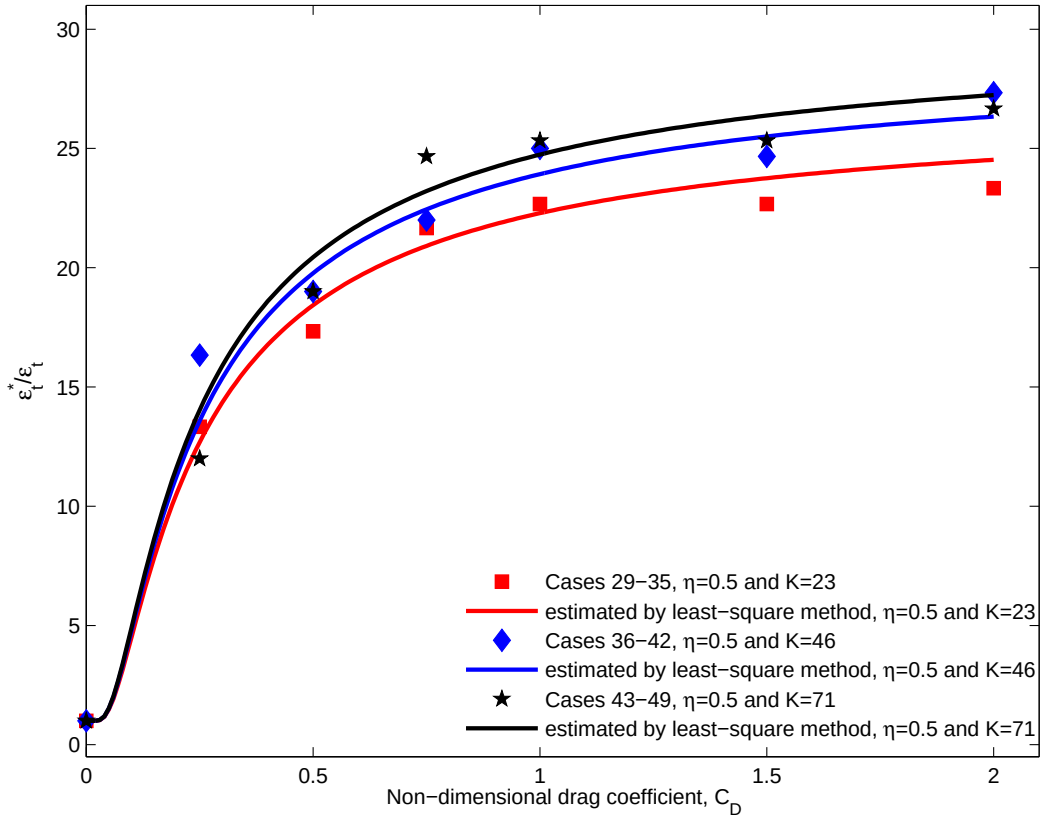

Figure 3.19: Time-averaged lateral mixing coefficients for the combined flow cases ($\eta = 0.5$, cases 29 through 49 in Table 3.1). They are normalized by the empirical transverse mixing $\varepsilon_t \cong 0.15du^*$. The red squares, blue diamonds, and black stars are computed from the numerical simulations and the associated colored lines show the exponential relation given by Equation (3.18) for the relevant values of λ listed in Table 3.5.

3.5 Summary

In this study, we have performed a series of high-resolution, two-dimensional, depth-averaged numerical simulations in an open channel domain to understand the fundamental aspects of mixing and transport of a passive scalar around a porous obstacle. For this in-depth parametric study, three key non-dimensional parameters were introduced, namely: the non-dimensional drag coefficient C_D (a surrogate for the porosity of the obstacle), the shape parameter η, and the tidal excursion length scale to the cylinder diameter K. The broad parametric study has clearly shown how these three non-dimensional parameters affect the dispersion of a passive scalar plume.

For uni-directional flow condition (i.e. $\eta = 0$), the result of the classical dispersion case (case 1 in Table 3.1) from the numerical simulation were a good agreement with the empirical relation (Equation (3.16)) for the lateral mixing. The drag induced by a porous obstacle results in a complex vortex-wake field behind the obstacle. Specially, based on our results, we were able to classify the characteristic of the vortex-wake field into three distinct regions, namely: a separation region, an in-phase vortex region, and a binary vortex street region. Overall, quantitative results for the lateral mixing coefficient as a function of the drag coefficient for different values of K and η were presented. An equation that describes well the lateral mixing across these broad ranges of conditions was found to be of the form

$$\varepsilon_t^*/\varepsilon_t = \lambda \exp\left(-\tfrac{1}{5C_D}\right) + 1,$$

as shown in Equation (3.18). The constant λ varies by close to an order of magnitude depending on the flow conditions (e.g. tidal forcing period and shape factor) as well as the porosity of the obstacle.

The take home message from this study is the finding that mixing and transport of a passive scalar is greatly enhanced in the presence of an obstacle, especially under strong oscillatory forcing conditions. Flow reversals and passive scalar mixing in a pure oscillatory flow are investigated in the next chapter.

Chapter 4

Mixing under flow reversals[1]

4.1 Introduction

Flow reversal is a visible phenomenon in tidally-forced water bodies such as in estuaries and the coastal ocean. Effluent discharged in these tidally forced systems can therefore undergo multiple reversals with older effluent washing over newer effluent at or close to the discharge site. This can quickly lead to high concentration levels and undesirable environmental conditions (Kay 1990). There are a number of studies that have focused on providing a variety of strategies such as the use of holding tanks and timing of contaminant release in such systems in order to alleviate undesirable environmental problems (Purnama and Kay 1999; Smith 1985).

In this context, the most relevant parameter is the ratio of the tidal flow to mean freshwater flow $\eta = U_T/U_m$ that was denoted as the shape parameter in Chapter 3. This shape parameter η can vary by orders of magnitudes for different estuaries with values ranging from much less than 1 in highly stratified (salt-wedge like) estuaries such as the Mouth of the Mississippi River and the Hudson River Estuary, to as high

[1]This chapter is submitted in substantial part as a manuscript entitled "Scalar dispersion around a cylindrical obstacle in oscillatory flows", by H. Ku and S. K. Venayagamoorthy, to *International Symposium on Shallow flows* Conference on June 4-6, 2012.

as 100 in vertically homogeneous (e.g. the Delaware Bay) or partially mixed estuaries (e.g. the San Francisco Bay and Puget Sound Estuary). The mixing and transport of a passive scalar in tidally-dominated systems ($\eta \gg 1$) is much more complex than in systems that restrict flow reversals ($\eta < 1$). The flow reversals as already mentioned make this problem physically interesting with the build-up of high concentrations. The flow reversals also make this problem both mathematically interesting and challenging (Kay 1990). When advection is small (or zero), the longitudinal diffusion can not be ignored as is commonly assumed for advection-diffusion problems in water bodies. The inclusion of longitudinal diffusion makes it very difficult to obtain tractable analytical solutions to the time-dependent advection-diffusion equation (Kay 1990, Smith 1982). There have been some previous work based on time-varying advection model that includes the effects of tidal oscillation (Harleman *et al.* 1968; Bella and Dobbins 1968).

Smith (1982) showed that the use of the classical advection-diffusion model results in a negative diffusivity. This implies the spontaneous development of infinite concentration in reversing flow for the case when the lateral mixing timescale is larger than the forcing period. Based on such analytical studies, a number of studies have focused on minimization and optimization strategies for concentration of effluents discharged into oscillating flow systems (Webb and Tomlinson 1992; Giles 1995; Smith and Purnama 1999; Smith 2000). This problem quickly becomes analytically intractable once an obstacle is introduced into the flow field. This is where computational fluid dynamics has become increasingly handy in providing numerical solutions. In this study, our objective is to gain insight into the effect of an obstacle in a pure oscillating flow field ($\eta = \infty$) on passive scalar mixing via highly resolved numerical simulations using the SUNTANS research code (which has been extensively discussed in Chapters 2 and 3).

In what follows in this chapter, we first present the model set-up and some statistical parameters that will be used to quantitatively describe the scalar field in Section 4.3. The results of passive scalar mixing obtained from numerical simulations are then discussed in Section 4.3. A short summary is provided in Section 4.4.

4.2 Problem set-up

We use an open channel domain that is 3 km long and 1.5 km wide for the computational simulations. A 20 m cylindrical porous obstacle is located at the middle of the domain at x=1.5 km and y=0.5 km as shown in Figure 4.1. The drag formulation discussed in Section 3.3.2 in Chapter 3 is used to account for the drag exerted by the obstacle. Two simulation are performed, one without an obstacle and one with an obstacle with a drag coefficient C_D=1.

The unstructured computational mesh consists of approximately 351000 cells with grid refinement near the cylindrical obstacle. The minimum voronoi distance of about 0.04 m is used to satisfy the stability criterion with a maximum Courant number of $C_r = 0.5$. A pure tidal flow is enforced at the left-end boundary of the domain as follows

$$u = U_T \sin(\omega t), \tag{4.1}$$

where U_T is the amplitude of the oscillating velocity; and ω is the tidal frequency. Boundary conditions for the horizontal velocity u are free-slip at the lateral walls. The horizontal component in the y-direction of the velocity field v has no-flux boundary conditions on the lateral walls, and the scalar field has gradient-free boundary condition on all walls. The tidal period is $T = 8$ hours with a corresponding forcing frequency $\omega = 2.18 \times 10^{-2}$ rad s^{-1}.

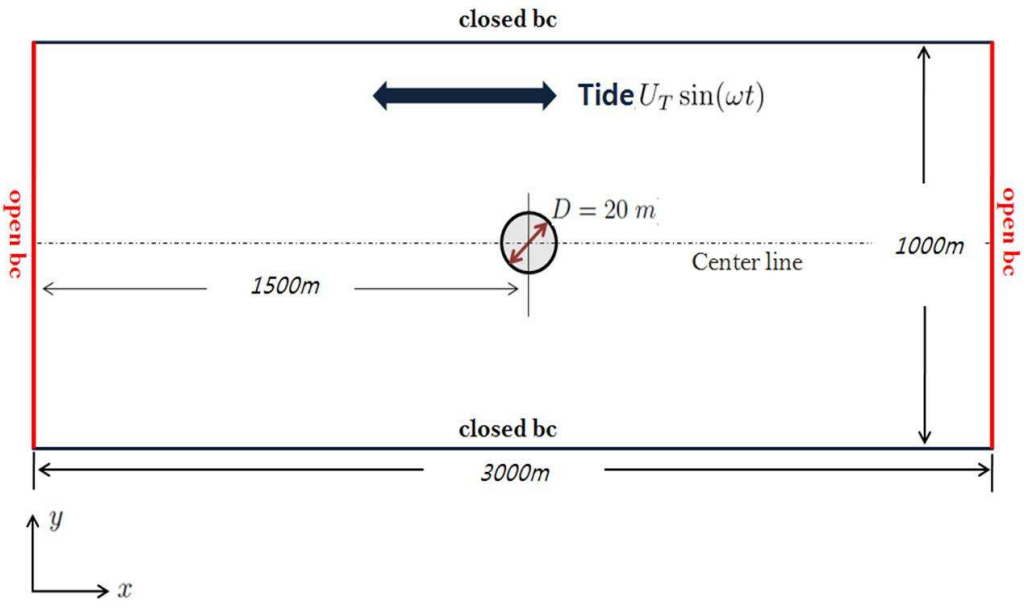

Figure 4.1: Computational domain for all simulations. It is 3000 m long and 1000 m in wide. A porous cylindrical obstacle is located at $x = 1500$ m and $y = 500$ m and it is 20 m of the diameter. The tidally driven velocity field is imposed at the left-end boundary of the domain.

4.2.1 Statistical parameters

Statistical parameters such as moments of concentration distributions can provide useful quantitative information on plume characteristics. In Section 4.3, we use the mean, standard deviation, skewness, and kurtosis to analyze both the instantaneous and time-averaged passive scalar fields.

Considering the values of the plume concentration as a random variable set $X = \{\bar{C}_1,\ \bar{C}_2\ \cdots,\ \bar{C}_N\}$ with probability $p_1,\ p_2,\ \cdots,\ p_n$, the k^{th} central moments are defined as

$$m_k = E\left\{(X - E[X])^k\right\}, \tag{4.2}$$

where the expectation operator E is the weighted average of all possible values given

by

$$E[X] = \frac{\sum_{i=1}^{N} \bar{C}_i p_i}{\sum_{i=1}^{N} p_i}. \tag{4.3}$$

The second moment is known as the variance. The standard deviation given by the square-root of the variance provides a measure of the spread of the concentration plume. It is given by

$$\sigma = \sqrt{m_2} = \sqrt{E\left\{(X - E[X])^2\right\}}. \tag{4.4}$$

The skewness and the kurtosis are given by the third and fourth moments

$$\gamma = \frac{m_3}{\sqrt{m_2^3}} = \frac{m_3}{\sigma^3} = \frac{E\left\{(X - E[X])^3\right\}}{\left(E\left\{(X - E[X])^2\right\}\right)^{3/2}}, \tag{4.5}$$

$$\beta = \frac{m_4}{m_2^2} = \frac{m_4}{\sigma^4} = \frac{E\left\{(X - E[X])^4\right\}}{\left(E\left\{(X - E[X])^2\right\}\right)^2}. \tag{4.6}$$

The skewness is a measure of the asymmetry of the plume distribution while the kurtosis provides a measure of the peakedness (measure of intermittency) of the concentration distribution (noting that the kurtosis of the Gaussian distribution is equal to 3).

4.3 Results

The passive scalar field from the simulation without drag is presented first to show the effect of flow reversal on the mixing. This is followed by results from the simulation with an obstacle to show the combined effect of flow reversals and drag.

4.3.1 Effect of the flow reversal

Figure 4.2 shows the passive scalar field as a time sequence over a duration of three tidal periods (with $T = 8$ h).The scalar is advected to the right during the forward phase of the tide (see Figure 4.2(a)) and as the tide reverses, the scalar is advected back in the opposite direction (see Figure 4.2(b)). This pattern repeats itself in subsequent tidal periods as shown in Figure 4.2(c)-(f).

A time sequence of the longitudinal concentration profile along the centerline (y=500 m) is shown in Figure 4.3 for three tidal cycles. The profiles are normalized by the maximum concentration value at $t = 3$ T. As shown in Figures 4.2 and 4.3, the plume is concentrated downstream of the point source during the first half cycle while it is upstream during the second half cycle. The time sequence of the longitudinal profiles shows bi-peaks: one at the point source and the other at either the downstream or upstream ends. These results are consistent with the study of Kay (1997) where he showed that the time-varying flow field causes the formation of a peak at each end of the flow reversal. The slightly higher peak at the location of the point source (x=1.5 km) results from the continuous discharge of the scalar at this location.

The time-averaged scalar field and corresponding longitudinal profile along the centerline are shown in Figures 4.4 and 4.5, respectively. The time-averaged longitudinal concentration profile is normalized by the maximum concentration. Figure 4.4 shows a number of distinct locations with significantly higher concentrations. This is much more evident in the longitudinal profile (Figure 4.5) where multiple peaks that are symmetric about the source location (x=1500 m) are seen. This is consistent with the notion that spontaneous spikes of infinite concentrations can develop when flow reversals occur, which implies that negative diffusivities are required to predict such peaks in the conventional advection-diffusion equation (Smith 1981, 1982). Notice also how the plume width in Figure 4.4 gets narrower upstream and downstream of

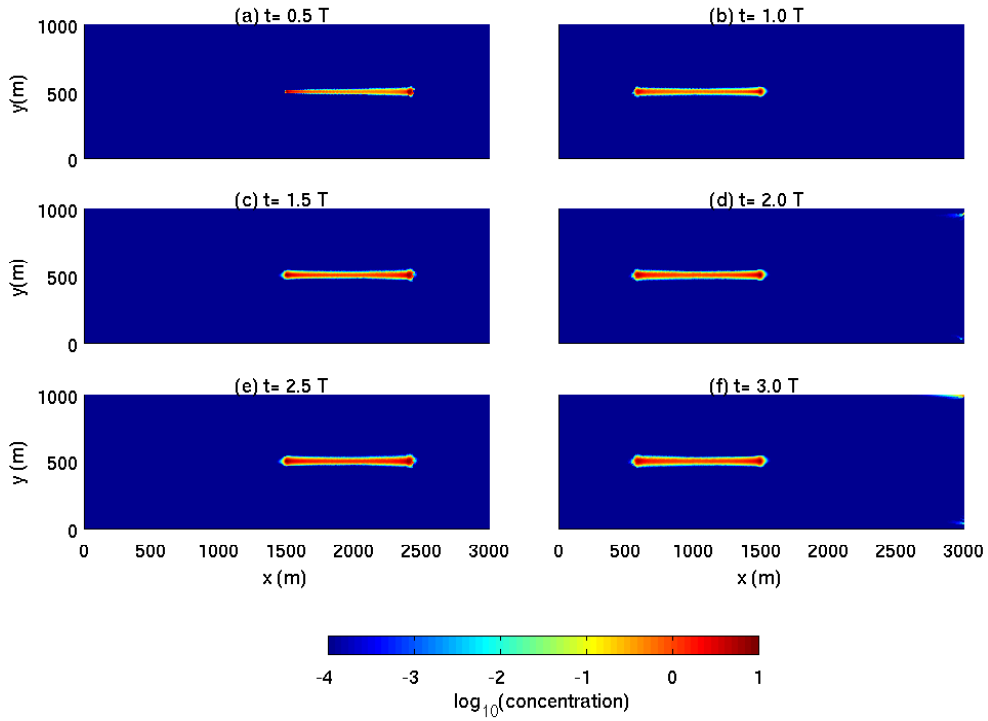

Figure 4.2: Instantaneous scalar concentration fields in the absence of an obstacle in a pure oscillatory flow (i.e. $u = U_T \sin(\omega t)$ and $C_D = 0$) at (a) $t = 0.5$ T, (b) $t = 1.0$ T, (c) $t = 1.5$ T, (d) $t = 2.0$ T, (e) $t = 2.5$ T, and (f) $t = 3.0$ T. The passive scalar point source is located at the center of the domain with a radius of 10 m.

the multi-peaks at x= 550, 1050, 1500, 1950 and 2450 m, respectively.

Figure 4.6 shows the time-averaged lateral concentration distributions at x=1050, 1500, and 1950 m (i.e. the location of multi-peaks) with the classical Gaussian distribution profile superimposed. The statistical values obtained from cross-sectional profiles at time $t = 1.75$ T is listed in Table 4.1 while the time-averaged statistics are given in Table 4.2. The kurtosis values shown in Table 4.1 are all very close to 3, indicating that the passive scalar follows a Gaussian distribution in the lateral direction at any given cross section. However, the time-averaged statistics do show significant departure from the Gaussian profile indicating that the longitudinal dispersion is not Gaussian. This is clearly expected due to the multiple peaks that occur as a consequence of flow reversals. These results confirm what is already well established in the

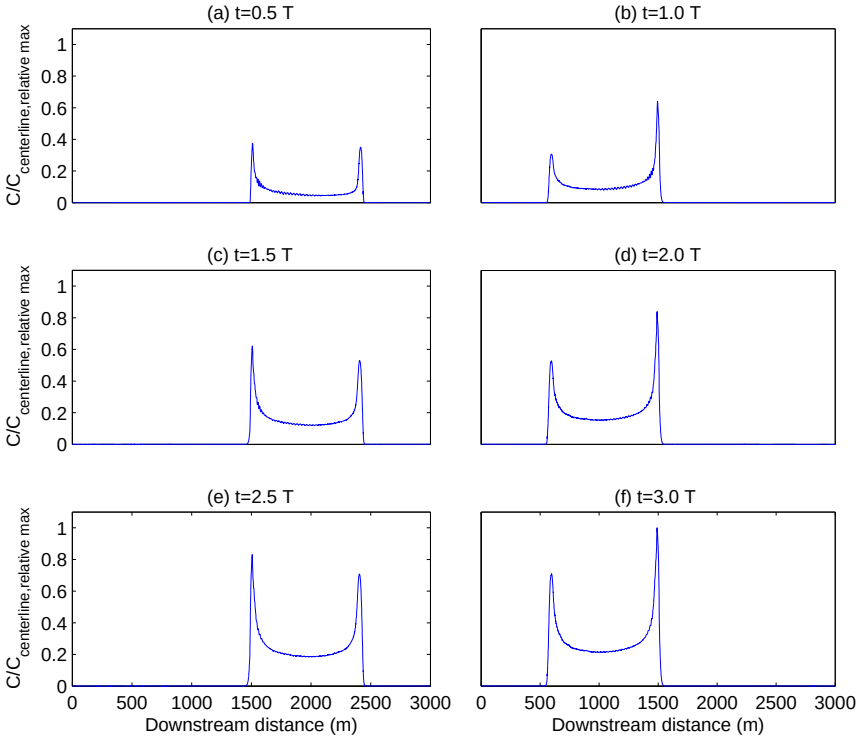

Figure 4.3: Time sequence of instantaneous longitudinal concentration profiles in the absence of the obstacle in a pure oscillatory flow (i.e. $u = U_T \sin(\omega t)$ and $C_D = 0$) at (a) $t = 0.5$ T, (b) $t = 1.0$ T, (c) $t = 1.5$ T, (d) $t = 2.0$ T, (e) $t = 2.5$ T, and (f) $t = 3.0$ T. These longitudinal profiles are measured along the centerline ($y = 500$ m) and relatively normalized by the maxi-maximum concentration (i.e. obtained at $t = 3.0$ T).

sense that the pattern of the dispersal under such pure tidal forcing conditions will cause higher concentration to occur at considerable distances from the source.

Table 4.1: Statistics of the scalar field at time $t = 1.75$ T at three different cross sections: $x = 1050$, 1500, and 1950 m (i.e. at the multi-peaks).

	Location of Cross-section (m)	Standard deviation σ ($\times 10^{-5}$)	Skewness γ	Kurtosis β	Mean C ($\times 10^{-5}$)	Peak value ($\times 10^{-5}$)
at	1050	17.3	-0.93	2.64	1.58	60.99
time	1500	3.26	-1.08	2.85	0.28	11.74
$t = 1.75$ T	1950	9.12	-1.17	3.32	1.41	35.38

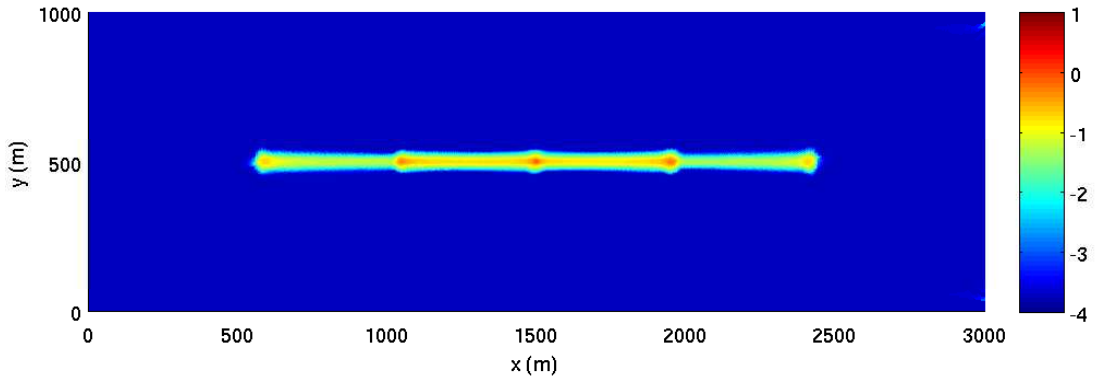

Figure 4.4: Time-averaged scalar concentration field without an obstacle in a pure oscillatory flow the flow ($u = U_T \sin(\omega t)$ and $C_D = 0$). The field is averaged over a duration of three tidal periods.

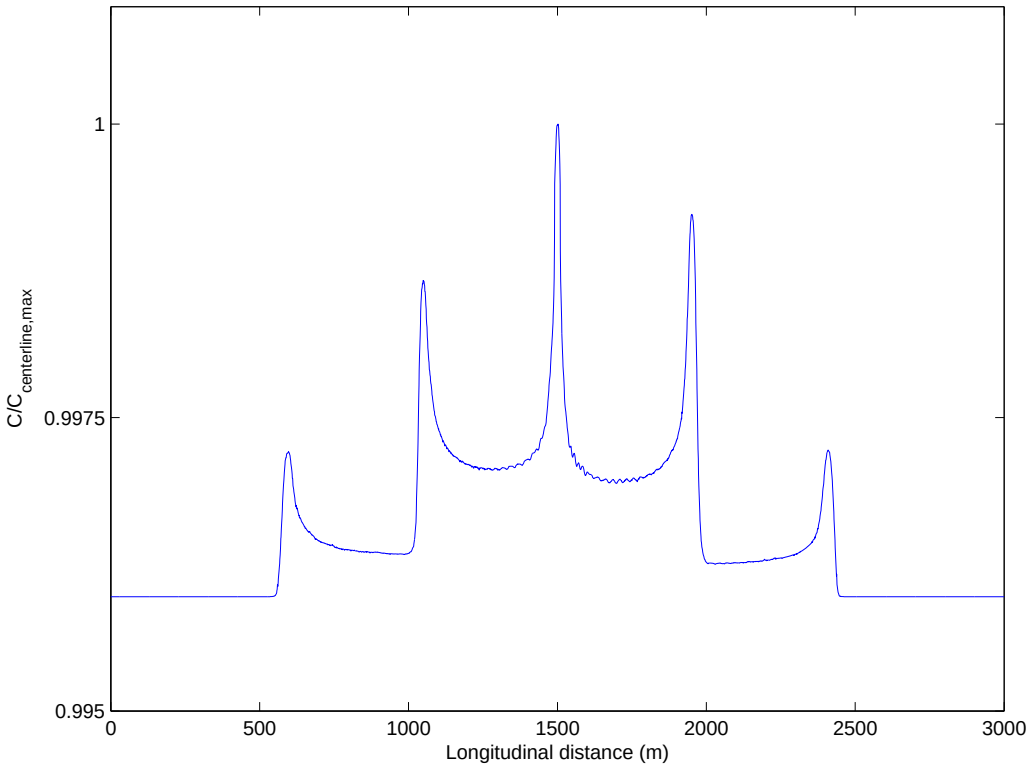

Figure 4.5: Time-averaged longitudinal profiles without an obstacle under the flow reversal ($u = U_T \sin(\omega t)$ and $C_D = 0$). Multi-peaks occur symmetrically.

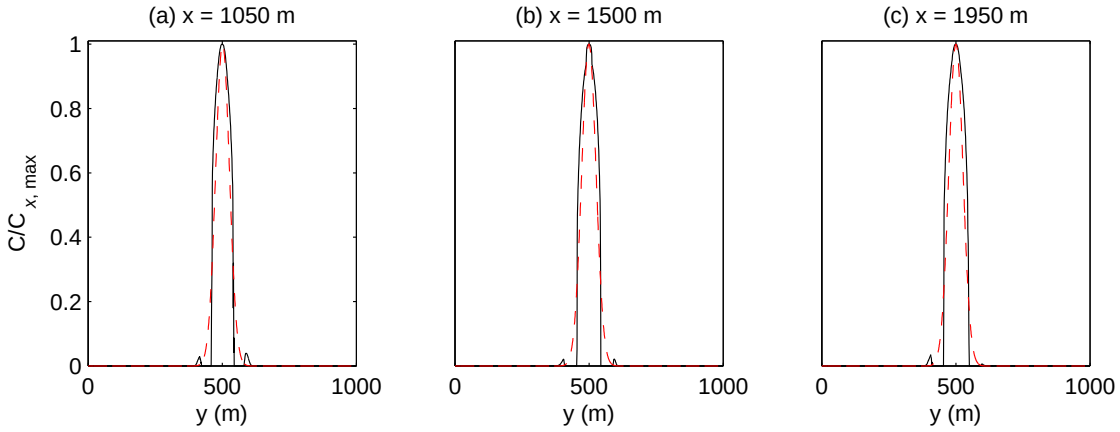

Figure 4.6: Time-averaged lateral concentration profiles at (a) $x = 1050$ m, (b) $x = 1500$ m, and (c) $x = 1950$ m. The Gaussian distribution is also shown by the red-dashed line.

Table 4.2: Time-averaged statistics of the scalar field depicted in Figure 4.6. The location of the cross-sections are at the multi-peaks, $x = 1050$, 1500, and 1950 m, and the centerline is at $y = 500$ m.

	Location of Cross-section (m)	Standard deviation σ ($\times 10^{-5}$)	Skewness γ	Kurtosis β	Mean $\overline{C}$ ($\times 10^{-5}$)	Peak value ($\times 10^{-5}$)
time	1050	5.91	-0.88	2.54	0.59	20.82
-	1500	9.99	-0.84	2.06	0.82	31.01
	1950	7.28	-0.81	2.36	0.77	25.16
	Centerline (m)					
averaged	$y = 500$ m	6.57	1.38	4.64	4.42	31.10

4.3.2 Scalar mixing under flow reversals with flow blockage

Here, we present results of passive scalar mixing in the presence of an obstacle in a pure oscillatory flow. All other flow conditions are identical to the case without an obstacle that was discussed in the previous section.

Figure 4.7 shows a time sequence of the instantaneous scalar field in the presence of an obstacle with C_D=1, over two tidal periods. The presence of the almost impervious obstacle causes significant flow blockage that causes the formation of a downstream wake. Soon after the initial vortex shedding begins, the flow starts to retard as the tidal velocity reverses direction and increases in amplitude. This causes the plume to contract in the longitudinal direction with a simultaneous dispersion in the lateral direction. As the flow reverses, the vortex formation is also halted due to the flow momentarily attaining a stationary state (see Figure 4.7(b), (d), (f), and (h)). Notice also that for this special case with $\eta = \infty$, the vortex wake created during each half cycle will sweep past the obstacle during each subsequent half cycle. It is clearly evident that the combined action of the flow reversals (oscillations) and obstacle-induced drag results in significantly enhanced dispersion in the lateral direction compared to the flow reversal case without the obstacle (Section 4.3.1) as well as the cases discussed in Chapter 3 where flow reversals were not considered. We note that as the extent of the plume reaches the lateral boundaries, the no-flux boundary condition used at these boundaries results in the non-physical longitudinal spreading that is observed as shown in Figure 4.8(g) and (h). In order to see a longer time sequence, a wider computational is required.

The time-averaged scalar concentration field is shown in Figure 4.8. Time-averaged lateral (cross-sectional) concentration profiles at x=1000, 1300, 1700, and 2000 m and spanwise concentration profiles at y=250, 500, and 750 m, are shown in Figures 4.9 and 4.10, respectively. The time-averaged field shows clearly the enhanced mixing due the combined effect of flow reversals and obstacle-induced drag. Comparing this

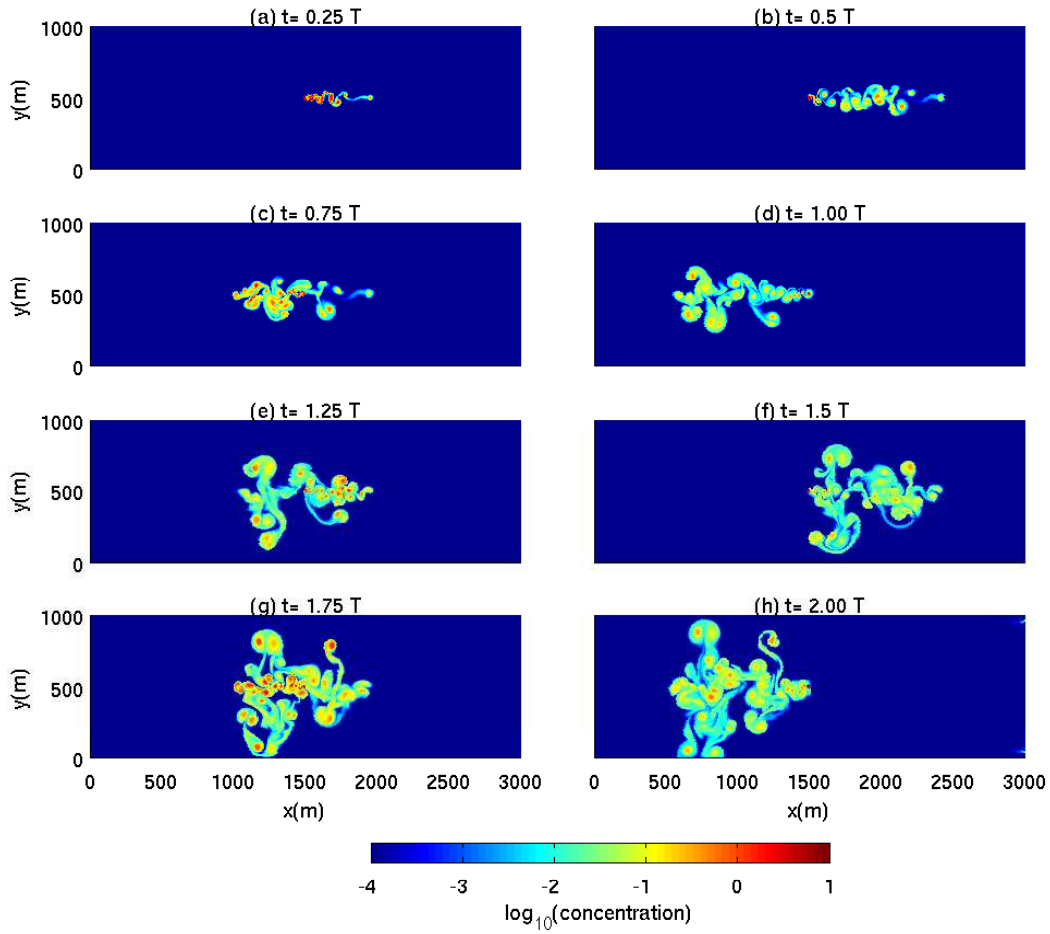

Figure 4.7: The instantaneous scalar concentration fields in the presence of the obstacle in a pure oscillatory flow field (i.e. $\eta = \infty$ and $C_D = 1.0$) are shown at (a) $t = 0.25$ T, (b) $t = 0.5$ T, (c) $t = 0.75$ T, (d) $t = 1.0$ T, (e) $t = 1.25$ T, (f) $t = 1.5$ T, (g) $t = 1.75$ T, and (h) $t = 2.0$ T. The passive scalar point source is located within the perimeter of the obstacle.

with Figure 4.4, shows how the drag exerted by the obstacle completely changes the plume behavior. The slight asymmetry is caused by the short number of tidal cycles used for averaging. This asymmetry is also evident in the longitudinal profiles shown in Figure 4.10(a) and (c).

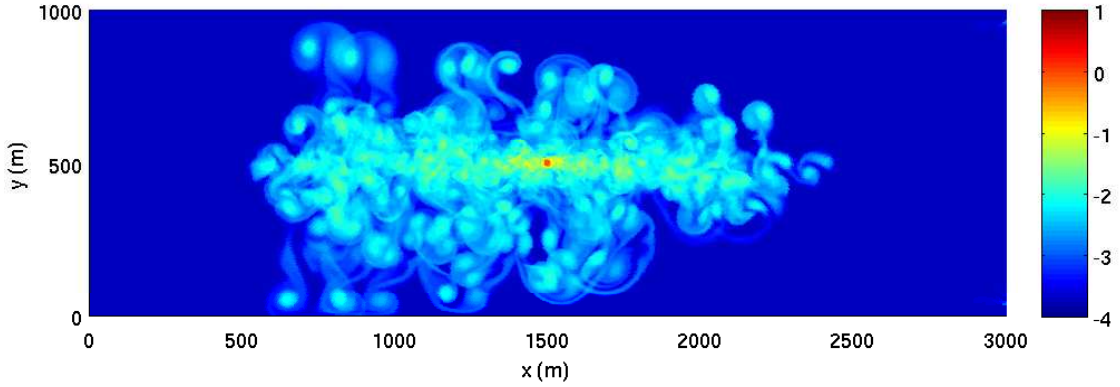

Figure 4.8: Time-averaged scalar field in the presence of an obstacle under the flow reversal ($\eta = \infty$ and $C_D = 1.0$).

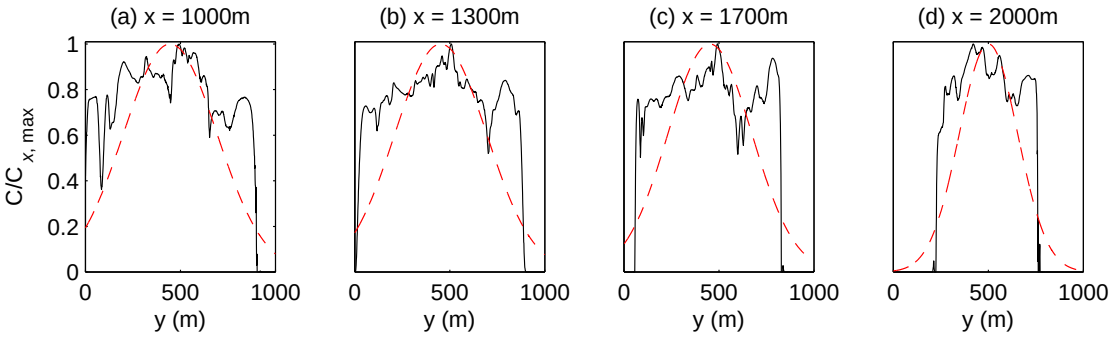

Figure 4.9: Time-averaged lateral concentration profiles at (a) $x = 1000$ m, (b) $x = 1300$ m, (c) $x = 1700$ m, and (d) $x = 2000$ m. The Gaussian distribution is also shown by the red-dashed line.

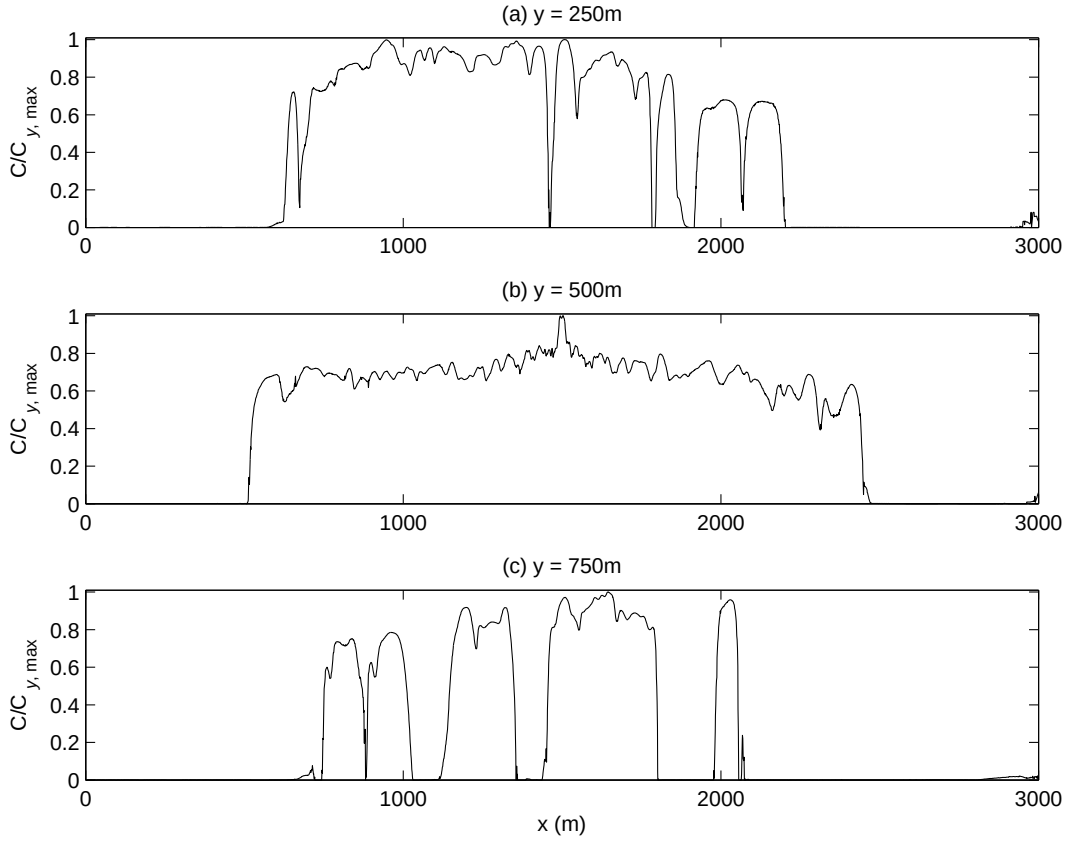

Figure 4.10: Time-averaged longitudinal concentration profiles at (a) $y = 250$ m, (b) $y = 500$ m, and (c) $y = 750$ m. These profiles are normalized by the maximum concentration value at the given location.

The statistics of the distributions shown in Figures 4.7 (g) (at $t = 1.75$ T), 4.9 and 4.10 are given Tables 4.3, 4.4 and 4.5, respectively. The mean and peak values of the concentration are also listed in these tables. On the whole, the statistics show how the entire plume field deviates from the Gaussian distribution as well as the significant enhancement in the mixing compared to the simulation without the drag.

Table 4.3: Statistics of the concentrations for the flow field at time $t = 1.75$ T.

	Location of Cross-section (m)	Standard deviation σ ($\times 10^{-5}$)	Skewness γ	Kurtosis β	Mean C ($\times 10^{-5}$)	Peak value ($\times 10^{-5}$)
at	1000	0.04	4.02	-28.2	4.3×10^{-3}	0.25
time	1300	2.19	1.30	3.29	0.63	7.34
$t = 1.75$ T	1700	3.18	0.29	1.37	0.67	8.74
	2000	8.8×10^{-5}	-0.83	2.20	7.6×10^{-6}	3.5×10^{-4}

Table 4.4: Statistics of the concentrations profiles depicted in Figure 4.9.

	Location of Cross-section (m)	Standard deviation σ($\times 10^{-5}$)	Skewness γ	Kurtosis β	Mean $\overline{C}$ ($\times 10^{-5}$)	Peak value ($\times 10^{-5}$)
time	1000	0.13	0.39	2.15	0.10	0.49
-	1300	0.35	1.19	3.24	0.14	1.24
averaged	1700	0.33	1.04	2.99	0.13	1.21
	2000	0.24	0.09	1.65	0.12	0.86

Table 4.5: Statistics of the concentrations profiles depicted in Figure 4.10.

	Location of Cross-section (m)	Standard deviation σ($\times 10^{-5}$)	Skewness γ	Kurtosis β	Mean $\overline{C}$ ($\times 10^{-5}$)	Peak value ($\times 10^{-5}$)
time	250	0.10	0.14	2.10	0.05	0.37
-	500	18.4	0.64	1.57	0.70	46.12
averaged	750	0.10	0.25	1.99	0.03	0.37

4.4 Concluding remarks

This chapter presents results from high resolution, two-dimensional, depth-averaged numerical simulations of the mixing and transport of passive scalars in purely tidally-driven flow. We have performed two simulations with and without a cylindrical obstacle.

The main conclusion of this study is the finding that flow reversals can result in multiple peaks in concentration at different locations in the flow domain. Furthermore, the presence of the obstacle leads to a highly complex dispersion pattern with significantly enhanced lateral mixing. The implications are that focusing on a single location (i.e. at the outfall) for regulatory purposes might not be sufficient since the scalar concentration peaks can occur far downstream (or upstream) of the source to affect sensitive locations remote from the source location. The next chapter focuses on understanding the vortex-wake interaction resulting from flow through multiple obstacles.

Chapter 5

Mixing around multiple obstacles

5.1 Introduction

There are many environmental flow problems where the flow encounters a group of obstacles such as natural vegetation in water bodies, aquaculture pens, bridge piers, wind turbines and buildings. The flow field becomes very complex due to vortex-wake interactions that can occur in such settings (see e.g. the complex wake fields generated in an offshore wind farm as shown in Figure 1.1(c)). An overarching question concerning flow around multiple obstacles is how the vorticity field (and related vortical flow signature) is modified both in the vicinity of and far downstream of these obstacles due to individual vortex-wake interactions.

Recent studies have focused on understanding the different vortex patterns around multiple obstacles. Zhang and Zhou (2001) showed that the flow patterns around three side-by-side cylinders is greatly influenced by both the lateral and longitudinal spacing between the cylinders. They found that a normalized (based on the cylinder diameter) lateral spacing of 5 is at least required to keep the wake regions independent, while two independent wakes are observed at a normalized spacing of 4 in the longitudinal direction. Other studies have used both staggered and unstaggered array

of cylinders to study flow around multiple obstacles (Moulinec *et al.* 2004; Nicolle and Eames 2011).

While the previous two chapters (Chapters 3 and 4) focused on understanding the flow around a single obstacle, our focus here is on flow around multiple obstacles. We use the SUNTANS research code (discussed earlier) to perform a series of highly-resolved two-dimensional, depth-averaged numerical simulations. In what follows, we present the problem configurations and simulation cases in slightly more detail in Section 5.2. This is followed by results and discussion in Section 5.3 and a brief summary in Section 5.4.

5.2 Problem configuration and diagnostics

In this study, we consider two different configurations: first a single column of three cylinders is used to study the effect of longitudinal spacing (L_G) between the cylinders on the both the flow and scalar fields; second, we use a staggered array of cylinders consisting of a total of eight cylinders to study the clustering effect in terms of both lateral and longitudinal spacing and associated passive scalar mixing. Two important length parameters are introduced to describe the configurations: (1) the ratio of the longitudinal center-to-center spacing between adjacent obstacle to the cylinder diameter, L_G/D, and (2) the ratio of the lateral center-to-center spacing to the cylinder diameter L_T/D.

5.2.1 Array of cylinders

For all simulations, we use an open channel flow computational domain as shown in Figure 5.1. Some studies have shown that significant side wall interactions interfere with the vortex shedding patterns for channel widths shorter than $15D$ (Jackson 1987; Ding and Kawahara 1999; Kumar and Mittal 2006). Hence, we use a computational

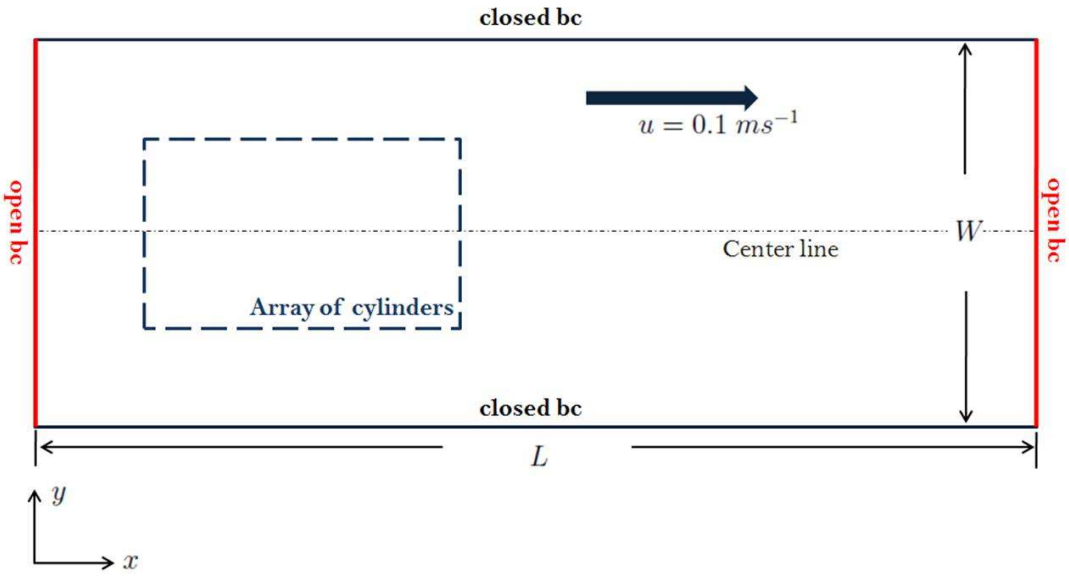

Figure 5.1: Schematic of computational domain.

domain that $20D$ (400 m) wide for the single column cases to minimize the interference from the side walls. The width is given by $W = T + 20 \times D$ (i.e from 400 m to 800 m) for the staggered array cases depending on the lateral spacing L_T (see Figure 5.2 for details).

For all simulations, a mean velocity field is forced at the left-boundary of the open channel domain given by

$$u = U_m, \tag{5.1}$$

where U_m= 0.1 m s^{-1} is the amplitude of the mean uni-directional current. Boundary conditions for the horizontal velocity u are free-slip at the lateral walls. The horizontal component in the y-direction of the velocity field v has no-flux boundary conditions on the lateral walls, and the scalar field has gradient-free boundary condition on all walls. Grid refinement is used in the vicinity of the obstacles. Each cylinder for both configurations has a continuous scalar point source within its perimeter.

5.2.2 Simulation cases

A total of 8 simulations as listed in Table 5.1 were conducted to study the different vortex patterns around the obstacles in both configurations shown in Figure 5.2 in a uni-directional steady flow field. The first two cases (cases 1-2) are for the single column configuration with two different longitudinal spacing of L_G/D=2 and 10. The remaining six cases (cases 3-8) have eight cylinders configured in a staggered array and are used to show the combined effect of different lateral and longitudinal spacing (L_G/D=2 and 4 with L_T/D=2, 4 and 10).

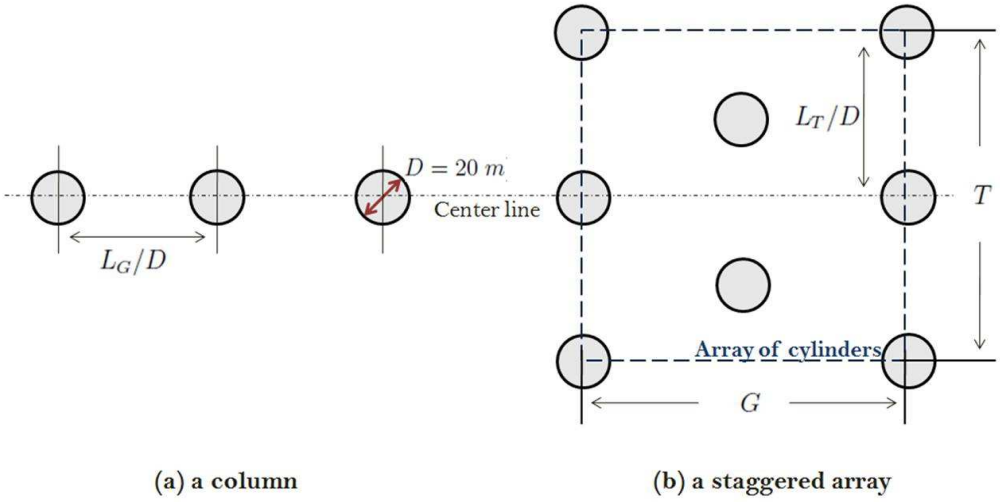

Figure 5.2: Layout of cylinders for (a) a single column configuration and (b) a staggered array. The single column has three cylinders while the staggered array consists of the eight cylinders.

5.3 Results and discussion

In this section, simulation results of the scalar fields are presented.

Table 5.1: Summary of simulations presented in this chapter.

Case #	Array of cylinders	L_G/D	L_T/D	G [m]	T [m]	W [m]
1	column	2		20		400
2	column	10		200		400
3	staggered array	2	2	80	80	480
4	staggered array	2	4	80	160	560
5	staggered array	2	10	80	400	800
6	staggered array	10	2	400	80	480
7	staggered array	10	4	400	160	560
8	staggered array	10	10	400	40	800

5.3.1 Single column cases

Figures 5.3 and 5.5 show time sequences of the passive scalar fields for a duration of 10800 seconds for cases 1 and 2 with center-to-center longitudinal spacing of 40 m and 200 m, respectively. The corresponding time-averaged distributions are shown in Figures 5.4 and 5.6. The discussion below refers to all of these figures, with a particular emphasis on the interaction of vortex shedding in near-field (i.e. close to the cylinders).

For case 1 with $L_G/D = 2$, the cylinders are closely clustered together. The vortices are shed from both sides of the top and bottom of the last cylinder while the close proximity of adjacent cylinders behind the first and second cylinders suppresses the shedding and formation distinct downstream wakes. However, flow separation at the first two cylinders results a slightly enhanced lateral dispersion close to these cylinders. Essentially, the three cylindrical obstacles collocated close together in a column have the same effect of a single elliptical obstacle with a major axis length of $5D$ and a minor axis length of D, respectively. The turbulent vortices arising from these obstacles roll up into a non-staggered row merging further downstream as shown in Figure 5.3 (e) and (f). Notice also how the binary vortex region consisting of a staggered rows of vortices does not form in contrast to the single obstacle cases discussed in Chapter 3. The time-averaged scalar field shows the combined effect of

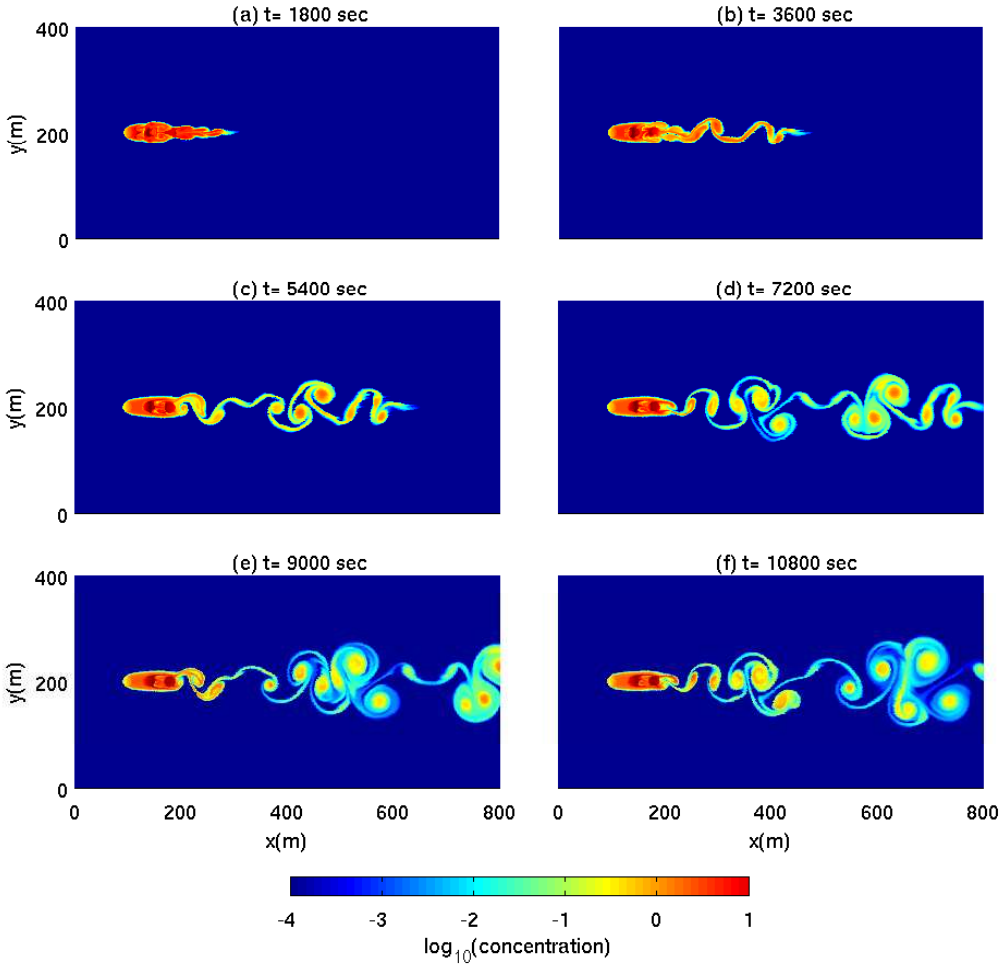

Figure 5.3: Time sequence using the plume concentration of passive scalar around the cylinders collocated in a single column array with $L_G/D = 2$ (case 1 in Table 5.1) at time (a) $t = 1800$ sec, (b) $t = 3600$ sec, (c) $t = 5400$ sec, (d) $t = 7200$ sec, (e) $t = 9000$ sec, and (f) $t = 10800$ sec, respectively.

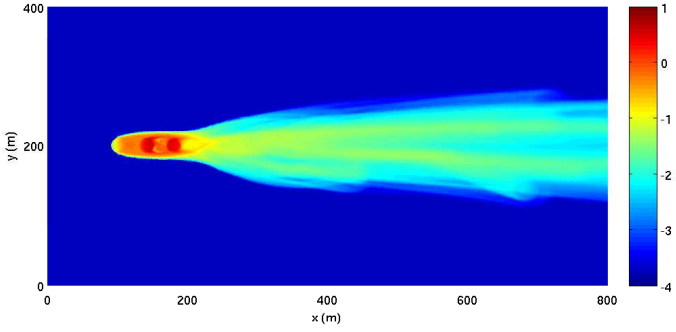

Figure 5.4: Time-averaged passive scalar field for case 1.

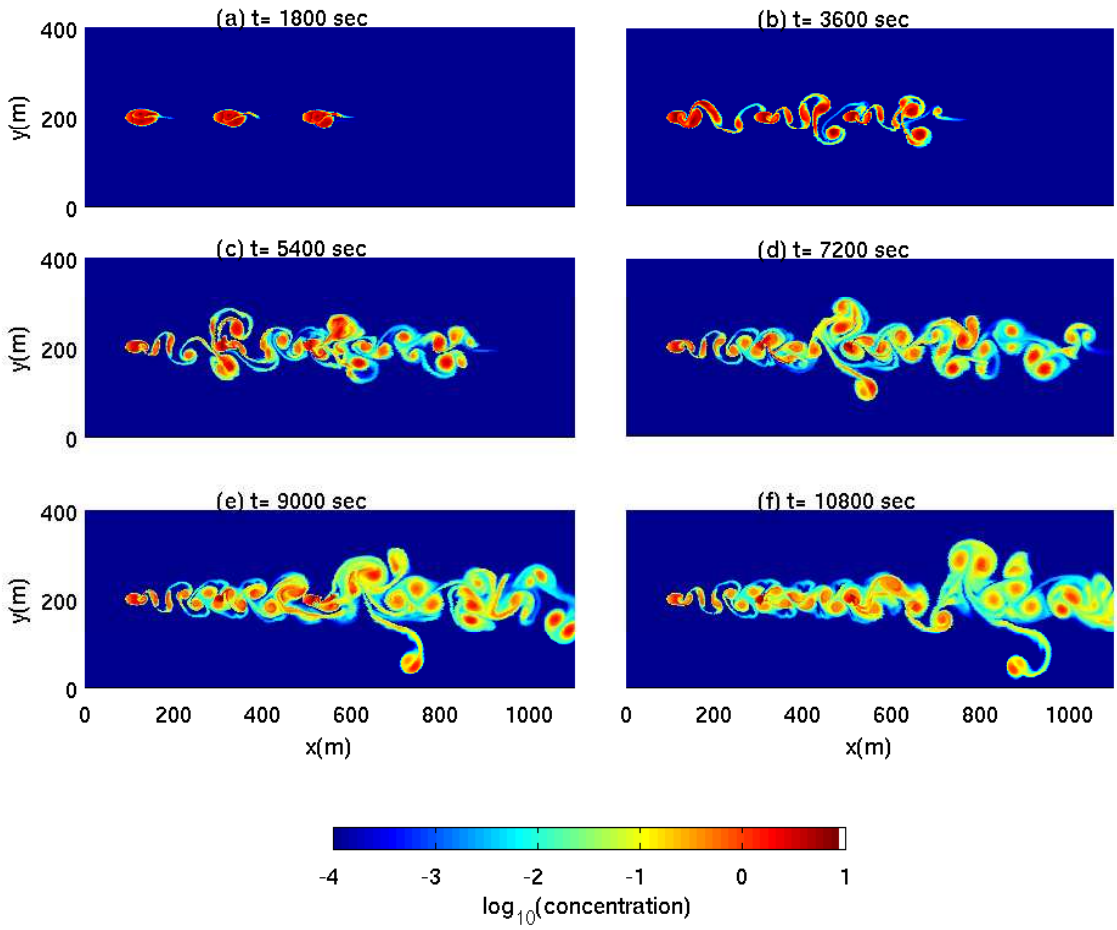

Figure 5.5: Time sequence using the plume concentration of passive scalar around the cylinders collocated in a single column array with $L_G/D = 10$ (case 2 in Table 5.1) at time (a) $t = 1800$ sec, (b) $t = 3600$ sec, (c) $t = 5400$ sec, (d) $t = 7200$ sec, (e) $t = 9000$ sec, and (f) $t = 10800$ sec, respectively.

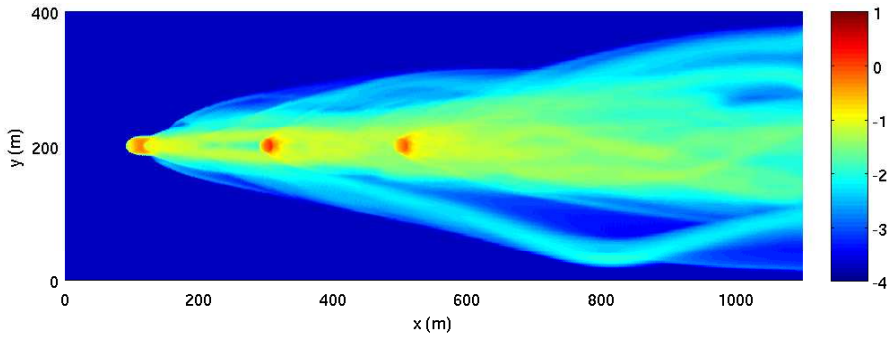

Figure 5.6: Time-averaged passive scalar field for case 2.

the vortex shedding from the closely spaced obstacles on the overall lateral mixing which is significantly enhanced.

On the other hand, for case 2 with $L_G/D = 10$, the vortex shedding and the formation of the downstream wakes occur behind each of the cylinders. However, notice how the wake-vortex field behind the first cylinder influences the flow behind the second cylinder resulting in the shedding of amplified vortices behind the second and subsequently third cylinders as shown in Figure 5.5 (b), (c) and (d). Clearly, the increased spacing between the obstacles results in a much more dramatic mixing pattern compared to the closely spaced pattern for case 1. Beyond the third cylinder, the vortex scale transitions from characteristic cylinder-size scale to large scale vortex that we denote as a mid-size vortex. A schematic depiction of the different vortex scales are shown in Figure 5.11. The time-averaged scalar field shown in Figure 5.5 indicates much stronger lateral spread of the scalar plume than that for case 1. Clearly, this means there must be an optimum longitudinal spacing $L_{G,opt/D}$ where lateral mixing is maximized. Beyond this optimum spacing, it can be expected that the interaction between individual vortex-wake regions becomes weaker resulting in a decrease in lateral mixing that may very well approach the limit of a single obstacle at some reasonable spacing. Evidence from previous studies suggests that this limit is of the order $L_G/D = 15$ (Zhang and Zhou 2001). This remains to be verified through further simulations.

Cross-sectional profiles of the downstream wakes are shown in Figure 5.7 using the time-averaged fields. These profiles are taken at $x = 120$, 160, and 200 m for case 1 (shown in the left panel) and $x = 200$, 400, and 600 m for case 2 (right panel). Please note that each time-averaged concentration profile is normalized by the maximum value at the given cross section. Table 5.2 shows the statistics for the cross sections shown in Figure 5.7. In this figure, the blue straight line and the red dotted-dash line denote the concentration distribution in the wake between the adjacent cylinders

while the black dashed line shows concentration profile in the wake beyond the third cylinder. The two sets of profiles clearly indicate the effect of the longitudinal spacing. Figure 5.7(a) shows how the close spacing prevents any noticeable lateral spread of the scalar (at x=120 m and 160 m) while the occurrence of the cylinder-size vortices far field promotes enhanced lateral mixing (at x=700 m). On the other hand, for case 2, with significant larger spacing, the lateral plume spread is substantial between adjacent cylinders. This is reflected in the mean and peak values as shown in Table 5.2. Notice how the distributions are peaked (high kurtosis values especially for case 1) in the near field and approach a Gaussian distribution far field (with kurtosis close to 3).

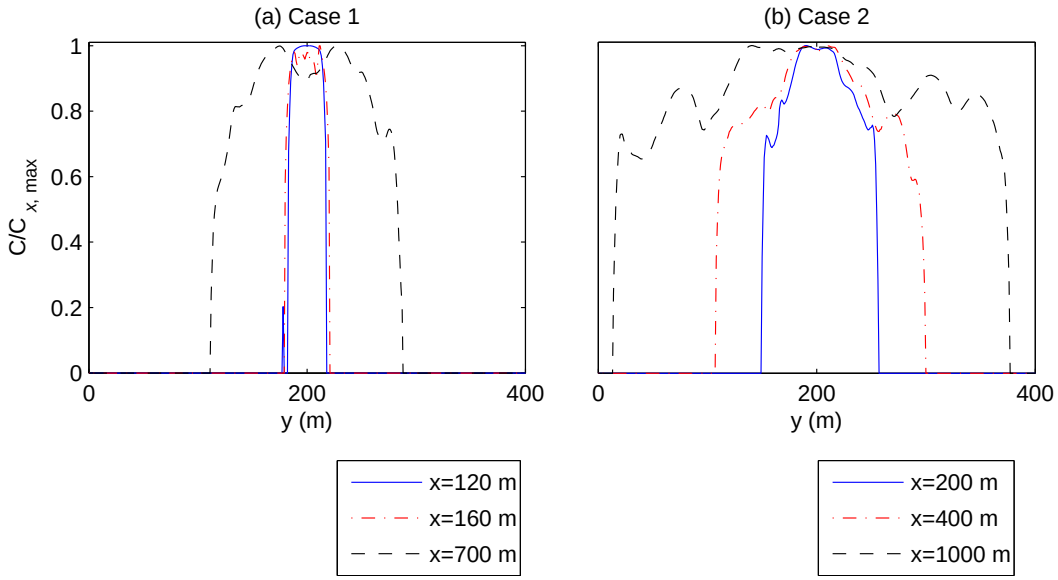

Figure 5.7: Time-averaged scalar profiles at (a) x = 120, 160, and 200 m for case 1, and (b) x = 200, 400, and 600 m for case 2. Blue straight line, red dotted-dash line, and black dash line denote the profiles at the three given cross sections, respectively. The values of the time-averaged concentration are normalized by the maximum values at the given cross section.

Table 5.2: Time-averaged statistics of the profiles depicted in Figure 5.7.

Case No.	Location of Cross-section (m)	Standard deviation σ ($\times 10^{-5}$)	Skewness γ	Kurtosis β	Mean C ($\times 10^{-5}$)	Peak value ($\times 10^{-5}$)
Case 1	120	3.61	-2.00	7.63	4.01	25.52
	160	4.77	-1.19	3.51	4.91	24.27
	700	0.33	-0.53	2.61	0.95	1.85
Case 2	200	0.59	-1.62	4.58	0.26	2.83
	400	0.76	-1.38	3.70	0.42	3.44
	1000	0.29	-1.11	2.82	0.35	1.24

5.3.2 Staggered array cases

The interaction of vortices and downstream wakes around a staggered array consisting of the eight cylinders in a model open channel domain is shown as a time sequence of the passive scalar field in Figures 5.8 and 5.9 with lateral and longitudinal spacings of $L_G/D = 2$ and $L_T/D = 2$ (case 3 in Table 5.1), and $L_G/D = 10$ and $L_T/D = 2$ (case 6), respectively. Figure 5.10 shows the concentration field of all the staggered array cases (cases 3-8) at t=16200 seconds. We focus our discussion on vortex shedding, different vortex scales and associated formation of the downstream wakes.

For the staggered array of the obstacles with $L_G/D = 2$ and $L_T/D = 2$ (case 3 in Table 5.1), the cylinders are too close in the lateral and longitudinal directions. The array-size scale vortex are alternatively shed from the upper and lower sides of the array with the cylinder-size scale vortex shedding occurring in the background. At the first row of cylinders, the flow is deflected towards the upper and lower (or rather the outer) cylinders, respectively. This is in agreement with the previous studies by Guillaume and LaRue (1999), Sumner *et al.* (1999), and Zhang and Zhou (2001) where it was found that a lateral spacing of $L_T/D = 1.338 - 1.730$ is required for quasi-stable modes to develop for three side-by-side cylinders placed normal to the flow. The larger longitudinal spacing between the subsequent rows of cylinders for case 6 permits the cylinder-size scale vortices to develop (see Figure 5.9) compared

to case 3 where they are attenuated (see Figure 5.8). For case 6, the cylinder-sized vortices further promote a well mixed array-size scale vortex to form.

Figure 5.10 shows the different complex vortex patterns that emerge for all the 6 different cases (cases 3-8). For case 3, the closed spaced array of cylinders serve to act as one big obstacle of the order of the array size, and exhibit plume spread similar to what would be expected from a single obstacle of a similar size. Perhaps cases 5 and 8 serve as suitable examples that demonstrate the full range of vortex scales that are depicted in the schematic in Figure 5.11. Clearly, both the lateral and longitudinal spacing greatly influence the vortex and wake dynamics in such clustered systems. We note that as the extent of the plume reaches the lateral boundaries, the no-flux boundary condition used at these boundaries results in the non-physical longitudinal spreading that is observed as shown in Figure 5.10. A wider computational domain (which was not explored due to computational and time constraints) is required to further explore the intricate dynamics of in these complex flows.

The statistics of the time-averaged fields are shown in Table 5.3. The statistical values are obtained based on the concentration profiles shown in Figures 5.12 and 5.13 for cases 3-5 and cases 6-8, respectively. In Figure 5.12, each panel shows the lateral concentration distribution at $x = 120$, 160, and 700 m. The blue straight line and the red dotted-dashed line show the distributions in the wakes between the cylinders. The concentration distribution at the far-field, $x = 700$ m, is shown in the black dashed line. For the cases 6-8, the lateral distributions are also presented at $x = 200$, 400, and 700 m using similar line specifications used for cases 3-5. Overall, smaller longitudinal spacing (cases 3-5) results in highly peaked distribution with large kurtosis excess compared to the larger spaced cases (cases 6-8) that are fairly well mixed.

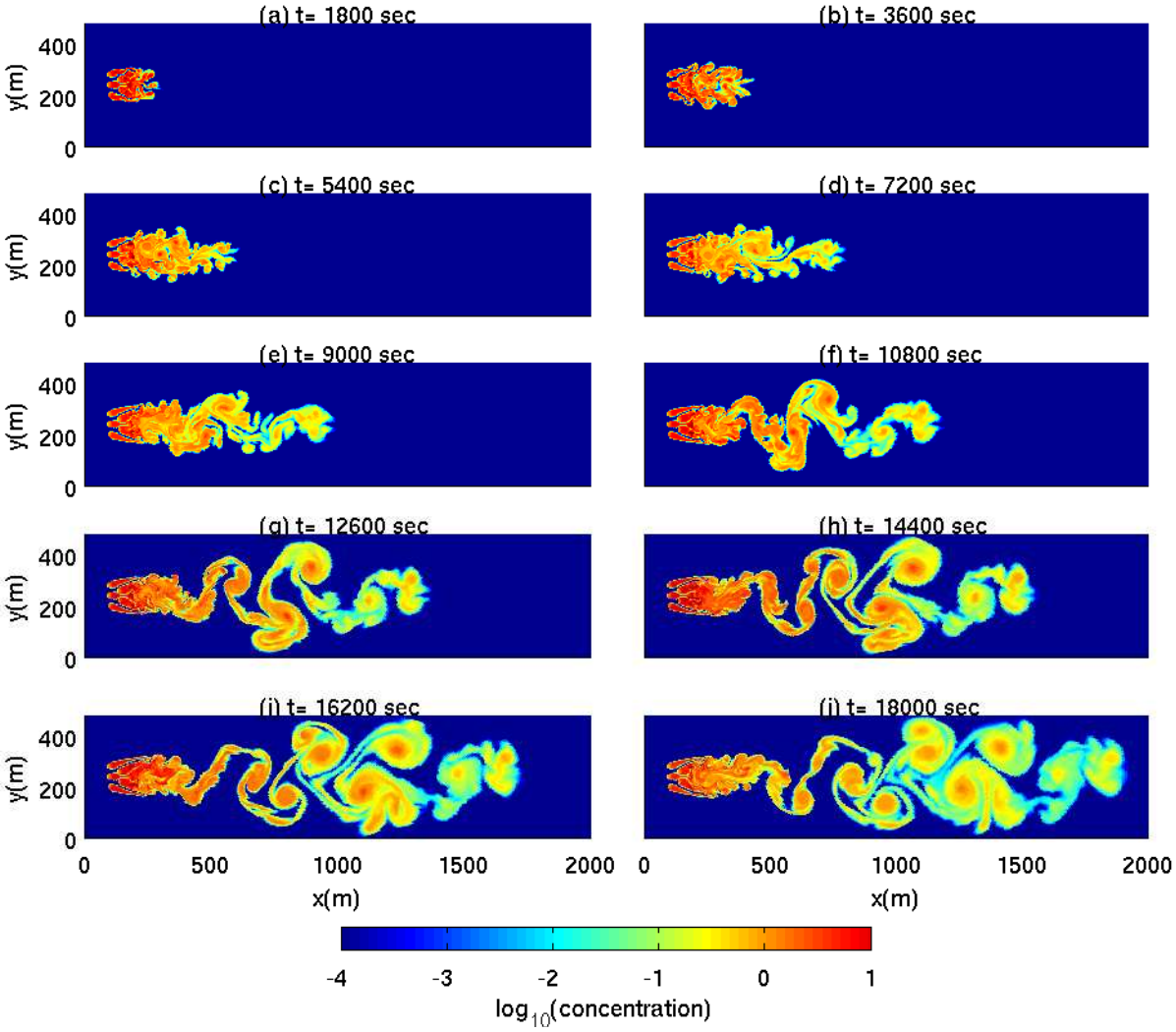

Figure 5.8: Time sequence of passive scalar field around cylinders collocated in a staggered array with $L_G/D = 2$ and $L_T/D = 2$ (case 3 in Table 5.1) at time (a) $t = 1800$ sec, (b) $t = 3600$ sec, (c) $t = 5400$ sec, (d) $t = 7200$ sec, (e) $t = 9000$ sec, (f) $t = 10800$ sec, (g) $t = 12600$ sec, (h) $t = 14400$ sec, (i) $t = 16200$ sec, and (j) $t = 18000$ sec.

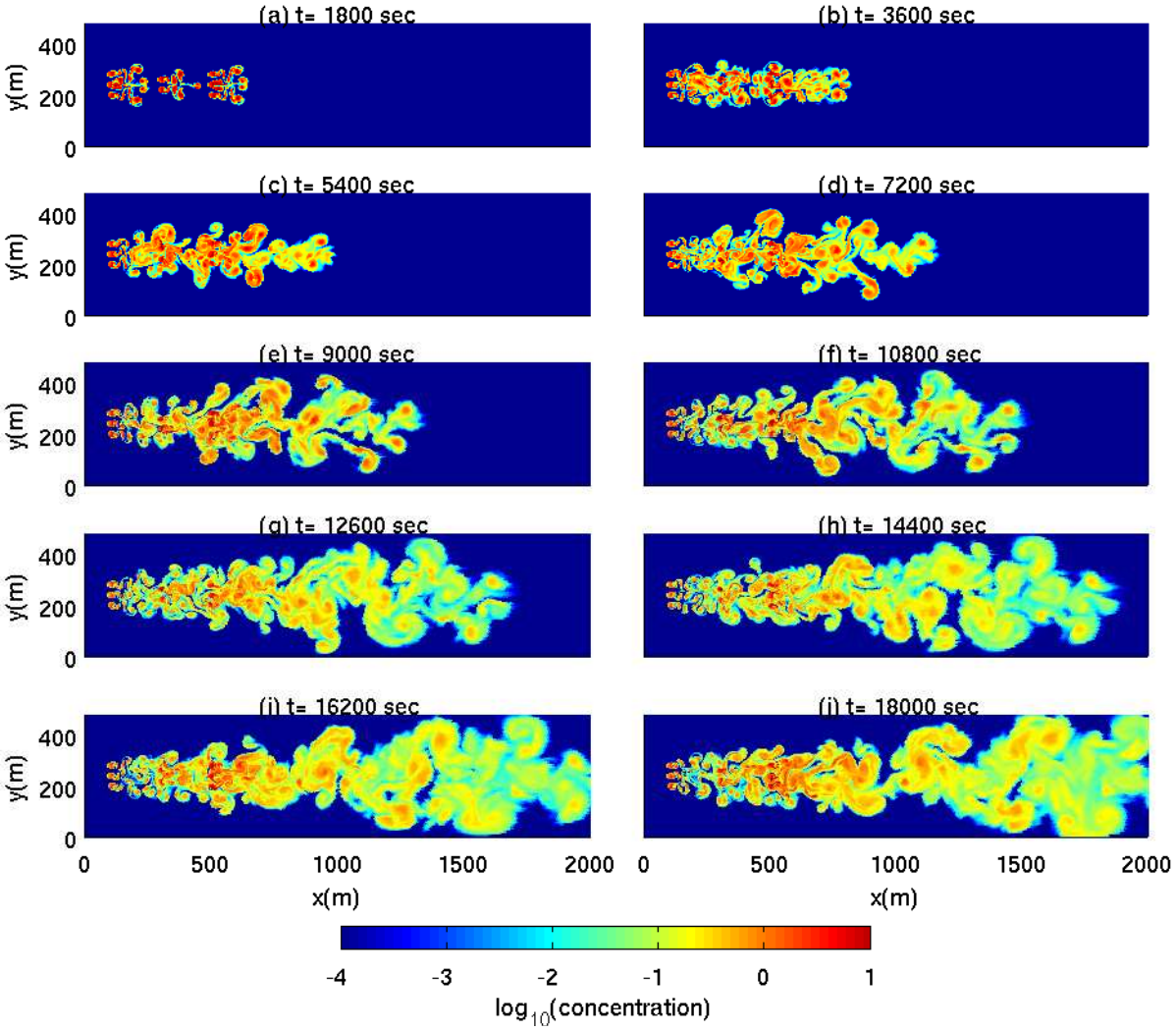

Figure 5.9: Time sequence of passive scalar field around cylinders collocated in a staggered array with $L_G/D = 10$ and $L_T/D = 2$ (case 6 in Table 5.1) at time (a) $t = 1800$ sec, (b) $t = 3600$ sec, (c) $t = 5400$ sec, (d) $t = 7200$ sec, (e) $t = 9000$ sec, (f) $t = 10800$ sec, (g) $t = 12600$ sec, (h) $t = 14400$ sec, (i) $t = 16200$ sec, and (j) $t = 18000$ sec.

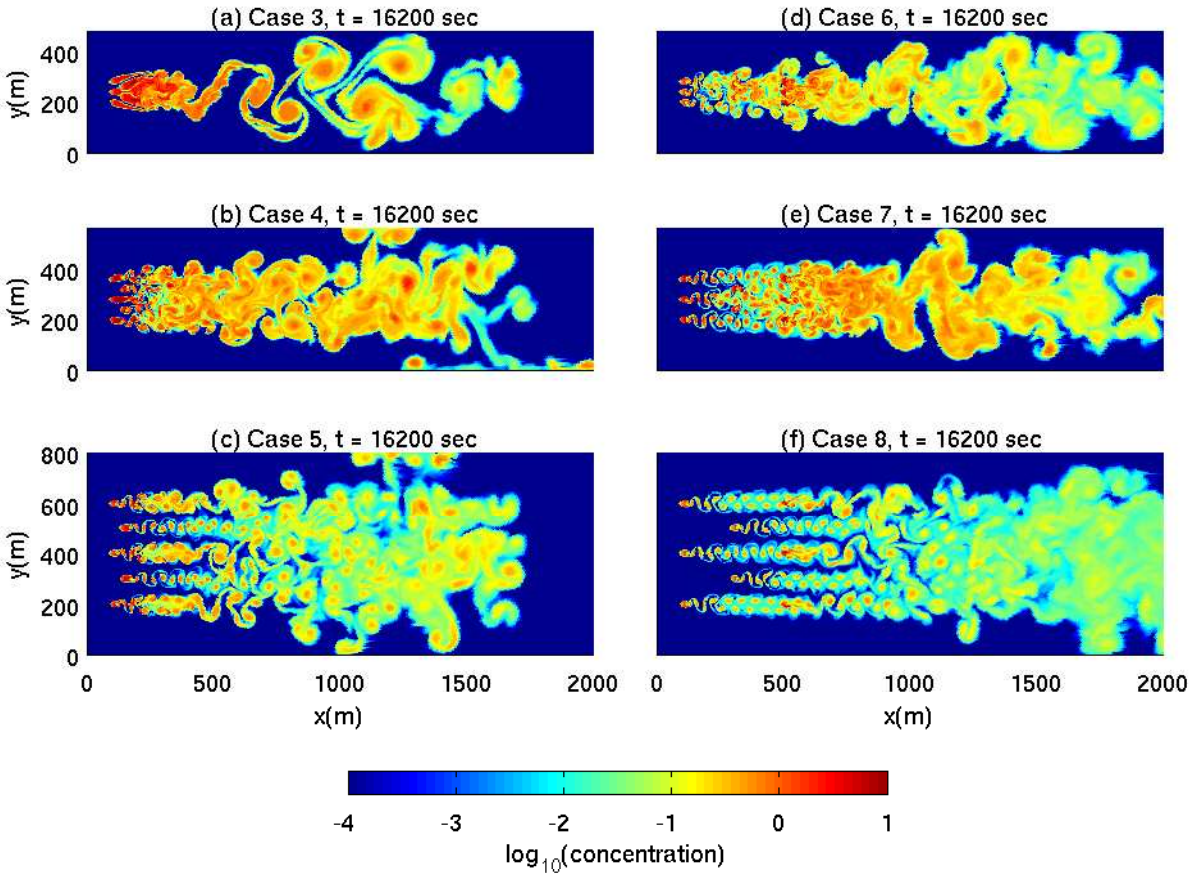

Figure 5.10: Passive scalar fields around a staggered array of cylinders at time $t =$ 16200 sec for (a) Case 3 ($L_G/D = 2$ and $L_T/D = 2$), (b) Case 4 ($L_G/D = 2$ and $L_T/D = 4$), (c) Case 5 ($L_G/D = 2$ and $L_T/D = 10$), (d) Case 6 ($L_G/D = 10$ and $L_T/D = 2$), (e) Case 7 ($L_G/D = 4$ and $L_T/D = 10$), (f) Case 8 ($L_G/D = 10$ and $L_T/D = 10$).

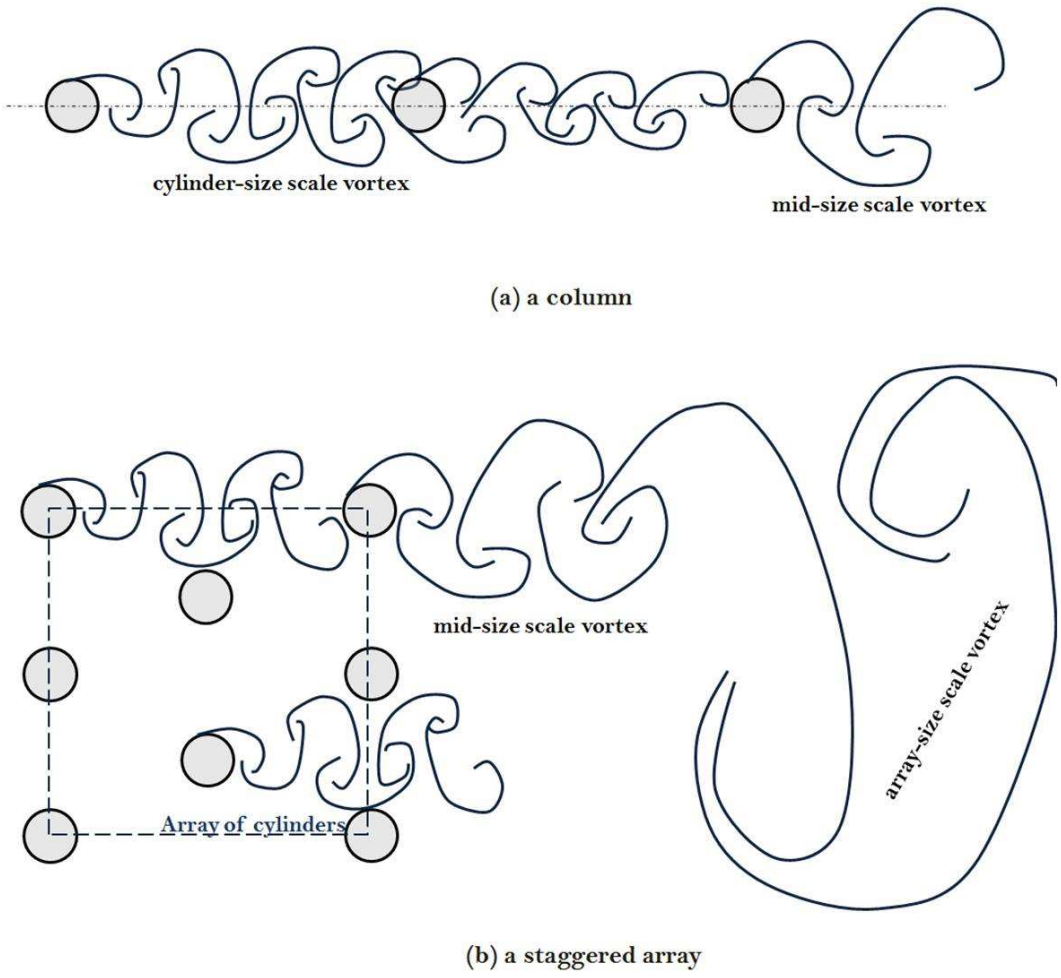

Figure 5.11: A schematic of cylinder-size, mid-size, and array-size scale vortex patterns that form for uni-directional flows around a single column of cylinders and a staggered array of cylinders.

Table 5.3: Statistics of the time-averaged concentrations of the passive scalar around the columns of the cylinders depicted in Figure 5.12 and 5.13.

Case No.	Location of Cross-section (m)	Standard deviation σ ($\times 10^{-5}$)	Skewness γ	Kurtosis β	Mean C ($\times 10^{-5}$)	Peak value ($\times 10^{-5}$)
Case 3	120	3.61	-2.03	7.63	25.52	4.01
	160	4.77	-1.19	3.51	24.27	4.91
	700	0.33	-0.53	2.61	1.85	0.95
Case 4	120	3.73	-2.18	7.87	2.74	24.91
	160	3.13	0.35	2.15	1.63	15.71
	700	0.42	-0.35	2.67	0.93	02.3
Case 5	120	3.09	-0.38	1.65	0.69	12.67
	160	6.15	-1.28	3.01	1.38	22.36
	700	0.20	-0.37	2.77	0.62	1.23
Case 6	200	0.41	-0.79	3.85	0.78	2.89
	400	0.97	-0.55	1.94	1.29	4.37
	700	0.80	-0.41	2.46	1.47	4.10
Case 7	200	0.55	-1.13	3.40	0.48	2.91
	400	0.52	-0.26	2.74	0.84	3.17
	700	0.49	-1.18	4.80	1.21	3.23
Case 8	200	0.63	-0.75	2.84	0.35	3.31
	400	0.67	0.19	2.12	0.49	3.40
	700	0.54	-0.07	2.13	0.77	2.64

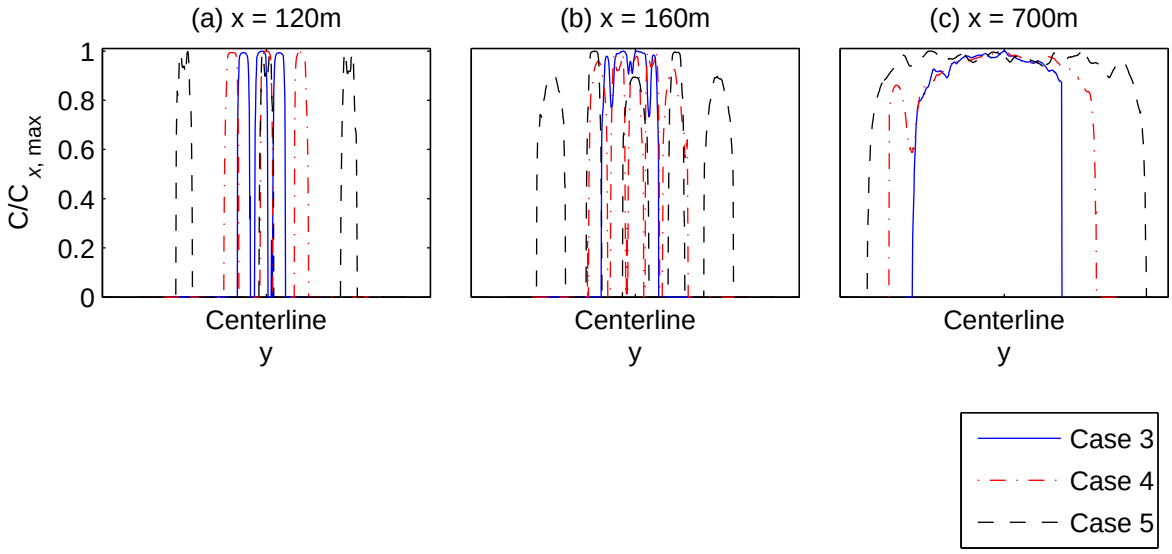

Figure 5.12: Time-averaged non-dimensional concentration at cross sections of (a) $x = 120$ m, (b) $x = 160$ m, and (c) $x = 700$ m for Cases 3-5. Blue straight line, red dotted-dash line, and black dash line describes the lateral time-averaged normalized concentration profile at the first, second, and third give cross section, respectively. The values of the time-averaged concentration are normalized by the maximum values at the given cross section.

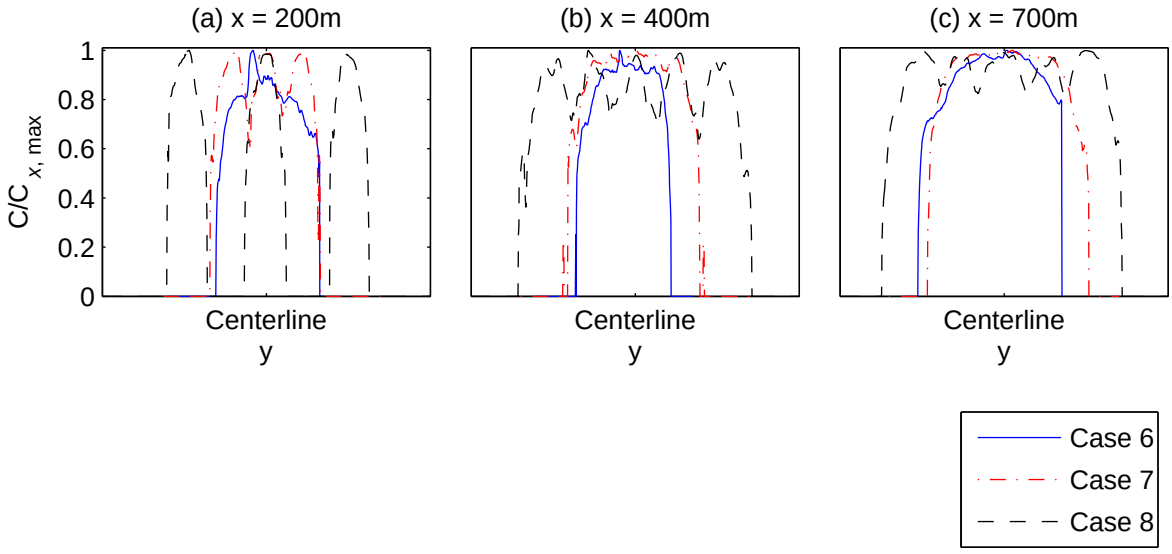

Figure 5.13: Time-averaged non-dimensional concentration at cross sections of (a) $x = 200$ m, (b) $x = 400$ m, and (c) $x = 700$ m for Cases 6-8. Blue straight line, red dotted-dash line, and black dash line describes the lateral time-averaged normalized concentration profile at the first, second, and third give cross section, respectively. The values of the time-averaged concentration are normalized by the maximum values at the given cross section.

5.4 Summary

In this study, we have performed a series of highly-resolved depth-averaged numerical simulations to understand the lateral mixing of passive scalars through and around multiple cylindrical obstacles. The simulation results of flow around multiple obstacles highlight the complex vortex and downstream wake patterns arising from two different array configurations, namely: (i) three cylinders located in a column to study the effect of longitudinal spacing, (ii) a staggered array consisting of eight cylinders to study the vortex patterns that emerge due to both lateral and longitudinal spacing. Various scale vortices are formed depending on both lateral and longitudinal spacing between the obstacles. This study confirms that the importance of the obstacle locations in promoting vortex interactions and lateral mixing. Hence, the spacing of obstacles is one of the most important parameters (others being flow and environmental conditions) for predicting environmental impacts of pollutants. Furthermore, this study can be easily extended to study dynamic loading and power generation problems in wind engineering.

Extensions of this study focusing on the effect of different hydrodynamic conditions such as time-varying flow and the earths rotation are discussed by means of an application study in Chapter 6.

Chapter 6

Application: Modeling of aquaculture dissolved waste transport in a coastal embayment [1]

6.1 Introduction

The subject of this chapter is on modeling the mixing and transport of dissolved waste (considered as a passive scalar in this study) such as nitrogen and phosphorus from aquaculture pens using high-resolution, two-dimensional, depth-averaged numerical simulations under different time-varying flow conditions in an idealized coastal embayment. The rapid expansion of marine aquaculture is a potential solution to the problem of overfishing and fisheries depletion worldwide, but also a major threat to ocean ecosystem. One of the most widely cited but poorly quantified impacts of open netpen aquaculture is its release of nutrients and other wastes to the surrounding environment (Naylor and Burke 2005). There is very little work in the refereed lit-

[1] This chapter has been published in substantial part as "Numerical modeling of aquaculture dissolved waste transport in a coastal embayment", by S. K. Venayagamoorthy, H. Ku, O. B. Fringer, A. Chiu, R. L. Naylor and J. R. Koseff in *Environmental Fluid Mechanics*,**11**, pp 329-352, (2011).

erature describing the dispersal of aquaculture wastes under varying hydrodynamic conditions at the field scale. Previous numerical studies have focused mostly on the near-field mixing under steady uni-directional flow conditions (Helsley and Kim 2005). Some recent field measurements on mussel and shellfish aquaculture identify the environmental impacts of large farms which include wave attenuation and flow suppression due to interaction with stratification (Delaux *et al.* 2010; Plew *et al.* 2006; Stevens *et al.* 2008). The complex nature of the flow around fish pens is caused by flow separation due to partial blockage of the flow by the pens and the combined effects of tides and winds. At larger scales, the influence of the earth's rotation becomes important and can alter the evolution of the waste plume considerably.

The goal of this chapter is to highlight the different dispersal patterns that may occur under various forcing scenarios (flows, tides, earth's rotation, and local sources) in an idealized coastal embayment. The layout of this chapter is as follows: In Section 6.2, we briefly describe the computational approach we employ for this study. Section 6.3 provides an overview of the problem set-up and a summary of all the simulation cases that will be discussed in Section 6.4. We then present and discuss results of the lateral mixing of a continuous pollutant source emanating from an array of aquaculture pens in a idealized coastal embayment under different flow conditions in Section 6.4. Finally we draw some conclusions and provide some directions for future work in Section 6.5.

6.2 Numerical methodology

The SUNTANS research code is employed to perform highly resolved simulations of flow through and around aquaculture open netpens in the idealized coastal embayment shown in Figure 6.1. SUNTANS is an unstructured, finite-volume, parallel coastal-ocean simulator, that solves the three-dimensional nonhydrostatic Navier-

Stokes equations with the Boussinesq approximation in a rotating frame. It also solves for the free surface, and the transport of salinity and temperature (see Fringer *et al.* 2006 and Wang *et al.* 2008 for details). However, in this study, we employ the depth-averaged formulation of SUNTANS using a single vertical layer for all simulations. The governing equations revert to the two-dimensional shallow water equations (also known as the Saint-Venant equations), together with the depth-averaged continuity equations given by

$$\frac{\partial u}{\partial t}+u\frac{\partial u}{\partial x}+v\frac{\partial u}{\partial y}-fv=-g\frac{\partial h}{\partial x}+\nu_H\left(\frac{\partial^2 u}{\partial x^2}+\frac{\partial^2 u}{\partial y^2}\right)+\frac{\tau_x^s}{H}-C_{DB}\frac{\sqrt{u^2+v^2}}{H}u+F_{D,x}, \quad (6.1)$$

$$\frac{\partial v}{\partial t}+u\frac{\partial v}{\partial x}+v\frac{\partial v}{\partial y}+fu=-g\frac{\partial h}{\partial y}+\nu_H\left(\frac{\partial^2 v}{\partial x^2}+\frac{\partial^2 v}{\partial y^2}\right)+\frac{\tau_y^s}{H}-C_{DB}\frac{\sqrt{u^2+v^2}}{H}v+F_{D,y}, \quad (6.2)$$

$$\frac{\partial h}{\partial t}+\frac{\partial}{\partial x}(Hu)+\frac{\partial}{\partial y}(Hv)=0, \quad (6.3)$$

where $H=h+d$ is the total water depth in m, h is the free-surface height relative to some vertical datum in m, d is the depth of the bottom relative to some vertical datum in m, u, v are the horizontal cartesian components of the depth-averaged velocity vector in m s^{-1}, t is time in s, g is the constant of gravitational acceleration in m s^{-1}, $f=2\Omega_{earth}\sin\phi_{lat}$ is the Coriolis parameter with Ω_{earth} the angular velocity of the earth's rotation in s^{-1} and ϕ_{lat} the latitude, ν_h is the horizontal eddy viscosity in m^{2}s^{-1}, τ_x^s and τ_y^s are the free-surface stresses at $z=h$, C_{DB} is a non-dimensional bottom drag coefficient and $F_{D,x}$ and $F_{D,y}$ are the pen induced drag forces in the x and y directions respectively, and are given by a quadratic drag law formulation as shown in Equation (6.5).

We opted to use the two-dimensional depth-averaged formulation since this study is a first step in addressing far-field influence of the near-field dynamics, with a particular emphasis on the near-field vortex street which is predominantly two-dimensional. Furthermore, the two-dimensional highly resolved simulations on their own are com-

putationally intensive and therefore three-dimensional simulations and associated parameter studies were not feasible due to computational and time constraints for the scope of work performed using the two-dimensional simulations.

6.3 Problem configuration and simulation cases

6.3.1 Problem configuration

The domain we use in this study is a model coastal embayment that is 10 km in length and 5 km wide as shown in Figure 6.1. The bathymetry of the domain consists of a shallow embayment incised by a deep channel as shown in Figure 6.2. Two sets of six 20 m diameter fish pens, as shown in Figure 6.1, are all located close to the western edge of the embayment. The effect of varying the location of the pens on the dispersal of the waste plume is presented in Section 6.4.

At the alongshore boundaries of the domain shown in Figure 6.1, we impose a velocity field of the form

$$v = U_m + U_T sin(\omega t), \tag{6.4}$$

where $U_m \leq 0$ is the amplitude of the mean current (where flow is in the north-south direction); U_T is the amplitude of the sinusoidal component of the flow field with forcing frequency ω; and v is the alongshore component of the velocity field. Boundary conditions for the horizontal velocity v are free-slip along the coastline and offshore boundary. The horizontal component in the x-direction of the velocity field u has no-flux boundary conditions along the coastline and the offshore boundary. The scalar field has no-flux boundary conditions on all boundaries.

An unstructured mesh is generated for this study with a total of approximately 162,500 cells, with grid refinement in the vicinity of the fish pens as shown in Figure 6.1. The resolution near the pens is roughly 5 m, while that in the far-field is stretched

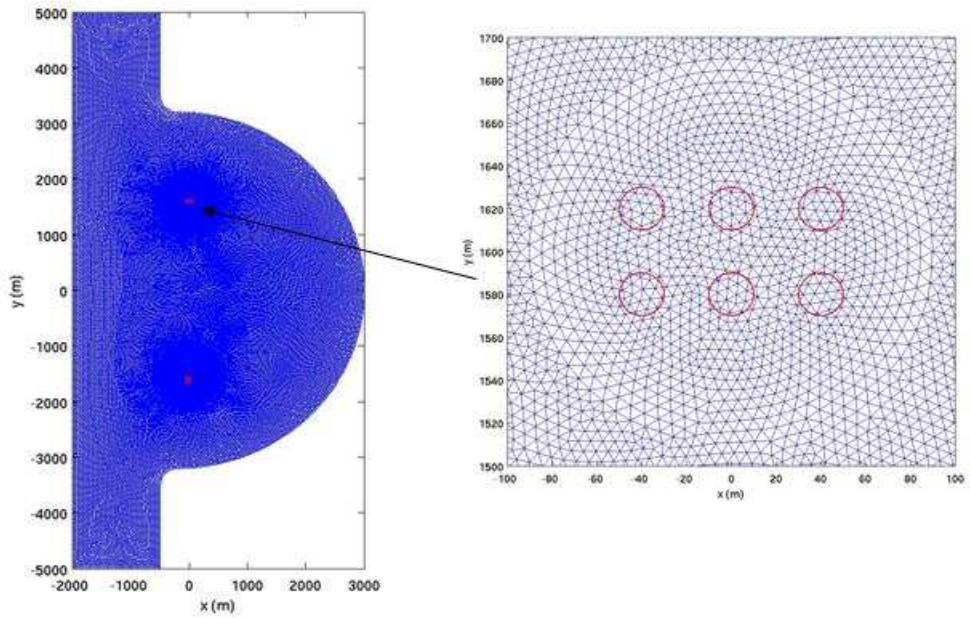

Figure 6.1: Unstructured computational mesh of the model coastal embayment used in the simulations for this study. A velocity field described by Equation (6.4) is imposed at the northern boundary of the domain with a M_2 tidal frequency of $\omega = 1.4 \times 10^{-4}$ rad s^{-1}. The image on the right shows a zoomed view highlighting the grid refinement around an array of six 20 m diameter pens.

to 50 m. Each individual fish pen is cylindrical in shape with a diameter of $D = 20$ m. A drag law formulation is used to account for the flow reduction inside the pens and the resulting decrease in momentum downstream of the pens. This quadratic drag law formulation is represented on the right-hand side of the x- and y-momentum equations shown in Equations (6.1) and (6.2) given by

$$F_{D,x} = -\frac{\alpha C_D (u^2 + v^2)^{1/2}}{D} u,$$
$$F_{D,y} = -\frac{\alpha C_D (u^2 + v^2)^{1/2}}{D} v, \tag{6.5}$$

where C_D is the non-dimensional drag coefficient exerted by the fish pens; u and v are the Cartesian components of the velocity vector; and $\alpha = 1$ inside of the pens while $\alpha = 0$ outside of the fish pens. We use a horizontal eddy-viscosity of ν_h=10^{-3} m^2 s^{-1},

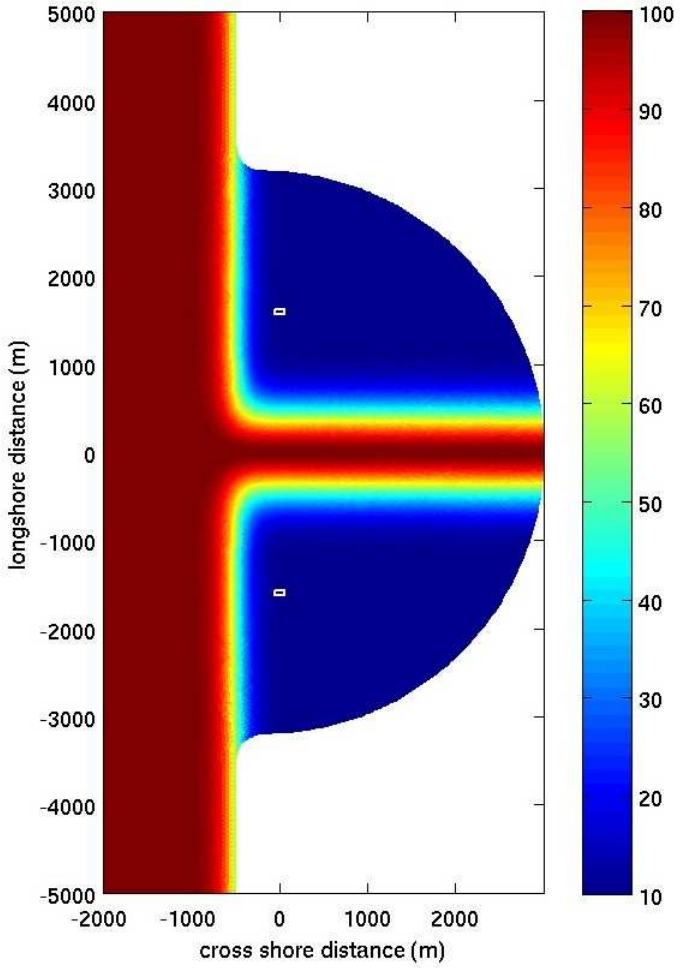

Figure 6.2: Idealized depth contours of the model embayment depicting a shallow shelf incised by a deep channel. Locations of model fish pens are depicted by the white boxes (for the offshore cases listed in Table 6.1). The depth is indicated by the color bar in meters.

and a quadratic bottom drag law formulation (as represented on the right-hand side in Equations (6.1) and (6.2) with a bottom drag coefficient of $C_{DB} = 0.0025$. An estimate of the Reynolds number based on the pen diameter of D=20 m with a characteristic velocity scale of 0.1 m s^{-1} and ν_h =10^{-3} m^2 s^{-1} is $Re = 2000$. A continuous pollutant (scalar) point source is placed inside the perimeter of each pen as an approximation of the effluent waste discharged from the pens. No horizontal diffusivity is applied for all simulations since it is assumed that transport dominates

the dispersion. Transport is computed using a highly resolved total variation diminishing (TVD) scheme which is explicit and hence conditionally stable but guarantees monotonicity (Zhang *et al.* 2011). Time step is restricted using a maximum Courant number of roughly 0.5 based on the smallest grid spacing and maximum currents. This limitation provides sufficient temporal resolution while satisfying stability.

For the simple model flow problem, there are two important non-dimensional parameters. The first parameter, defined by Equation (6.4), is the ratio of the tidal to mean flow given by

$$\eta = \frac{U_T}{U_m}, \tag{6.6}$$

which compares the amplitude of the oscillatory flow to the amplitude of the mean current and determines the shape of the contaminant plume (Purnama and Kay 1999). The other parameter is the non-dimensional tidal excursion length scale given by

$$K = \frac{2U_T}{\omega D}, \tag{6.7}$$

where U_T is the amplitude of the tidal current; ω is the forcing frequency; and D is the fish pen diameter. This parameter describes the ratio of the tidal excursion to the pen diameter, which is known as Keulegan-Carpenter number in wave-structure interaction studies (Keulegan and Carpenter 1958). For all of the simulations performed in this study, we have used an alongshore velocity magnitude of $U_m = 0.1$ m s^{-1}, which is representative of mean currents in coastal regions such as the St. Lawrence Island in the Bering Sea. The tidal velocity magnitude is varied to yield different (field-scale) values of η and K. In Section 6.4, we discuss the influence of these and other parameters on the dispersion of a contaminant plume in the idealized coastal embayment shown in Figure 6.1.

A dimensionless number that is used to quantify the significance of rotational (Coriolis) effects is the Rossby number and is given by

$$Ro = \frac{U_m}{fL}, \tag{6.8}$$

where f is Coriolis parameter (depends on the latitude); and L is a characteristic length scale (which is taken as the embayment width of 5 km) The Rossby number is a ratio of inertial forces to Coriolis forces which result from the Earth's rotation.

6.3.2 Simulation cases

A total of 7 simulations of the coastal embayment were performed for a number of different flow conditions and pen locations as shown in Table 6.1. Offshore cases (cases 1-4) and nearshore cases (cases 5-7) are used to investigate the effect of pen location on plume dispersion. Case 1, which we refer to as 'offshore bases case', takes into account the drag exerted by each of 12 pens with $C_D = 1$. The earth's rotation is included with Coriolis coefficient of $f = 8.7 \times 10^{-5}$ rad s^{-1}. The flow field is driven by a tidal flow from north to south combined with a northerly flowing mean current as described by Equation (6.4). The relevant oscillating flow parameters are $\eta = 1$ and $K = 71$, based on a tidal velocity amplitude of $U_T = 0.1$ m s^{-1} and M_2 tidal period of 12.42 hours.

Case 2 shows a similar simulation to case 5 except that here, the Coriolis terms in the momentum equations ((6.1) and (6.2)) were switched off by simply setting f=0 (i.e. $Ro = \infty$). Case 3 presents a simulation where we have added a river inflow to case 1, with all other parameters kept identical to case 1. A small river inflow river discharge with a velocity of U_R=0.05 m s^{-1} was placed symmetrically at the channel incision at the central embayment coast (i.e. at a alongshore distance of 0 m). The width of the river inflow is 400 m and the discharge is approximately 1500 m^{3}s^{-1}. This

Table 6.1: Summary of the seven cases simulated in this study. The last column provides some remarks where the Rossby number and other variables and/or comments are shown.

Case #	Case Name	Domain	C_D	η	K	Remarks
1	Offshore base case	Embayment	1.0	1	71	Ro=0.26
2	Offshore with no rotation	Embayment	1.0	1	71	$Ro = \infty$
3	Offshore with river inflow	Embayment	1.0	1	71	$U_R/U_m = 0.5$
4	Offshore with no pen drag	Embayment	0	1	71	Ro=0.26
5	Nearshore base case	Embayment	1.0	1	71	Ro=0.26
6	Nearshore with strong tides	Embayment	1.0	2	71	Ro=0.26
7	Nearshore with wind	Embayment	1.0	∞	71	$u_{10} = 10$ m/s

is about 10 percent of the volume flow rate entering the embayment from the northern alongshore boundary from the mean and tidally-induced flow. Case 4 is a simulation where the pen-induced drag is switched off (C_D=0) with all other parameter kept identical to the 'offshore base case' (case 1).

For nearshore cases (case 5-7), the southern facing farm in Figure 6.1 was moved into the bay and closer to the channel incision (see Figure 6.7). Case 5 is what we refer to as 'nearshore base case'. Here, except for the southern farm location, all other conditions are identical to the 'offshore base case' (case 1). In case 6, we take into account a stronger tidal with $\eta = 2$. When $\eta > 1$, flow reversals will occur and dramatic changes on the plume structure can be expected. Case 7 presents a nearshore simulation where surface wind stress acts over the entire embayment in a northward direction (i.e. opposite to the mean current flow). We have also removed the mean current for this case in order to explore the effect of the wind-induced circulation on the plume distribution.

6.3.3 Statistical parameters

We assess the plume distribution using statistical indicators such as moments of non-dimensional concentration field in order to obtain quantitative information on the plume characteristics. Here, we use the mean standard deviation, skewness, and kurtosis of the alongshore concentration distribution. A description of these moments are provided here.

The standard deviation provides a measure of the spread of the concentration plume and is defined as the root-mean-square of the concentration value from the mean given by

$$\sigma = \sqrt{m_2} = \sqrt{\frac{\sum_{j=1}^{N} \left(C_j - \overline{C}\right)^2}{N}}, \tag{6.9}$$

where $\overline{C}$ is the mean of the concentration distribution; N is the sample size; and m_2 is the variance or the second moment about the mean. The skewness is defined as the third moment about the mean normalized by the cube of the standard deviation in a form of

$$\gamma = \frac{m_3}{\sqrt{m_2^3}} = \frac{\frac{1}{N}\sum_{j=1}^{N} \left(C_j - \overline{C}\right)^3}{\left(\frac{1}{N}\sum_{j=1}^{N} \left(C_j - \overline{C}\right)^2\right)^{3/2}}. \tag{6.10}$$

This shows the degree of asymmetry of a distribution compared with the Gaussian distribution that is in perfectly symmetrical. The fourth moment about the mean normalized by the variance (known as the kurtosis) provides a measure of peakedness of a distribution usually taken relative to a Gaussian distribution and is given by

$$\beta = \frac{m_4}{m_2^2} = \frac{\frac{1}{N}\sum_{j=1}^{N}\left(C_j - \overline{C}\right)^4}{\left(\frac{1}{N}\sum_{j=1}^{N}\left(C_j - \overline{C}\right)^2\right)^2}. \tag{6.11}$$

A concentration distribution with large kurtosis indicates strong intermittency while a distribution with large skewness indicates a highly asymmetrical distribution.

6.4 Results

Here, we present simulation results of the coastal embayment under different flow conditions and fish pen locations.

6.4.1 Offshore cases

Offshore base case (Case 1)

The passive scalar concentration field from a simulation run with two sets of fish farm pens located along the edge of the embayment is shown in Figure 6.3 as a time sequence over a duration of six tidal periods. For this 'offshore base case', we have included the drag induced by each of the pens on the flow field and have also taken into account the earth's rotation. Using a Coriolis parameter of $f = 8.7 \times 10^{-5}$ rad s^{-1}, and the embayment width as the length scale, the Rossby number for this case is $R = U_m/fL = 0.26$, which indicates that the Coriolis force will likely influence the flow dynamics. The flow field is driven by a tidal flow from north to south combined with a southerly flowing mean current. The relevant oscillating flow parameters as shown in Table 6.1 are $\eta = 1$ and $K = 71$, based on a tidal velocity amplitude of $U_T = 0.1$ m s^{-1} and M_2 tidal period of 12.42 hours. The formation of the downstream vortex shedding is evident early on as shown in Figure 6.3 (a). As the flow reverses,

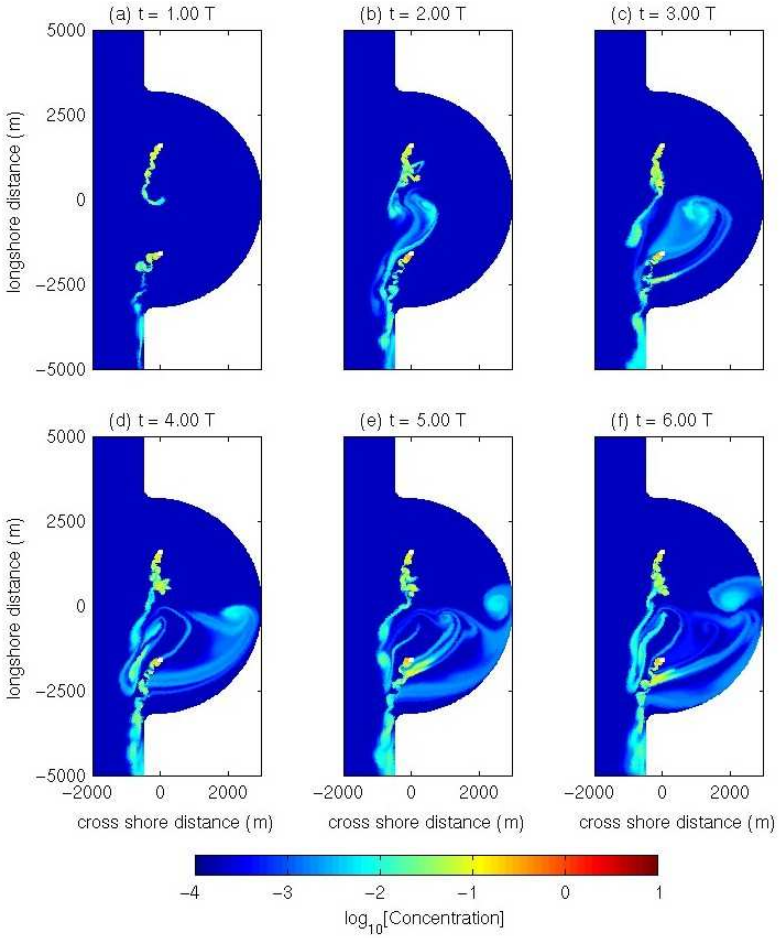

Figure 6.3: "Birds-eye-view" of the normalized concentration in the vicinity if two sets of six 20 m diameter pens (depicted as white boxes) releasing a passive scalar at the edge of the coastal embayment for the 'offshore base case' (case 1).

the plume contracts in a similar manner to that observed for the channel flow case (as discussed in Chapters 3 and 4 respectively). The plume, while predominantly transported downstream (southwards) due to the rather strong mean current, also tends to spread eastward into the bay (see Figure 6.3(c) - (f)).

The concentration distribution for all the offshore cases (case 1-4 in Table 6.1) at time $t = 4$ T is shown in Figure 6.4 to highlight the difference in the plume behavior under different flow conditions. To assess the dispersion characteristics of the concentration plumes, we analyzed longitudinal profiles of the concentration

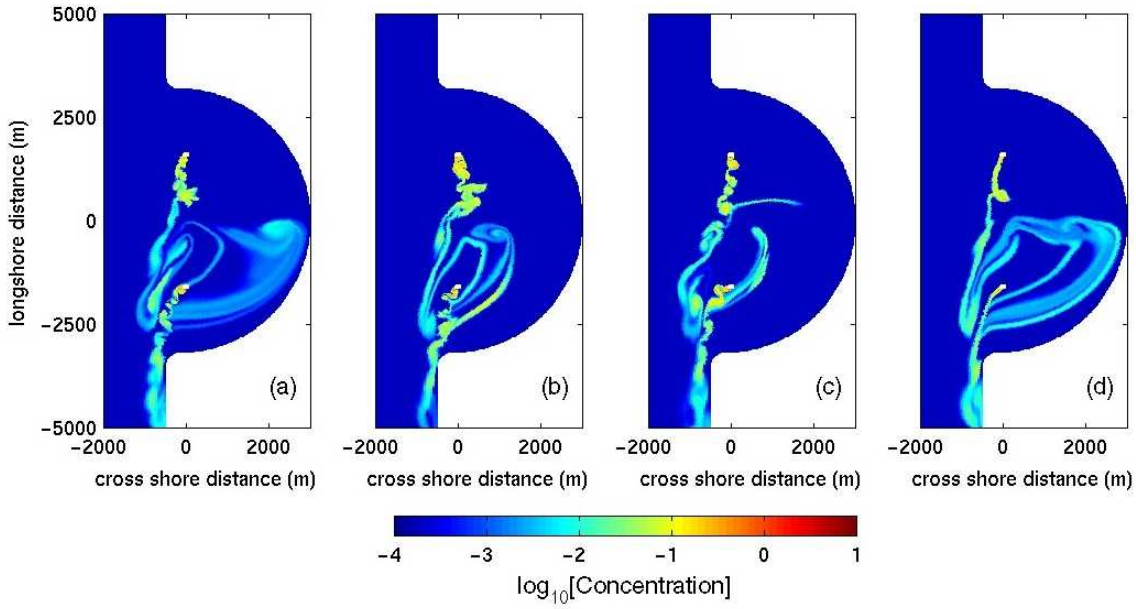

Figure 6.4: "Birds-eye-view" of the normalized concentration in the vicinity if two sets of six 20 m diameter pens (depicted as white boxes) releasing a passive scalar at the edge of the coastal embayment at time $t = 4$ T for (a) offshore base case (case 1), (b) offshore with no rotation case (case 2), (c) offshore with river inflow case (case 3), and (d) offshore with no pen drag case (case 4), respectively.

along the coastline as shown in Figure 6.5 at times $t = 3$ T and 6 T, respectively. The alongshore concentration profiles for cases 6, 7 and 8 are also shown in Figure 6.5 for comparison. These profiles for the 'offshore base cases' clearly show that the waste plume disperses toward the embayment coast albeit at very low concentration levels.

We computed the moments of the alongshore concentration distribution (as discussed in Section 6.3.3) for all the simulations and the statistics are shown in Tables 6.2 and 6.3. Also shown in Tables 6.2 and 6.3 are the peak values of the concentration for all the cases outlined in Table 6.1 at $t = 3$ T and 6 T respectively. Time series of the concentration profiles at three locations along the embayment coastline highlight the temporal intermittency in the concentrations along the embayment coast (see Figure 6.6). Details of the results of these simulations are discussed in what follows.

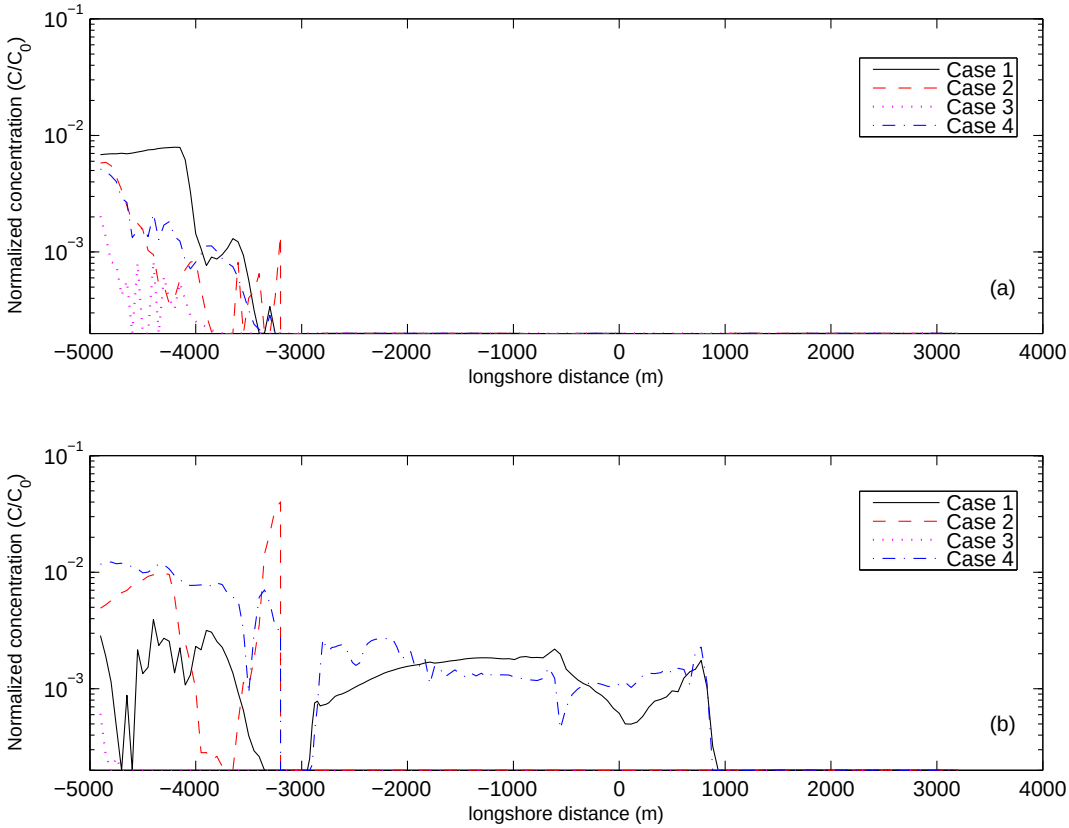

Figure 6.5: Concentration profiles of the passive scalar along the embayment coast line at (a) $t = 3$ T and (b) $t = 6$ T, for the offshore base case (solid line, case 1), offshore with no rotation case (dash line, case 2), offshore with river inflow case (dash-dotted line, case 3) and offshore with no pen drag case (dotted line, case 4), respectively.

Table 6.2: Statistics of the alongshore concentrations depicted in Figure 6.5(a) and 6.9(a) at time $t = 3$ T.

Case #	Case Name	Mean $\overline{C}$ ($\times 10^{-3}$)	Standard deviation σ ($\times 10^{-3}$)	Skewness γ	Kurtosis β	Peak value ($\times 10^{-3}$)
1	Offshore base case	0.61	1.92	3.06	10.58	7.73
2	Offshore with no rotation	0.18	0.78	5.66	36.41	5.69
3	Offshore with river inflow	0.04	0.17	7.18	63.86	1.83
4	Offshore with no pen drag	0.20	0.71	4.69	27.00	4.94
5	Nearshore base case	0.05	0.15	3.64	15.96	0.89
6	Nearshore with strong tides	0.00	0.00	10.24	111.52	0.00
7	Nearshore with wind	0.87	3.00	5.43	34.96	21.26

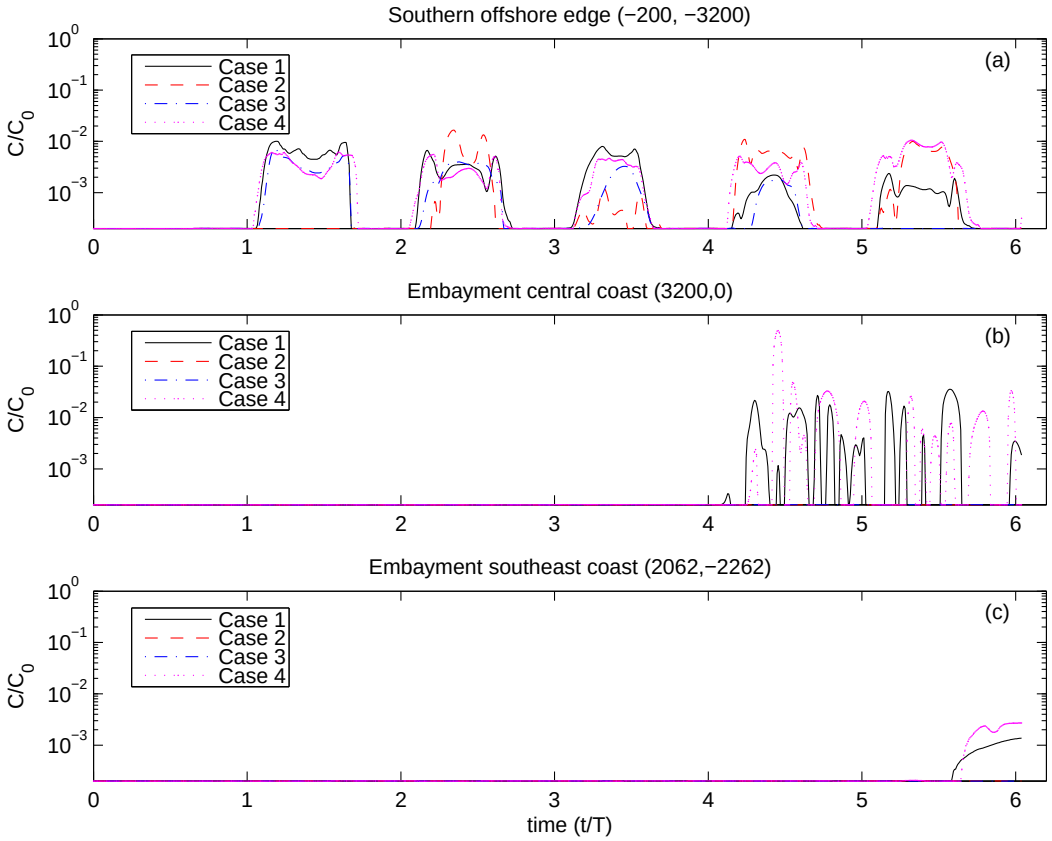

Figure 6.6: Time series of concentration profiles of passive scalar at three different locations along the embayment coast for offshore cases 1, 2, 3 and 4, respectively.

Table 6.3: Statistics of the alongshore concentrations depicted in Figure 6.5(b) and 6.9(b) at time $t = 6$ T.

Case #	Case Name	Mean $\overline{C}$ ($\times 10^{-3}$)	Standard deviation σ ($\times 10^{-3}$)	Skewness γ	Kurtosis β	Peak value ($\times 10^{-3}$)
1	Offshore base case	0.62	0.77	1.11	3.69	3.74
2	Offshore with no rotation	1.09	4.36	6.25	48.66	39.92
3	Offshore with river inflow	0.00	0.00	13.71	195.37	0.41
4	Offshore with no pen drag	1.81	3.10	2.11	6.29	12.07
5	Nearshore base case	2.78	4.52	1.76	5.20	21.80
6	Nearshore with strong tides	0.34	1.21	4.85	28.36	8.92
7	Nearshore with wind	2.36	4.38	2.32	8.13	21.43

Offshore without rotation (Case 2)

The effect of the earths rotation on the dispersion of the plume was investigated by simply switching off the Coriolis term in Equations (6.1) and (6.2) in our numerical code. Figure 6.4(b) shows the concentration field at time $t = 4$ T together with the concentration field for 'offshore base case' for the same time (Figure 6.4(a)). For this scenario, it is seen that the plume does not spread deep into the embayment. The kurtosis of the alongshore concentration distribution for this case (case 2) are considerably higher than the 'offshore base case' as shown in Tables 6.2 and 6.3. The absence of the Coriolis force implies that the flow field is not deflected into the embayment especially during slack tides when the effects of rotation are expected to be very strong. Hence, when the tide turns, the plume is flushed downstream (southwards) with much higher concentrations as indicated by the high peak in Figure 6.5(b) at $t = 6$ T, resulting in a highly peaked distribution. Furthermore, the asymmetry in the concentration distribution is also enhanced by the absence of the Coriolis forcing as indicated by skewness statistics in Tables 6.2 and 6.3. These results clearly demonstrate that the large scale effect of the earth's rotation does indeed influence the dispersion of such plumes and should not be disregarded in numerical modeling.

Offshore with river inflow (Case 3)

Enclosed coastal embayments may often have rivers discharging into them. A small inflow river discharge with a velocity of U_R=0.05 m s^{-1} was placed at the head of the channel incision as discussed in Section (6.3.2). The resulting plume concentration at $t = 4$ T is shown in Figure 6.4(c). With all other parameters being equal with the 'offshore base case', it is evident (as would be expected) that the plume spread into the embayment is impeded by the river inflow. Both the skewness and kurtosis of the concentration distributions alongshore are considerably higher than the 'offshore base case'. However, in contrast to the previous case (no rotation case), the time sequence

of the plume distributions (not shown here) clearly indicate that the plume does not hug the embayment coast except further downstream resulting in a highly skewed distribution. This is clearly a desirable situation for fishfarm operations since the waste plume is very unlikely to reach the coastline due to the flushing action of the freshwater inflow. For a buoyant river plume, further research using three-dimensional simulations are required to capture the vertical mixing of the river plume with the denser coastal water.

Offshore with no pen drag (Case 4)

The effect of the drag induced by the fish pens causes flow separation and vortex shedding thus enhancing the local mixing as was clearly demonstrated from the results of the open channel cases (Chapters 3, 4 and 5). In an effort to understand the influence of blockage introduced by the pens, we ran an offshore case without accounting for the drag from the pens. For this case, it is clear from the concentration distribution shown in Figure 6.4(d) that the absence of drag results in less mixing compared to the 'offshore base case' shown in Figure 6.4(a), even though the overall plume distribution looks very similar. The peak concentration is at least three times higher than the peak value for the 'offshore base case' as shown in Tables 6.3 at $t = 6$ T. This results in conjunction with the results of the channel flow cases (from earlier chapters) highlights the need to correctly account for the drag induced by the pens in predictive numerical models for water quality applications. An over prediction of the drag (i.e. a higher drag coefficient) will result in a well mixed plume and on the other hand, under prediction (i.e. a lower drag coefficient) of the drag will imply poor mixing conditions.

6.4.2 Nearshore cases

For the nearshore cases (case 5-7), we have moved the southern facing farm into the bay and closer to the channel incision (see Figure 6.7) in order to explore the variability in the plume dispersion as a function of the location of the pens.

Nearshore base case (Case 5)

The concentration distribution for the 'nearshore base case' is shown in Figure 6.7 as a time sequence over six tidal periods. The distributions indicate much higher concentrations closer to the coast compared to the'offshore base case' (case 1, Figure 6.3). The concentration distributions of the plume for case 5 as seen in Figure 6.7 indicate much higher concentrations closer to the coast compared to the 'offshore base case' (case 1). Figure 6.8 shows the concentration distribution at time $t = 4$ T for all the nearshore cases (cases 5, 6 and 7 respectively). As expected, the concentration profiles along the coast as shown in Figure 6.9 are at least an order of magnitude higher than those for the offshore base case' (Figure 6.5) especially at $t = 6$ T. Time series of the concentrations at the three same locations shown for all offshore cases in Figure 6.6 are repeated here for all the nearshore cases (see Figure 6.10). The relocation of the southern farm close to the coast has reduced the concentration at the southern offshore boundary (Figure 6.8(a)) while the concentration at the head of the channel incision has dramatically increased by up to two orders of magnitude (Figure 6.8(b)).

Nearshore with strong tides (Case 6)

The parameter η determines the shape of the plume. In other words, it quantifies the effect of the tidal action to that of the mean current. A higher value of η signifies a stronger tidal signal and allows for a stronger plume reversal. A simulation for the 'nearshore case' was performed with $\eta = 2$ with the results of the concentration

distribution shown in Figure 6.8(b). We see dramatic changes in the plume structure for this case compared to the distribution for the 'nearshore base case' shown in Figure 6.8(a). The plume undergoes a much stronger reversal as the tide changes direction. It is clear from this figure (and other time sequence plots not shown here) that the plume reaches some parts of the northern coast. The strong sloshing motion of the tidal flow in the alongshore direction results in highly peaked and skewed distributions compared to the 'nearshore base case' as shown by the high values of the kurtosis and skewness in Tables 6.2 and 6.3. This result indicates the importance of identifying the correct (and dominant) hydrodynamic conditions at a particular fish farm site because these conditions will dramatically influence how far a waste plume from a fish farm site would spread.

Nearshore with wind (Case 7)

Finally, we present a 'nearshore case' with a surface wind stress acting over the entire embayment in the southerly direction (i.e. opposite to the tidal flow). We have also removed the mean current for this case in order to explore the effect of the wind-induced circulation on the plume distribution. Figure 6.8(c) shows the concentration distribution at $t = 4$ T. The pattern for this case is completely different to those shown earlier. Here, the wind stress used was estimated to yield a mean velocity of 0.1 m s^{-1} based on a mean wind speed $U_{10} = 10$ m s^{-1} at a height of 10 m in the atmospheric boundary layer. Clearly, it is seen that the wind effect is dominant and tends to drive the distribution in a northward direction. This is accentuated even more when the tide reverses and the plume is dispersed more toward the northern end of the bay.

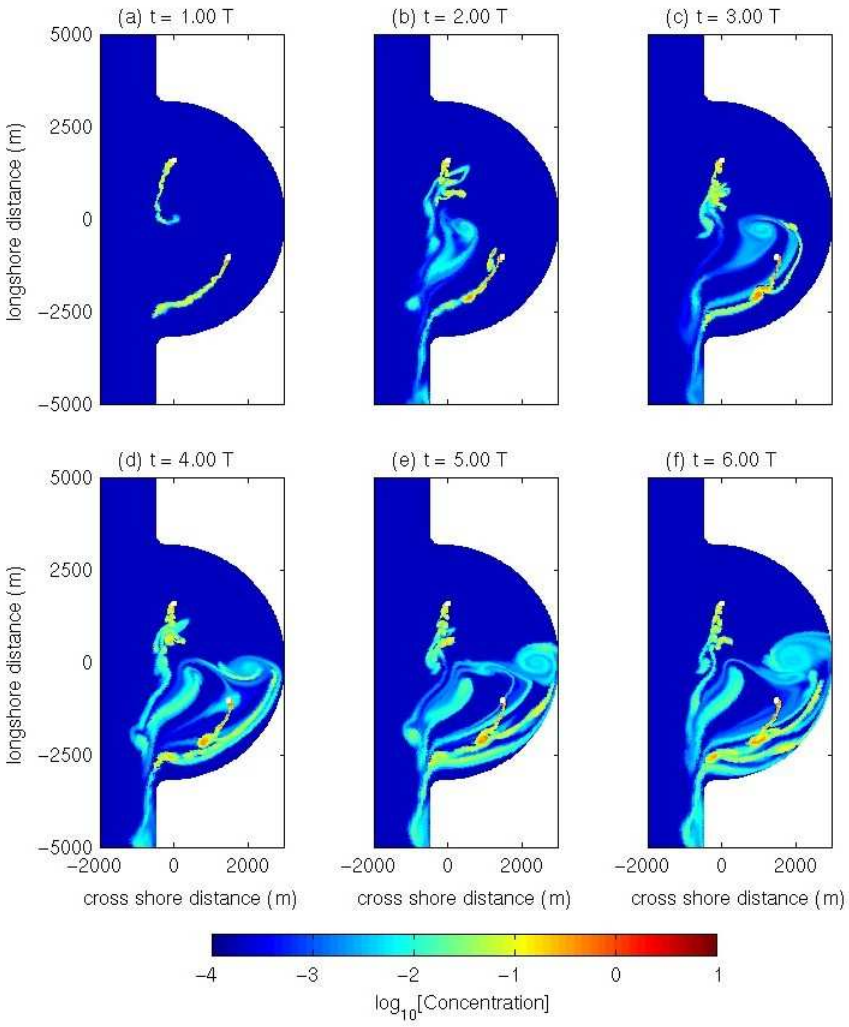

Figure 6.7: "Birds-eye-view" of the normalized concentration in the vicinity if two sets of six 20 m diameter pens (depicted as white boxes) releasing a passive scalar at the edge of the coastal embayment for the 'nearshore base case' (case 5).

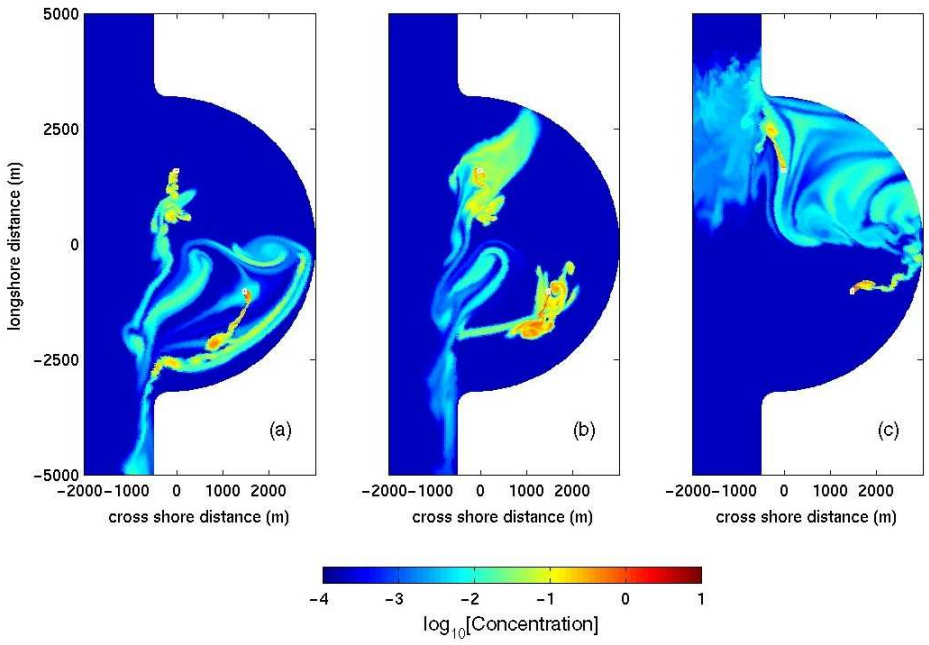

Figure 6.8: "Birds-eye-view" of the normalized concentration in the vicinity if two sets of six 20 m diameter pens (depicted as white boxes) releasing a passive scalar at the edge of the coastal embayment at time $t = 4$ T for (a) nearshore base chase (case 5), (b) nearshore with strong tides case (case 6), (c) nearshore with wind case (case 7), respectively.

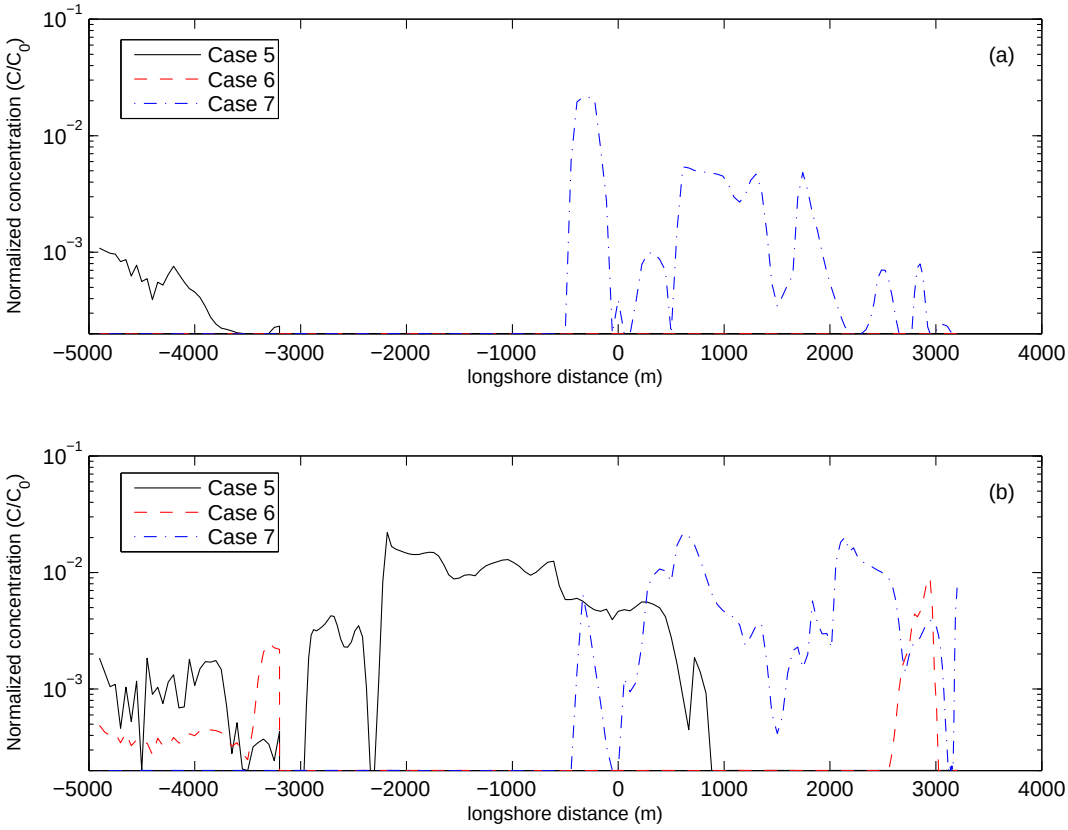

Figure 6.9: Concentration profiles of the passive scalar along the embayment coast line at (a) $t = 3$ T and (b) $t = 6$ T, for the nearshore case (solid line, case 5), nearshore case with strong tides (dash line, case 6), and nearshore case with wind (dash-dotted line, case 7), respectively.

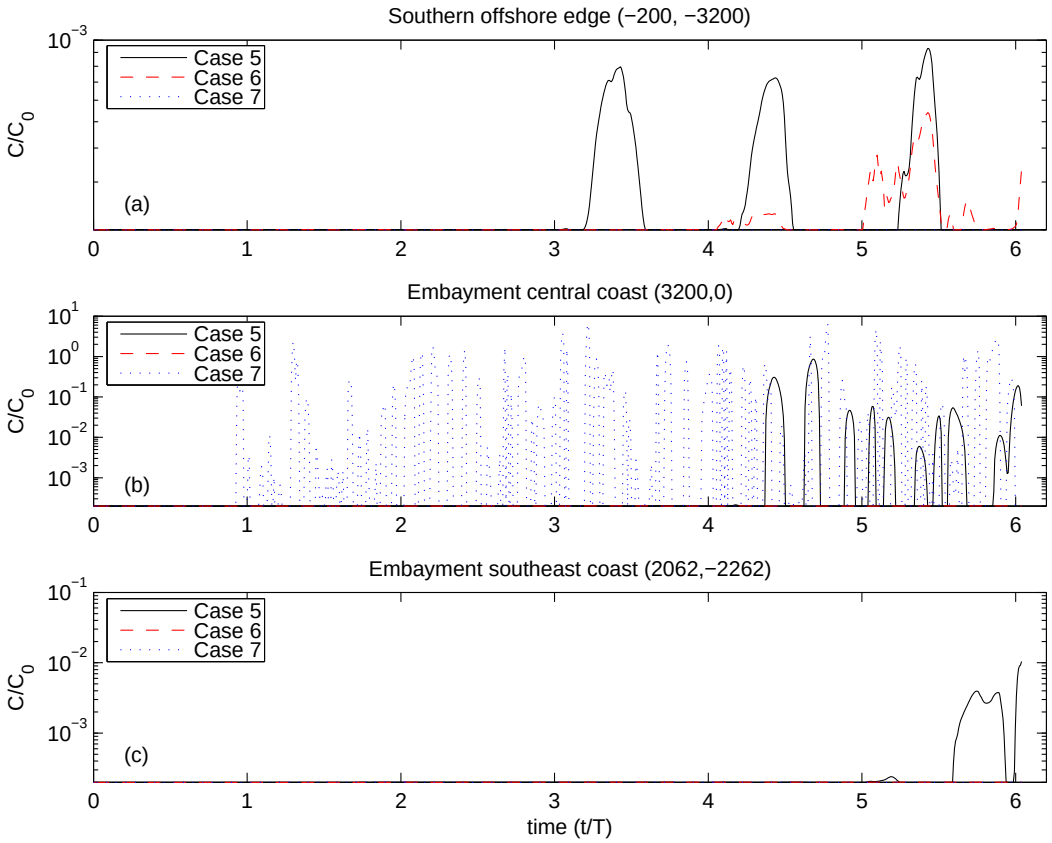

Figure 6.10: Time series of concentration profiles of passive scalar at three different locations along the embayment coast for nearshore cases 9, 10, and 11, respectively.

6.5 Summary

This study presents results from highly-resolved two-dimensional, depth-averaged numerical simulations of the mixing and transport of continuous point sources of waste from an array of aquaculture pens modeled as porous cylinders. The results highlight the complex and different dispersion patterns that occur under such flow conditions. In particular, the results from this study demonstrate the following key points:

- The mixing and dispersion of the pollutant field under oscillatory flow conditions with added drag from the fish pens is very different from the classical uni-directional flow case where a Gaussian plume spread occurs. Under oscillatory flow conditions, our results show plumes of waste with relatively high concentration occurring at considerable distances from the source.

- The large scale effect of the Earth's rotation does indeed influence the dispersion of contaminant plumes and should be accounted for in numerical models.

- The local runoff from rivers and other tributaries should be taken into account in modeling the plume dispersion in near-coastal environments.

- Accounting for the drag induced by the pens is important to accurately predict the level of mixing in numerical models for water quality applications.

- It is necessary to identify the correct (and dominant) hydrodynamic conditions at a particular fish farm site because these conditions will dramatically influence how far a waste plume from a fish farm site would spread.

In addition, our work shows strong "non-Gaussian" behavior in that the spatial decay is not necessarily exponential. This is highlighted by the statistics of the plume concentrations, which indicate highly peaked and skewed distributions and show that high concentrations of the scalar field can be found at significant distances from

the source. The results also indicate pronounced spatio-temporal variability in the concentration fields and this spatio-temporal variability is a strong function of the particular forcing parameters involved. *Based on our results, "dilution as a solution to pollution" should not be prescribed for marine aquaculture, particularly in near-shore systems.*

This study is a first step towards understanding the complex plume dispersion dynamics in the vicinity of aquaculture farms in nearshore coastal waters. Further work using three-dimensional simulations, is required to gain key insights into the three-dimensional flow structure that would occur in the close proximity of aquaculture pens. Furthermore, the flow model needs to be coupled with a biological model that will allow for the prediction of other water quality parameters, such as dissolved oxygen and plankton concentrations. The use of such models in the design of water quality regulations and the monitoring of wastes will be key to ensuring an environmentally sound aquaculture industry.

Chapter 7

Conclusion

7.1 Summary of investigation

There have been numerous studies over the last few decades on flow around obstacles and passive scalar mixing with an emphasis on understanding the turbulent vortex-wake dynamics under different flow conditions. Changes in hydrodynamic conditions and locations of obstacles can result in very complex scalar distributions. Improved understanding of the mixing under such conditions is required for developing better prediction and decision strategies in many environmental engineering problems related to water and air quality issues. The research discussed in this dissertation has been motivated by the need for improved understanding of scalar mixing and transport in widely varying environmental flow conditions such as in rivers, estuaries, oceans and the atmospheric boundary layer. As such, the main focus of this research is on fundamental aspects of passive scalar mixing around obstacles in environmental flows.

In this dissertation, an in-depth investigation of turbulent mixing of passive scalars under various flow conditions in the presence of the obstacles has been carried out using high-resolution, two-dimensional numerical simulations of the incompressible Navier-Stokes equations. The main results of the research are presented in Chapters

3, 4, 5, and 6, respectively.

In Chapter 3, the effects of the presence of a single porous cylinder under unidirectional mean flow condition and combined conditions of oscillatory and mean flows were presented using a total of 49 simulations. Fundamental aspects of the vortex-wake dynamics were discussed to highlight their effect on mixing by means of turbulent scalar diffusivity. This lateral scalar diffusivity was parameterized as a function of three key non-dimensional parameters.

In Chapter 4, scalar mixing and transport in flow reversal conditions were investigated. Two simulations in purely oscillatory flow conditions (i.e. no mean flow) with and without drag were performed to show the drag effect under such conditions, using a tidal forcing period of 8 hours. The simulation results reveal harmonic contractions and expansions of the scalar field resulting in much more convoluted flow patterns in the presence of an obstacle compared to the cases without flow reversals discussed in Chapter 3.

The work done in Chapter 5 primarily focused on understanding the vortex-wake interaction resulting from flow through multiple obstacles. Both a single column consisting of 3 cylinders and a staggered array consisting of 8 obstacles were used for this investigation. A total of eight simulations were performed as a part of this study. The results presented three different vortex scales depending on both the lateral and longitudinal spacing between the obstacles.

The impact of open netpet aquaculture farms located in an idealized coastal embayment was presented in Chapter 6. A total of seven depth-averaged simulations were performed that encompass a range of hydrodynamic and environmental conditions such as the rotation of the Earth, river inflow, strong tides, and the wind stress at the free surface as well as the location of pens. This engineering application highlights the importance of correct descriptions of hydrodynamic conditions, geometry, and location of obstacles at any given site in order to accurately predict the impact

of pollutants on the ecosystem and water quality.

7.2 Main conclusions

The following is a brief outline of the important results obtained from this study:

- From an in-depth parametric study, it was clearly shown in Figure 3.9, 3.15, and 3.19 how the three non-dimensional parameters C_D, η, and K affect the dispersion of a passive scalar plume. The lateral mixing coefficients were parameterized as a function of the non-dimensional drag coefficient C_D at two other given parameters (as shown in Equation (3.18) and Table 3.2, 3.3, and 3.4). Mixing was found to be greatly enhanced under the combined action of obstacle-induced drag and oscillatory flow superimposed into mean current with $\eta \leq 1$. The lateral mixing coefficient was considerably larger (about 40 times in some cases) than the typical classical dispersion coefficient of 0.15, depending on the amplitude and frequency of the oscillatory forcing as well as the porosity of the obstacle. As shown in Table 3.5, for oscillatory flows conditions with $\eta = 1$, the scaling factor $\lambda \approx 31 - 46$ in Equation (3.18) is about 6-9 times larger than that for uni-directional flow ($\lambda \approx 5$) in the presence of an obstacle.

- Under pure oscillatory flow conditions or even combined flows with $\eta > 1$, multiple flow reversals will cause older effluent discharge to return to the discharge site (as shown in time sequence of the passive scalar field of Figure 4.2 and 4.7), resulting in high concentration levels. In the absence of obstacles, a symmetric concentration distribution results in the lateral. However, the reversals cause the longitudinal profile to depart from the Gaussian distribution commonly observed for contaminant plumes in uni-directional flows. The effect of porosity of the obstacle for the pure oscillatory forcing field is significantly higher than for

the cases discussed in Chapter 3 (for $\eta < 1$) mainly due the stronger contraction and expansion of the plume during different phased of the tidal cycle.

- The interaction of the vortex-wake regions generated by multiple obstacles result in different large scale vortex-wake patterns. For steady uni-directional flow conditions, the results highlight the effect of the location of the obstacles, specifically the lateral and longitudinal spacing between adjacent obstacles. Different cylinder-, mid-, and array-size scale vortices can occur depending on the spacing between the obstacles. This study shows that locations of obstacles is a fundamental parameter that controls the intensity of the vortex interactions in a flow domain containing an array of obstacles.

- The field-scale study on the mixing of dissolved waste from aquaculture pens provided an understanding of the complex plume dispersion dynamics that can occur in the vicinity of fish farms in nearshore coastal waters. The complex concentration patterns depending on hydrodynamic conditions at a specific study site is highlighted by the statistics of the plume concentrations of the passive scalars, which indicate highly peaked and skewed distributions and show that the high scalar concentrations can be found at significant distances from the point source. The results also indicate pronounced spatio-temporal variability in the concentration field and this spatio-temporal variability is a strong function of the particular forcing parameters involved. Our results mainly show that "dilution as a solution to pollution" should not be prescribed for marine aquaculture, particularly in nearshore environments.

7.3 Suggestions for further research

This research is a first step towards gaining fundamental insights into the flow dynamics encountering the porous obstacles under the different flow conditions and can lead to better parameterizations of such processes for practical applications in engineering and oceanography. Further work using three-dimensional simulations is required to gain key insights into the three-dimensional flow structure that would occur in the close proximity of obstacles especially under stably stratified conditions. Ultimately, the hydrodynamics should be linked with the biology and as such, further extensions of this work should couple the flow model with a biological model that will for example allow for the prediction of other water quality parameters, such as dissolved oxygen and plankton concentrations. Such models are increasingly required for formulating appropriate water quality regulations and for monitoring purposes for a sustainable environment.

References . . . . . .

Anderson, J. D. 1995. *Computational fluid dynamics: The basics with applications.* McGraw-Hill, Inc.

Aris, R. 1956. On the dispersion of a solute in a fluid flowing throug a tube. *Proc. of Royal Soc. of Lon. Series A, Mathematical and Physical Sciences*, **235**, 67–77.

Balachandar, S., & Eaton, J. K. 2010. Turbulent dispersed multiphase flow. *Annu. Rev. Fluid Mech.*, **42**, 111–133.

Bella, D. A., & Dobbins, W. E. 1968. Difference modeling of stream pollution. *J. of Sanitary engineering division, Proc. of ASCE*, **94, No.SA5**, 995–1016.

Bosch, G., & Rodi, W. 1998. Simulation of vortex shedding past a square cylinder with different turbulence models. *Int. J. Numer. Meth. Fluids*, **28**, 601–616.

Bowden, K. F. 1967. Stability effects on turbulent mixing in tidal currents. *Phys.Fluids*, **10**, S278.

Carati, D., Winckelmans, G. S., & Jeanmart, H. 2001. On the modelling of the subgrid-scale and filtered-scale stress tensors in large-eddy simulation. *J. Fluid Mech.*, **441**, 119–138.

Casulli, V. 1999. A semi-implicit finite difference method for non-hydrostatic, free-surface flows. *Int. J. Numer. Meth. Fluids*, **30**, 425–440.

Catalano, P., Wang, M., Iaccarino, G., & Moin, P. 2003. Numerical simulation of the flow around a circular cylinder at high Reynolds numbers. *International Journal of Heat and Fluid Flow*, **24**, 463–469.

Chatwin, P. C. 1975. On the longitudinal dispersion of passive contaminant in oscillatory flows in tubes. *J. Fluid Mech.*, **71**, 513–527.

Chen, D., & Jirka, G. H. 1995. Experimental study of plane rurbulent wakes in a shallow water layer. *Fluid Dynamics Research*, **16**, 11–41.

Crimaldi, J. P., & Koseff, J. R. 2006. Structure of turbulent plumes from a momentumless source in a smooth bed. *Environ Fluid Mech.*, **6**, 573–592.

Crimaldi, J. P., Wiley, M. B., & Koseff, J. R. 2002. The relationship between mean and instantaneous structure in turbulent passive scalar plumes. *Journal of Turbulence*, PII: S1468–5248(02)32522–0.

Delaux, S., Stevens, C. L., & Popinet, S. 2010. High-resolution computational fluid dynamics modelling of suspended shellfish structures. *Environ Fluid Mech*, **11**, 405–425.

Dimotakis, P. E. 2000. The mixing transition in turbulent flows. *J. Fluid Mech.*, **409**, 69–98.

Ding, Y., & Kawahara, M. 1999. Three-dimensional linear stability analysis of incompressible viscous flows using the finite element method. *Int. J. Numer. Meth. Fluids*, **31**, 451–479.

Elder, J. W. 1959. The dispersion of marked fluid in turbulent shear flow. *J. Fluid Mech.*, **5**, 544–560.

Fernando, H. J. S., Zajic, D., Sabatino, S. Di, Dimitrova, R., Hedquist, B., & Dallman, A. 2010. Flow, turbulence, and pollutant dispersion in urban atmospheres. *Phys.Fluids*, **22**.

Fischer, H. B. 1978. On the tensor form of the bulk dispersion coefficient in a bounded skewed shear flow. *Journal of Geophysical Research*, **83**, 2373–2375.

Fischer, H. B., List, E. J., Koh, R. C. Y., Imberger, J., & Brooks, N. G. 1979. *Mixing in inland and coastal waters*. Academic Press.

Fringer, O. B. 2007. *SUNTANS user guide, Stanford Unstructured Nonhydrostatic Terrain-following Adaptive Navier-Stokes Simulator*.

Fringer, O. B., Gerritsen, M., & Street, R. L. 2006. An unstructured-grid, finite-volume, nonhydrostatic, parallel coastal ocean simulator. *Ocean Modelling*, **14**, 139–173.

Germano, M., Piomelli, U., Moin, P., & Cabot, W. H. 1991. A dynamic subgrid-scale eddy viscosity model. *Phys.Fluids*, **3**, 1760–1765.

Gerrard, J. H. 1978. The wakes of cylindrical bluff bodies at low Reynolds number. *Phil. Trans. R. Soc. of Lon. Series A, Mathematical and Physical Sciences*, **288**, 351–382.

Giles, R. T. 1995. Optimal strategies for discharging pollutants into narrow estuaries. *Wat. Res.*, **29**, 563–569.

Guillaume, D. W., & LaRue, J. C. 1999. Investigation of the flopping regime with two-, three- and four-cylinder arrays. *Exp. Fluids*, **27**, 145–156.

Gullbrand, J., & Chow, F. K. 2003. The effect of numerical errors and turbulence models in large-eddy simulations of channel flow, with and without explicit filtering. *J. fluid Mech.*, **495**, 323–341.

Harleman, D. R. F., Lee, C. H., & Hall, L. C. 1968. Numerical studies of unsteady dispersion in estuaries. *J. of Sanitary engineering division, Proc. of ASCE*, **94**, SA 5, 897–991.

Helsley, C. E., & Kim, J. W. 2005. Mixing downstream of a submerged fish cage: a numerical study. *IEEE J. Ocean Eng.*, **30**, 12–19.

Holley, E. R., Harleman, D. R. F., & Fischer, H. B. 1970. Dispersion in homogeneous estuary flow. *J. of Hydraulics division, Proc. of ASCE*, HY 8, 1691–1709.

Hoyas, S. J., & Jimenez, J. 2006. Scaling of the velocity fluctuations in turbulent channel up to $Re_\tau = 2003$. *Phys.Fluids*, **18**, 011702.

Jachec, S. M., Fringer, O. B., Gerritsen, M. G., & Street, R. L. 2006. Numerical simulation of internal tides and the resulting energetics within Monterey Bay and the surrounding area. *Geophys Res Lett*, **33**, L12605.

Jackson, C. P. 1987. A finite-element study of the onset of vortex shedding in flow past variously shaped bodies. *J. Fluid Mech.*, **182**, 23–45.

Kay, A. 1990. Advection-diffusion in reversing and oscillating flows: 1. The effect of a single reversal. *IMA Journal of Applied Mathematics*, **45**, 115–137.

Kay, A. 1997. Advection-diffusion in reversing and oscillating flows: 2. Flows with multiple reversals. *IMA Journal of Applied Mathematics*, **58**, 185–210.

Keulegan, G. H., & Carpenter, L. H. 1958. Forces on cylinders and plates in an oscillating fluid. *Journal of Research of the National Vureau of Standards*, **60**, 423–440.

Kumar, B., & Mittal, S. 2006. Effect of blockage on critical parameters for flow past a circular cylinder. *Int, J. Numer. Meth. Fluids*, **50**, 987–1001.

Kundu, P. K., & Cohen, I. M. 2008. *Fluid mechanics*. Academic Press.

Lau, Y. L., & Krishnappan, B. G. 1977. Transverse dispersion in rectangular channels. *J. of Hydraulics division, Proc. of ASCE*, **103**, HY10, 1173–1189.

Liu, Y. I., & Tsai, S. T. 1993. Contaminant contraction in two-dimensional oscillatory flows. *Applied Mathematics and Mechanics*, **14**, 1003–1012.

Meneveau, C., & Katz, J. 2000. Scale-invariance and turbulence models for large-eddy simulation. *Annu. Rev. Fluid Mech.*, **32**, 1–33.

Moulinec, C., Hunt, J. C. R., & Nieuwstadt, F. T. M. 2004. Disappearing wakes and dispersion in numerically simulated flows through tube bundles. *Flow, Turbulence and Combustion*, **73**, 95–116.

Munson, B. R., Young, D. F., Okiishi, T. H., & Huebsch, W. W. 2009. *Fundamentals of fluid mechanics*. 6th edn. John Wiley and Sons, Inc.

Naylor, R., & Burke, M. 2005. Aquaculture and ocean resources: raising tigers of the sea. *Annu. Rev. Environ. Resour.*, **30**, 185–218.

Nepf, H. M. 1999. Drag, turbulence, and diffusion in flow through emergent vegetation. *Water Resources Research*, **35**, 479–489.

Nicolle, A., & Eames, I. 2011. Numerical study of flow through and around a circular array of cylinders. *J. Fluid Mech.*, **679**, doi:10.1017/jfm.2011.77.

Papoulis, A., & Pillai, S. U. 2002. *Probability, random varialbes and stochastic processes*. McGraw-Hill, Inc.

Plew, D. R., Spigel, R. H., Stevens, C. L., Nokes, R. I., & Davidson, M. J. 2006. Stratified flow interactions with a suspended canopy. *Environ Fluid Mech*, **6**, 519–539.

Pope, S. B. 2000. *Turbulent flows.* Cambridge University Press.

Pope, S. B. 2004. Ten questions concerning the large-eddy simulation of turbulent flows. *New Journal of Physics*, **6**, 35.

Purnama, A., & Kay, A. 1999. Effluent discharge into tidal waters: optimal or economic strategy? *Environmetrics*, **10**, 601–624.

Reynolds, W. C. 1990. The potential and limitations of direct and large eddy simulations. *Lecture Notes in Physics*, **357**, 313–343.

Richardson, L. F., & Stommel, H. 1948. Note on eddy diffusion in the sea. *J. Meteorol.*, **5**, 238–240.

Rossi, R., & Iaccarino, G. 2008. Numerical simulation of scalar dispersion downstream of a square obstacle. *Annual Research Briefs*, 287–312.

Rossi, R., Philips, D. A., & Iaccarino, G. 2009. Numerical simulation of scalar dispersion in seperated flows using algebraic flux models. *In: Turbulence, Heat and Mass Transfer 6. 6th International Symposium on Turbulence, Heat and Mass Trnasfer*, Rome, Italy.

Rummel, A. C., Socolofsky, S. A., v. Carmer, C. F., & Jirka, G. H. 2005. Enhanced diffusion from a continuous point source in shallow free-surface flow with grid turbulence. *Phys.Fluids*, **17**, 075105.

Smagorinsky, J. 1963. General circulation experiments with the primitive equations. *Mon. Weath. Rev.*, **91**, 99–164.

Smith, R. 1981. A delay-diffusion description for contaminant dispersion. *J. Fluid Mech.*, **105**, 469–486.

Smith, R. 1982. Contaminant Dispersion in Oscillatory Flows. *J. Fluid Mech.*, **114**, 379–398.

Smith, R. 1983. The concentration of contaminant distributions in reversing flows. *J. Fluid Mech.*, **129**, 137–151.

Smith, R. 1985. When and where to put a discharge in an oscillatory flow. *J. Fluid Mech.*, **153**, 479–499.

Smith, R. 2000. Optimal discharging in a branched estuary. *J. Engr. Math.*, **38**, 309–322.

Smith, R., & Purnama, A. 1999. Two ourfalls in an estuary: optimal wasteload allocation. *J. Engr. Math.*, **35**, 273–283.

Smith, R., & Scott, C. F. 1997. Mixing in the tidal environment. *J. Hydr. Engr.*, **123**, 332–340.

Stacey, M. T., Cowen, E. A., Powell, T. M., Dobbins, E., Monismith, S. G., & Koseff, J. R. 2000. Plume dispersion in a stratified, near-coastal flow: measurements and modeling. *Cont Shelf Res*, **20**, 637–663.

Stevens, C., Plew, D., Hartstein, N., & Fredriksson, D. 2008. The physics of open-water shellfish aquaculture. *Aquacultural Engineering*, **38**, 145–160.

Sumner, D., Wong, S. S. T., Price, S. J., & Paidoussis, M. P. 1999. Fluid behaviour of side-by-side circular cylinders in steady cross-flow. *J. Fluid and Struct*, **13**, 309–338.

Tanino, Y., & Nepf, H. M. 2008. Lateral dispersion in random cylinder arrays at high Reynolds number. *J. Fluid Mech.*, **600**, 339–371.

Taylor, G. I. Sir. 1922. Diffusion by continuous movements. *Proc. London Math. Soc.*, **s2-20**, 196–212.

Taylor, G. I. Sir. 1953. Dispersion of soluble matter in solvent flowing slowly through a tube. *Proc. of Royal Soc. of Lon. Series A, Mathematical and Physical Sciences*, **219**, 186–203.

Taylor, G. I. Sir. 1954. The dispersion of matter in turbulent flow through a pipe. *Proc. of Royal Soc. of Lon. Series A, Mathematical and Physical Sciences*, **223**, 446–468.

Tennekes, H., & Lumley, J. L. 1972. *A first course in turbulence*. The MIT Press.

Ting, T. S., & Prakash, M. 2005. Simulation of high Reynolds number flow over a backward facing step using SPH. *Mathematical and Information Science, Technical Report*.

Venayagamoorthy, S. K. 2006. *Energetics and dynamics of internal waves on a shelf break using numerical simulations*. Ph.D. thesis, Stanford University.

Venayagamoorthy, S. K., Ku, H., Fringer, O. B., Koseff, J. R., Chiu, A., & Naylor, R. L. 2011. Numerical Modeling of aquaculture dissolved waste transport in a coastal embayment. *Env. Fluid Mech.*, **11**, 329–352.

Wang, B., Fringer, O. B., giddings, S. N., & Fong, D. A. 2008. High-resolution simulations of a macrotidal estuary using SUNTANS. *Ocean Modelling*, **26**, 60–85.

Warhaft, Z. 2000. Passive scalars in turbulent flows. *Annu. Rev. Fluid Mech.*, **32**, 203–240.

Webb, T., & Tomlinson, R. B. 1992. Design procedures for effluent discharge to estuaries during ebb tide. *J. Envirn. Engng, Proc. of ASCE*, **118**, 338–362.

White, B. L., & Nepf, H. M. 2003. Scalar transport in random cylinder arrays at moderate reynolds number. *J. Fluid Mech.*, **487**, 43–79.

Williamson, C. H. K. 1985. Sinusoidal flow relative to circular cylinders. *J. Fluid Mech.*, **155**, 141–174.

Williamson, C. H. K. 1996. Vortex dynamics in the cylinder wake. *Annu. Rev. Fluid Mech*, **28**, 477–539.

Wu, X., Homsy, G., & Moin, P. *Flow over a backward-facing Step (spanwise vorticity).* Center for Turbulent Research.

Yasuda, H. 2004. Analytical study of longitudinal mass flux due to the shear effect in a tidal basin. *Journal of Oceanography*, **60**, 587–596.

Zhang, H. J., & Zhou, Y. 2001. Effect of unequal cylinder spacing on vortex streets behind three side-by-side cylinders. *Phys.Fluids*, **13**, 3675–3686.

Zhang, X., & Perot, B. 2000. Turbulent vortex shedding from triangle cylinder using the turbulent body force potential model. *In: Proceedings of ASME FEDSM'00. ASME 2000 Fluids Engineering Division Summer Meeting*, Boston, MA.

Zhang, Z., Fringer, O. B., & Ramp, S. R. 2011. Three-dimensional, nonhydrostatic numerical simulation of nonlinear internal wave generation and propagation in the South China Sea. *Journal of Geophysical Research*, **116**, C05022.